

Neutral strange particle production in $p + p$ collisions at $\sqrt{s} = 200$ GeV and pentaquark searches with STAR at RHIC

Inauguraldissertation
der Philosophisch-naturwissenschaftlichen Fakultät
der Universität Bern

vorgelegt von
Mark T. Heinz
von Zürich (ZH) und Sils i.Domleschg (GR)

Leiterin der Arbeit:
Prof. Dr. S.Kabana
Laboratorium for Hochenergiephysik, Universität Bern

Von der Philosophisch-naturwissenschaftlichen Fakultät angenommen.

Bern, 23. Juni 2005

Der Dekan:

Prof. Dr. P. Messerli

To Ariane and Mathilda
For their love and encouragement

Abstract

The Relativistic Heavy Ion Collider on Long Island is capable of colliding hadrons and heavy ions at a center of mass energy of 200 GeV/nucleon. The experiments at RHIC were specifically designed to search for signatures of the Quark Gluon Plasma (QGP), a state of deconfined quark and gluon matter predicted by lattice QCD calculations to exist at energy densities above ≈ 0.6 GeV/fm³. Furthermore, high p_T particle jets produced in the collision may interact with the QGP and probe the medium.

The enhancement of strange particles has been predicted as one of the signatures of QGP formation. In this thesis we present an analysis of the neutral strange particles K_s^0 , Λ and $\bar{\Lambda}$ in $p + p$ collision at $\sqrt{s} = 200$ GeV performed at the STAR experiment. This measurement establishes an important baseline to which heavy ion experiments can be compared to. We find that yields for K_s^0 and Λ in $p + p$ collisions are significantly lower than the preliminary results in Au+Au collisions at the same energy.

Furthermore, this high statistics measurement of strange particle transverse momentum spectra allows us to constrain phenomenological leading order and next-to-leading order models. Our results are consistent with mini-jet production which has been proposed as dominant production mechanism of high- p_T particles in $p + p$ collisions.

By comparing to phenomenological models (PYTHIA, NLO) we test the implementation of non-perturbative processes in these models, i.e. string fragmentation, and show that for strange baryons in particular the current fragmentation functions do not produce good agreements with our data.

In addition we show preliminary results from the θ^+ pentaquark searches in $p + p$ and $d + Au$ collisions at STAR.

Acknowledgements

I would like to start by thanking my host at Brookhaven National Laboratory, Dr. Tim Hallman, for inviting me to this government facility and allowing me the necessary infrastructure to perform my research. I also am grateful to Prof. John Harris of Yale University for allowing me to be an ‘unofficial’ member of his group and a part of the STAR collaboration.

I would like to thank my thesis advisor Prof. Sonia Kabana for her support and guidance. A special thanks to Prof. Helen Caines who was a great mentor and always spared time to discuss physics.

I thank my colleagues and friends at STAR who where interested in my research and involved me in fruitful discussions: Betty, Boris, Camelia, Christina, Christoph, Gene, Jerome, John, Jon, Lee, Manuel, Matt, Mike, Rene, Richard, Sevil, Thomas and Thorsten.

Last but not least, I thank my parents for their continuous unconditional support and for encouraging me to set my goals high in life.

Contents

1	Introduction	1
2	Theoretical concepts	3
2.1	Elementary particles	3
2.2	Quantum Chromodynamics	4
2.2.1	Asymptotic freedom	6
2.2.2	Perturbative QCD and Factorization	7
2.3	Dynamics of $p + p$ collisions	8
2.3.1	Mini-jet evidence	8
2.3.2	Cross-Section definitions	10
2.4	Quark Gluon Plasma (QGP)	11
2.5	Strangeness Production	12
2.6	Models for hadronic collisions	14
2.6.1	Thermal statistical models	14
2.6.2	Leading-order (LO) pQCD Models	15
2.6.3	Next-to-Leading-order (NLO) formalism	17
2.6.4	Multiple scattering formalism (NeXus/EPOS)	19
3	Experiment	21
3.1	RHIC collider overview	21

3.1.1	RHIC accelerator and cooling	24
3.1.2	Accelerating heavy ions	24
3.1.3	Accelerating protons	25
3.2	The STAR detector system	25
3.2.1	Time Projection Chamber (TPC) Design	28
3.2.2	Time Projection Chamber performance	31
3.2.3	Trigger Detectors	34
3.2.4	Silicon Vertex Tracker (SVT)	38
4	Analysis	41
4.1	Event reconstruction	41
4.1.1	Cluster and Track reconstruction	41
4.1.2	Primary Vertex Finding and Event Selection	42
4.1.3	'Pile-up'	50
4.2	V^0 particle reconstruction	52
4.2.1	particle identification	52
4.2.2	Topological cuts in V^0 analysis	53
4.2.3	Cuts to reduce backgrounds from pile-up	58
4.2.4	Yield extraction from invariant mass	60
4.2.5	Invariant mass peaks vs p_T	64
4.3	Corrections	66
4.3.1	Applying vertex corrections to spectra	66
4.3.2	Efficiency and acceptance corrections	66
4.3.3	Feed-down contributions to Λ	69
4.4	V^0 -analysis using SVT information	73
5	Results	77
5.1	Results from V^0 -Analysis	77

5.1.1	Transverse Momentum Spectra	77
5.1.2	Anti-particle to particle ratio	83
5.1.3	Systematic errors	84
5.2	Multiplicity study	87
5.2.1	$\langle p_T \rangle$ and $dN/d\mathbf{y}$ vs. event multiplicity	90
5.2.2	R_{pp} vs. Event Multiplicity	94
6	Exotic Searches	97
6.1	Experimental pentaquark evidence	98
6.2	Theory	98
6.2.1	Chiral Soliton Model	98
6.2.2	The Jaffe-Wilzcek Diquark model	99
6.3	Analysis	100
6.3.1	Pre-filtering of events	101
6.3.2	Reconstructing θ^+	103
6.3.3	θ^+ background method	106
6.3.4	θ^+ Monte-Carlo simulation	107
6.3.5	Cross-checks	113
6.4	Results and Discussion	113
6.4.1	Cross-Section estimation	116
6.4.2	Conclusion	117
7	Discussion	119
7.1	Comparison to previous measurements	119
7.1.1	p_T -Spectra and yields	119
7.1.2	Particle ratios	122
7.2	$\langle p_T \rangle$ Systematics	123
7.2.1	$\langle p_T \rangle$ vs N_{ch}	123

7.2.2	$\langle p_T \rangle$ vs. particle mass	127
7.3	Comparison to model predictions	129
7.3.1	PYTHIA 6.221	129
7.3.2	PYTHIA Summary	136
7.3.3	Next-to-leading order calculations (NLO)	137
7.3.4	EPOS v1.02 (formerly NEXUS)	140
7.4	Strangeness Enhancement at STAR	143
7.5	Nuclear modification factor	145
7.6	Conclusions	148
7.7	Outlook	149
A	Table of values	151
A.1	Table of p_T -Spectra	151
A.2	Table of $\langle p_T \rangle$ vs N_{ch}	155

Chapter 1

Introduction

The ultimate goal of high energy physics (HEP) is to explore the realm of the very small and discover the building blocks of nature and our universe. One of the phenomena which are important in high energy physics is the so-called QCD phase transition which is predicted to occur at sufficiently high energy density. To recreate this transition from a hadronic phase to a phase of deconfined quarks and gluons, the **Quark Gluon Plasma**, we collide very energetic heavy nuclei in order to obtain the required energy density.

At the same time, by doing so we will create a medium that is comparable to what astrophysicists believe existed in the early stages of the universe. Thus, maybe providing answers to a yet other philosophical question such as 'How did the universe begin ?' and 'How is matter created from energy?'.

In this quest high energy physicists have been devising collider and accelerator experiments to create collisions that should release a sufficient amount of energy. By doing so they have been pushing the technological envelope in many related sciences, i.e. mathematics and computer technology, over the last 50 years.

One of the first particle physics experiments was at the Cyclotron at

Lawrence Berkeley National Laboratory (LBNL) in California capable of accelerating protons to 1.2 MeV (million electron-volts) was completed in 1932 [1]. Today, we are capable of accelerating whole atoms (more precisely ions) to reach up to 200 GeV per nucleon at the Brookhaven National Laboratory (BNL) in New York and in a few years the Large Hadron Collider (LHC) at CERN is expected to accelerate protons and nuclei to several TeV per nucleon, one million times the energy reached by the LBNL cyclotron.

In this thesis the emphasis will be on a specific type of particle produced in these collisions: **strange particles**, i.e. containing one or more strange quarks. If a Quark Gluon Plasma is created at RHIC, the production of strange quarks is believed to be enhanced with respect to a hadron gas.

In a wider context, some astrophysicists believe that there may be stable strange matter at the core of neutron stars [3, 2].

In particular we will focus on strange particles produced in the intermediate to high transverse momentum range which is believed to be dominated by string fragmentation process. This mechanism is described in current phenomenological models by fragmentation functions obtained from elementary collision data. The present measurement in $p+p$ collisions may help constrain the model calculations and thereby advance our knowledge of hadronization mechanism.

Chapter 2

Theoretical concepts

2.1 Elementary particles

Today's knowledge of elementary particles is summarized in a model called the Standard Model (SM), which combines the elementary particles with the four 'elementary' forces known to physicists: Gravitation, Electromagnetic force, Weak nuclear force and Strong nuclear force.

It is a beautiful model with many symmetries grouping the elementary particles into bosons or force carriers (spin 0 or 1) and fermions (spin 1/2). The fermions are either leptons (electrical charge -1 or zero) or quarks (fractional electrical charge). The neutrino leptons have close to zero mass, no charge and interact very weakly with matter. The quarks come in 6 different flavours, paired into 3 families or generations as shown in figure 2.1. Murray Gell-Mann coined the name quark in 1964 and classified the particles in the scheme he called 'Eightfold Way', for which he received a Nobel in 1969.

The gluon is the force mediator between quarks of the so-called strong nuclear force, it is in a sense the 'glue' between the quarks. The photon is the force mediator of the electromagnetic force, a force that attracts electric

Elementary Particles

Quarks	u up	c charm	t top	Force Carriers
	d down	s strange	b bottom	
Leptons	ν_e electron neutrino	ν_μ muon neutrino	ν_τ tau neutrino	Z Z boson
	e electron	μ muon	τ tau	W W boson
	I	II	III	
	Three Families of Matter			

Figure 2.1: Table of elementary particles and forces known in the standard model.

charges and is well known to most of us. The weak nuclear force is mediated by two bosons, a neutral one (Z) and two charged ones (W^\pm). It is responsible, among other things, for nuclear chain reactions. Finally, gravitation is the weakest force and a force mediator boson is expected to exist but has still to be found experimentally.

2.2 Quantum Chromodynamics

As well as being flavored each quark also carries a color charge; red, blue or green. Quarks and gluons are confined in color-neutral objects called baryons and mesons, which are jointly known as hadrons. A baryon consists of 3 quarks of different color, a meson consists of a quark and an anti-quark. All experimental attempts to separate a single free quark from a hadron have failed.

The strong nuclear force acting between quarks is described in a theory

called Quantum Chromodynamics (QCD), in reference to the greek word *chromos* reminding us that it deals with colored objects. This interaction is also referred to as the strong interaction since it's coupling is many times stronger (≈ 100) than the electromagnetic and thousands times more than the weak nuclear force.

For this theory Feynman, Schwinger and Tomonaga received a Nobel prize in 1965. Quantum Chromo Dynamics is in many ways similar to the theory of electromagnetic interactions or Quantum Electrodynamics (QED) were the effective coupling between electrons is given by:

$$\alpha_{QED}(Q^2) = \frac{\alpha_0}{1 - (\alpha_0/3\pi)\log(Q^2/m_e^2)} \quad (2.1)$$

Here m_e is the electron mass and Q is the momentum transfer between the two electrons. At large distances the value of the effective coupling is smaller due to the effect of charge screening and reaches it's asymptotical value of $\alpha_0 = \frac{1}{137}$.

Similarly in QCD a gluon couples between quarks but, in contrast to QED, can also couple to other gluons, since they also carry color charge. As an example, let two partons with 4-vector momentum p_1 and p_2 couple via a gluon, then the momentum transfer is defined by:

$$q^2 = -Q^2 = (p_2 + p_1)^2 \quad (2.2)$$

And the QCD coupling is given by:

$$\alpha_s(Q^2) = \frac{4\pi}{(11 - \frac{2}{3}n_f)\log(Q^2/\Lambda_{QCD}^2)} \quad (2.3)$$

Here n_f is the number of quark flavours and Λ_{QCD} is an important perturbative scale variable which has to be determined experimentally. When

$Q = \Lambda_{QCD}$ the effective coupling becomes infinite, which is nowadays assumed to be around 200 MeV. On the other hand at very large values of Q^2 , or small distances, the coupling tends to zero and quarks appear to move freely [4]. This important property of the strong force is called **asymptotic freedom**.

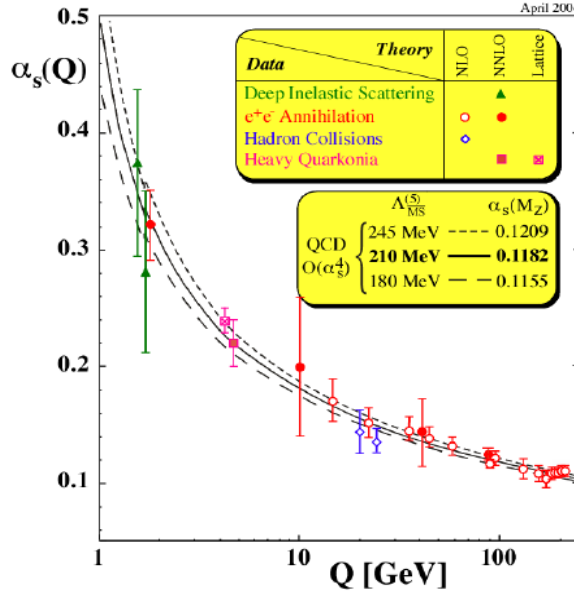


Figure 2.2: Running coupling constant, α_s , versus momentum transfer, Q . The world average measurement of α_s is given at the value of the Z boson mass (91.2 GeV). Taken from [4]

2.2.1 Asymptotic freedom

The physical reason for the vanishing of α_s at small distances or large Q^2 can be understood by the color screening effects of the vacuum. Color charges can radiate gluons and thus are no longer located at a definite place in space. As the Q^2 of the incoming probe increases, thereby looking at smaller and

smaller distances, it becomes less likely to find the charge, resulting in a weaker and weaker effective coupling.

The theoretical discovery of Asymptotic Freedom in 1973 by Gross, Politzer and Wilczek was awarded last year (2004) with the Nobel price [5].

Thus, the theory of strong interactions predicts confinement into color-neutral hadrons at large distances and small Q^2 . At short distances and large Q^2 however deep inelastic scattering (DIS) experiments, where an electron interacts with a quark inside a hadron, have been successful in investigating the strong interactions. These experiments probe the momentum distributions of quarks and gluons inside the hadrons and provide us with experimental knowledge of the parton distribution functions (PDF).

2.2.2 Perturbative QCD and Factorization

Perturbation theory is a mathematical concept by which a system of equations that cannot be solved analytically is separated into two parts. The first part has an analytic solution and the second contains the non-analytic part without solution. By modifying the stable part by a small perturbation one can study how the solutions evolve as the exact system undergoes this perturbation.

In order to apply perturbative theory to QCD (pQCD) we need sufficiently small values of α_s . This means that pQCD can only describe processes at small distance scales and large momentum transfer Q^2 .

In $p + p$ collisions, interactions between partons from the two nuclei typically involve large transfer of momentum and thus constitute an example of a pQCD process. These high Q^2 parton interactions, also referred to as hard-scatterings, produce hadron jets with large transverse momentum.

Furthermore, in order to make predictions of the produced final state

hadrons we apply the factorization theorem. It states that as long as α_s is small the inclusive hadron cross-section can be written as a convolution of three independent parts: parton distribution functions (PDF), parton cross-section and fragmentation functions (FF). Both the PDF's and the FF are non-perturbative objects and thus have to be determined experimentally.

$$\frac{d^2\sigma^h}{dydp_T} = K \sum_{abcd} \int dx_a dx_b f_a(x_a, Q^2) f_b(x_b, Q^2) \frac{d\sigma}{d\hat{t}}(ab \rightarrow cd) \frac{D_{c/d}^h(z, M_f)}{\pi z_{c/d}} \quad (2.4)$$

Equation 2.4 shows how the hadron cross-section can be described in terms of these three elements. The PDF's of the two hadrons f_a, f_b depend on $x_a = p_{parton}/p_{hadron}$ the fraction of momentum of parton a with respect to the hadron momentum and Q^2 . The fragmentation function $D_{c/d}^h$ describes the creation of a hadron h from a parton c depends on $z_c = p_{parton}/p_{hadron}$ of the outgoing parton and the factorization scale M_f . $\frac{d\sigma}{d\hat{t}}$ is the differential cross-section of the parton hard scattering. The sum runs over all parton species a,b,c,d involved in the hard scattering and the integral over all fractional momenta x_a, x_b of the two incoming partons.

2.3 Dynamics of $p + p$ collisions

2.3.1 Mini-jet evidence

The production of hadrons from p+p collisions is the main topic of this thesis and is an important area to test QCD. Experimentally we can measure the high p_T hadrons, also referred to as jets, that are due to the parton hard-scattering process. These jets are often azimuthally correlated since they conserve the directional information of the parton scattering. The first

observation of jets in hadronic collisions was in the early 1980's by the UA2 experiment at SPS collider in CERN [6].

Figure 2.3 shows the transverse energy deposition in the electromagnetic calorimeter tiles as a function of azimuthal and polar angle. The peaks of the 2 opposite jet-centers are clearly visible.

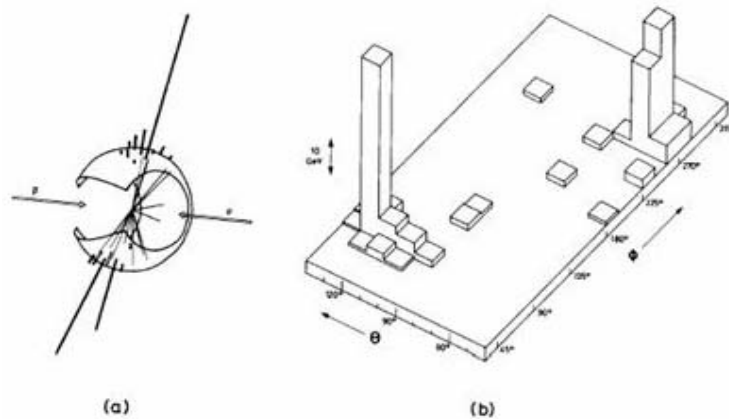


Figure 2.3: First observation of jets in $\bar{p} + p$ collisions by UA2 experiment at CERN. Taken from [6]

More evidence for jets in high energy $p + p$ collisions comes from the mean number of produced charged particles ($\langle N_{ch} \rangle$). This number is proportional to the cross-section and at lower energies, i.e. less than 100 GeV, it has a logarithmical dependency on the collision energy (\sqrt{s}) as shown by Thome et al [7] in the seventies. More recent $\bar{p} + p$ and $p + p$ experiments at SPS energies of 200-1800 GeV measured cross-section which are clearly above the expected values by Thome's 'law' and thus signal new phenomena creating additional particles [8].

Finally, the shape of the multiplicity distribution has also been studied in detail. At lower energies these distributions were seen to scale perfectly

onto a 'universal shape' according to Koba-Nielson-Oleson (KNO)[9]. The distributions from the higher energy experiments did not scale and displayed a different shape with additional high multiplicity events. This violation of KNO-scaling at higher energies has also been attributed by several authors [41, 70] to the creation of jets in hadronic collisions. The term mini-jet is often used for low p_T jets that produce several lower p_T hadrons.

2.3.2 Cross-Section definitions

The hadronic cross-section can be divided into elastic and in-elastic collisions. In in-elastic collisions the particles transform part of their kinetic energy to create new particles. In-elastic collisions can be sub-divided into diffractive and non-diffractive processes.

1. elastic collisions
2. in-elastic collisions
 - (a) singly diffractive
 - (b) doubly diffractive
 - (c) non-diffractive

Diffractive processes are defined as processes where one nucleon acts as a region of absorption and the interference of scattering amplitudes gives rise to diffraction pattern in the forward and backward regions. A nucleon suffering a diffractive scattering will become excited and lose a small amount of energy when breaking up into a few particles at a small emission angle. This can occur in one of the nucleons (singly) or in both (doubly). In non-diffractive processes the nucleons hit 'head-on' and both disintegrate

creating large particle multiplicities at mid-rapidity. The STAR $p+p$ Trigger is only sensitive to the **non-singly diffractive (NSD)** cross-section since it requires charged tracks to be detected in coincidence on both sides of the interaction point. This represents about 70% of the inelastic cross-section.

2.4 Quark Gluon Plasma (QGP)

In this section I will briefly introduce the phenomenology of the heavy ion collisions, since this was one of the main reasons for building RHIC.

It is believed that in high energy heavy ion collisions the energy density is sufficient to create a new state of matter, called a quark-gluon plasma or QGP. In this state quarks and gluons are de-confined and move freely over large distances. The experiments studying heavy ion collisions have gathered a large amount of evidence for the existence of the QGP although the final proof remains open [10].

In figure 2.4 shows the space-time evolution of how events are believed to unfold in a heavy ion collision. In this 1+1 dimensional representation time flows from bottom to top and the spatial expansion is on the x-axis. About 1 fm/c (the timespan it takes light to traverse the size of a proton) after the beams collide, a QGP is formed. Bjorken estimated the energy density of the system at that time to be $\approx 1 \text{ GeV}/\text{fm}^3$ and established that this is closely related to the total rapidity density of the produced particles [11]. At $T_c \approx 170 \text{ MeV}$, the critical temperature, the phase transition to a hadron gas is believed to occur. At T_{ch} , the chemical freeze-out temperature, in-elastic collisions cease and the bario-chemical composition is fixed. Finally, at T_{fo} or thermal/kinetic freeze-out temperature, the elastic interactions cease and the momentum distributions of the particles are fixed. We have tried to

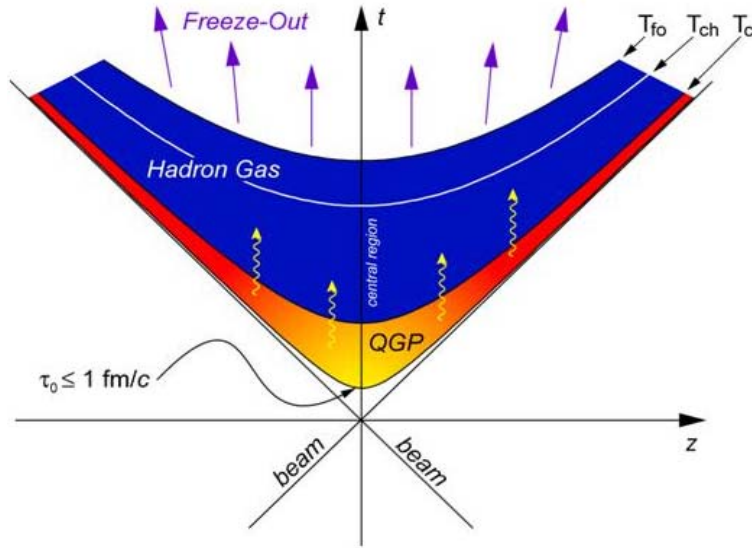


Figure 2.4: Space-time evolution of a heavy ion collision assuming the formation of Quark-Gluon Plasma.

determine appropriate observables to measure each one of these stages of a heavy ion collision.

2.5 Strangeness Production

Strange particles are the main actors of this thesis and I will briefly introduce the reasons for investigating these particles and the processes by which strange quarks are produced. Rafelski and Muller postulated in 1982 that strange particle production is enhanced in the Quark Gluon Plasma with respect to that in a hadron gas [12, 13]. Strangeness production in a hadron gas has to proceed via the strangeness conserving strong hadronic interactions. These reactions typically have high energy thresholds of several hundreds of

MeV.

In the presence of a deconfined QGP however, $s\bar{s}$ pairs can be copiously formed via associated production mechanisms, $g + g \rightarrow s\bar{s}$ and $q\bar{q} \rightarrow s\bar{s}$. The energy for these processes is of order of the 2 times strange quark mass, i.e. ≈ 300 MeV and thus much lower than for hadronic reactions. Overall the thermal gluon fusion process calculated to be much more important for $s\bar{s}$ production, i.e. accounts for 85-90% total rate, and also is responsible for the chemical equilibration of strangeness in the QGP.

Experimentally two different observables have been proposed to measure this effect. The ratio of strange quarks pairs with respect to the non-strange quark pairs was proposed by Wroblewski [16]. This ratio is strongly dominated by the most abundant strange particle, the kaon, and it's ratio to the pion. The energy dependance of this ratio λ_s , e.g. estimated here [17, 22], has a maximum at $\sqrt{s} \approx 6$ GeV as shown in figure 2.5.

$$\lambda_s = \frac{2\langle s\bar{s} \rangle}{\langle u\bar{u} \rangle \langle d\bar{d} \rangle} \quad (2.5)$$

One way to quantify strangeness enhancement is by λ_s going from ≈ 0.25 in elementary collisions [15], to ≈ 0.45 in central heavy ion collisions. This effect becomes more important as the strangeness content of the particle increases. This was noticed by Rafelski and others who predicted that the strangeness enhancement should be even stronger for multi-strange anti-baryons [18].

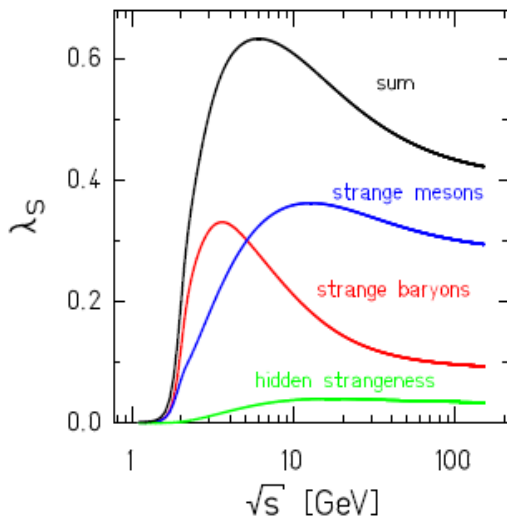


Figure 2.5: Contributions to the Wroblewski factor λ_s in heavy ion collisions from strange baryons (red), strange mesons (blue) and mesons with hidden strangeness (green). Taken from [22]

2.6 Models for hadronic collisions

2.6.1 Thermal statistical models

The thermo-dynamic approach to hadron production in particle collisions has been quite successful at describing macroscopic observables at lower energies [54]. For example, the transverse mass ($m_T = \sqrt{m_0^2 + p_T^2}$) spectra of the produced particles has been seen to be exponential in shape.

These **statistical models** of hadron production were extensively adapted and used in different collisions systems, i.e. elementary $e^+ + e^-$ and $p + p$ as well as nuclear collisions [20, 21, 22]. The models assume that all hadrons originate from a hadron gas fireball in full **thermal equilibrium**, and that they decouple from the fireball at a given freeze-out temperature T_{ch} . After

decoupling there are no more in-elastic interactions between the particles and the hadron abundances are fixed. Some models allow for partial **chemical equilibrium** of the system by introducing an additional parameter γ_s .

In order to calculate particle abundances statistical mechanics is inferred using conservation of quantum numbers. In a relatively small system, i.e. $e^+ + e^-$ and $p + p$, several authors apply the canonical form which requires that the Quantum numbers are conserved exactly. In a larger system, as present in heavy ion collisions, the grand canonical form is used, where quantum numbers are conserved on average. The conservation laws are implemented via the statistical partition function:

$$Z_k = V \frac{g_k}{2\pi^2} m_k^2 T K_2\left(\frac{m_k}{T}\right) \exp(B_k \mu_B + Q_k \mu_Q) \quad (2.6)$$

The one particle partition function is given by equation 2.6, for a particle of mass m_k . Here V is the volume, T the temperature, g_k the spin-isospin degeneracy factor, B_k the baryon number, Q_k the electric charge, μ_b and μ_Q are the corresponding chemical potentials.

The predictions of the statistical model can be compared with data and the quality of the fit gives information on the degree of agreement of this particular assumption.

For example, the values obtained from $\bar{p} + p$ collision at $\sqrt{s} = 200$ GeV are $T \approx 175$ MeV, the volume $V \approx 35 fm^3$ and strangeness suppression $\gamma_s \approx 0.54$ [19]. Using these values the calculated particle abundances compared to the experimental data is shown in figure 2.6.

2.6.2 Leading-order (LO) pQCD Models

The other 'school of thought' are so-called micro-scopic models which reduce elementary particle collisions, $p + p$ and $e^+ + e^-$, into the level of the fun-

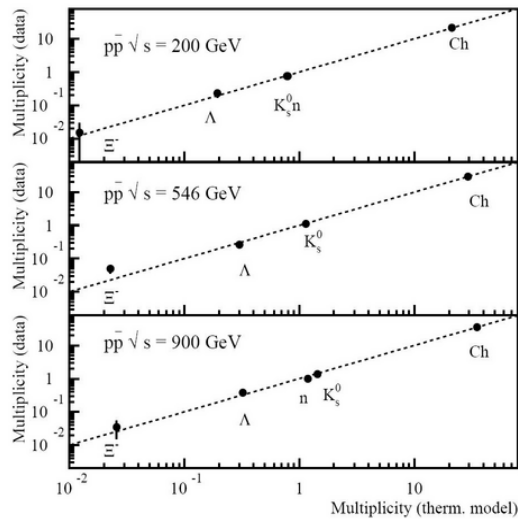


Figure 2.6: Yields calculated with the thermal statistical model for $\bar{p} + p$ collisions at $\sqrt{s} = 200$ GeV(top), 546 GeV(center), 900 GeV(bottom). Taken from [19]

damental interactions between quarks and gluons ("partons") governed by QCD. It is not possible to get an exact solution from first principles, however when large momentum transfers Q^2 are involved a perturbative approximation is valid.

In the early 1980's Ellis *et al.* calculated jet-structures in $e^+ + e^-$ collisions using pQCD [23]. This have since been refined and implemented in computer codes. One of the most common elementary collisions 'event generators' using Monte-Carlo simulations is **PYTHIA** [25]. It is based on the JETSET algorithm developed in the late seventies by the Lund group and successfully applied to $e^+ + e^-$ data from PETRA and PEP [26]. The parton cross-section is approximated by $2 \rightarrow 2$ processes and the associated LO Feynman diagrams. Parton distribution functions, as well as the fragmentation functions, are non-perturbative objects and cannot be calculated from QCD first

principles. They are therefore user-defined from a list of currently available parametrizations. The default hadronization mechanism in PYTHIA is the “**Lund symmetric string fragmentation**” parametrization [28].

Figure 2.7 is a visualization of the string fragmentation process. It takes the simple picture of a quark(blue)-antiquark(green) pair along 1 dimension in space (z) and time dimension. As the q and \bar{q} move apart we picture a color flux tube being stretched between them like a string (red lines). The potential energy grows and is stored in the string, quantified by a string constant κ . At some point this energy becomes sufficiently large that the string can break creating a new quark-antiquark pair, which then hadronize to form a meson. Baryon production can be similarly described by the production of diquarks [27].

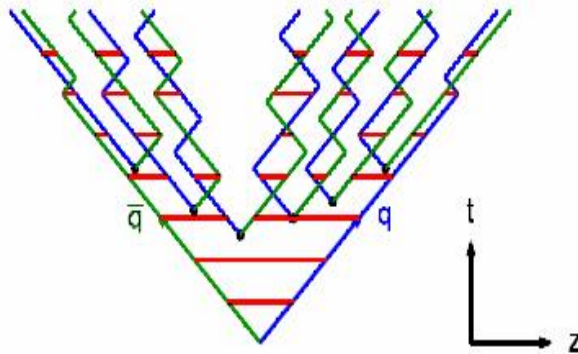


Figure 2.7: Schematic of string fragmentation process

2.6.3 Next-to-Leading-order (NLO) formalism

In order to remediate the inaccuracies of the simple LO-approach we need to include parton processes at higher orders in α_s . This is the goal of the NLO formalism. It calculates additional parton cross-sections for higher order

Feynman diagrams and uses NLO parameterizations of the parton distributions and fragmentation functions (FF). The additional parton processes include radiative corrections from initial and final state gluon radiation. Figure 2.8 is an example of a fragmentation function parametrization derived from $e^+ + e^-$ data at $\sqrt{s} = 5.2-91.2$ GeV. The variable on the x-axis is the energy fraction of the outgoing hadron with respect to the total energy of the system $x = 2E_{hadron}/\sqrt{s}$. The difference between LO and NLO is most clearly seen, in the fact that the gluon function becomes 'softer', i.e. more lower energy hadrons are produced, in NLO.

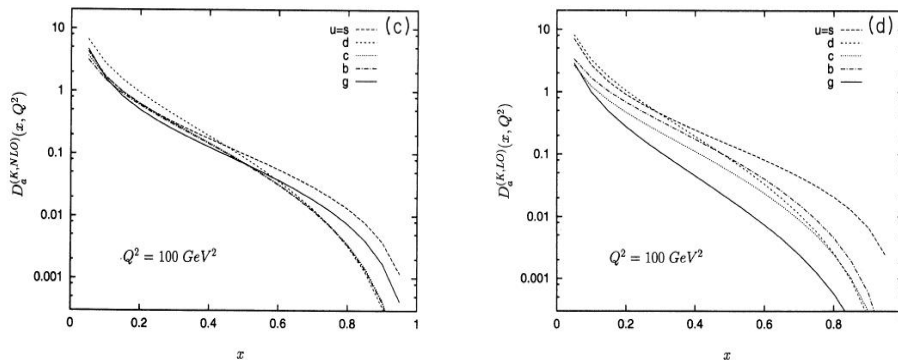


Figure 2.8: Fragmentation function parametrization by Kramer-Kniehl-Poetter (KKP) for charged kaons at LO (left) and NLO (right). Contributions from different quark flavor and gluons are shown separately. Taken from [29]

The authors of fragmentation functions shown in figure 2.8 have also shown in a recent publication that the universality of fragmentation function postulated by the QCD factorization theorem can be verified using experimental data [31]. Another important property of QCD that can be tested experimentally with fragmentation functions is the scale evolution. It states that once the x-dependance of the fragmentation function at some scale Q^2

is known it can be computed at any other scale by use of the Altarelli-Parisi equations [30].

2.6.4 Multiple scattering formalism (NeXus/EPOS)

The EPOS model evolved over time but started as in the late 1980's as the VENUS model by Klaus Werner [32, 33]. It is based on Gribov-Regge theory (GRT) [34], an effective field theory, that allows multiple interactions between partons to happen 'in parallel'. This is as opposed to Pythia where the parton interaction are mainly $2 \rightarrow 2$ processes. The elementary interactions are described by pomerons, whose precise nature is not known but can be described in terms of string ladders pairs, and between which interference terms can be calculated.

Other models based on the GRT approach include the Dual Parton Model (DPM) [35] and the Quark Gluon String model (QGS) [36]. These three models have the same formalism for the elastic cross-section.

The VENUS model was then further extended and renamed into NeXus model [37]. The main difference of the Nexus model is that it is a parton-based GRT and therefore uses this type of framework to define the in-elastic cross section using hard scattering language. Parton-parton scattering processes are described in a consistent way as 'soft', 'hard' or 'semi-hard'. This approach is then extrapolated to nucleus-nucleus collisions and has been successful in describing particle multiplicities and rapidity distributions at different collision energies [37].

Hadronization is achieved by string fragmentation, however not according to the Lund framework, but rather using the Artru-Mennessier string breaking, which defines the breaking points by an area law [38]. This allows for strings to break into sub-strings and also the formation of off-shell

resonances.

Chapter 3

Experiment

3.1 RHIC collider overview

The analysis presented in this thesis was carried out at the STAR experiment at the Relativistic Heavy Ion Collider (RHIC) on Long Island, New York. The collider was designed to study heavy ion and polarized p+p collisions and is located at the Brookhaven National Laboratory, a dedicated facility for research in natural sciences and medicine.

There are four experiments that are installed at RHIC in a configuration shown in figure 3.1, each one built with a focus on a specific high energy physics topic:

1. STAR: Stands for "**Solenoidal Tracker at RHIC**" and includes a large Time projection chamber (TPC) which has the unique capability of reconstructing complex particle decay topologies from strange particles, resonances and charmed mesons. It also includes EM calorimeters for high- E_T jet reconstruction.
2. PHENIX: Short for "**Pioneering High Energy Nuclear Interact-**

ing Experiment” has an excellent system for identifying high transverse momentum pion, kaon and protons. Moreover it has two muon tracker arms which are instrumental in reconstructing the decay of J/Ψ particles.

3. PHOBOS: Is named for a **moon of Mars** and is focused on precisely measuring the identified particle multiplicity at mid-rapidity by use of silicon spectrometers. It is capable of measuring particles at low p_T where the bulk of them is produced.
4. BRAHMS: The **Broad Range Hadron Magnetic Spectrometer** is designed to measure identified hadrons over a wide range of rapidity and transverse momentum.

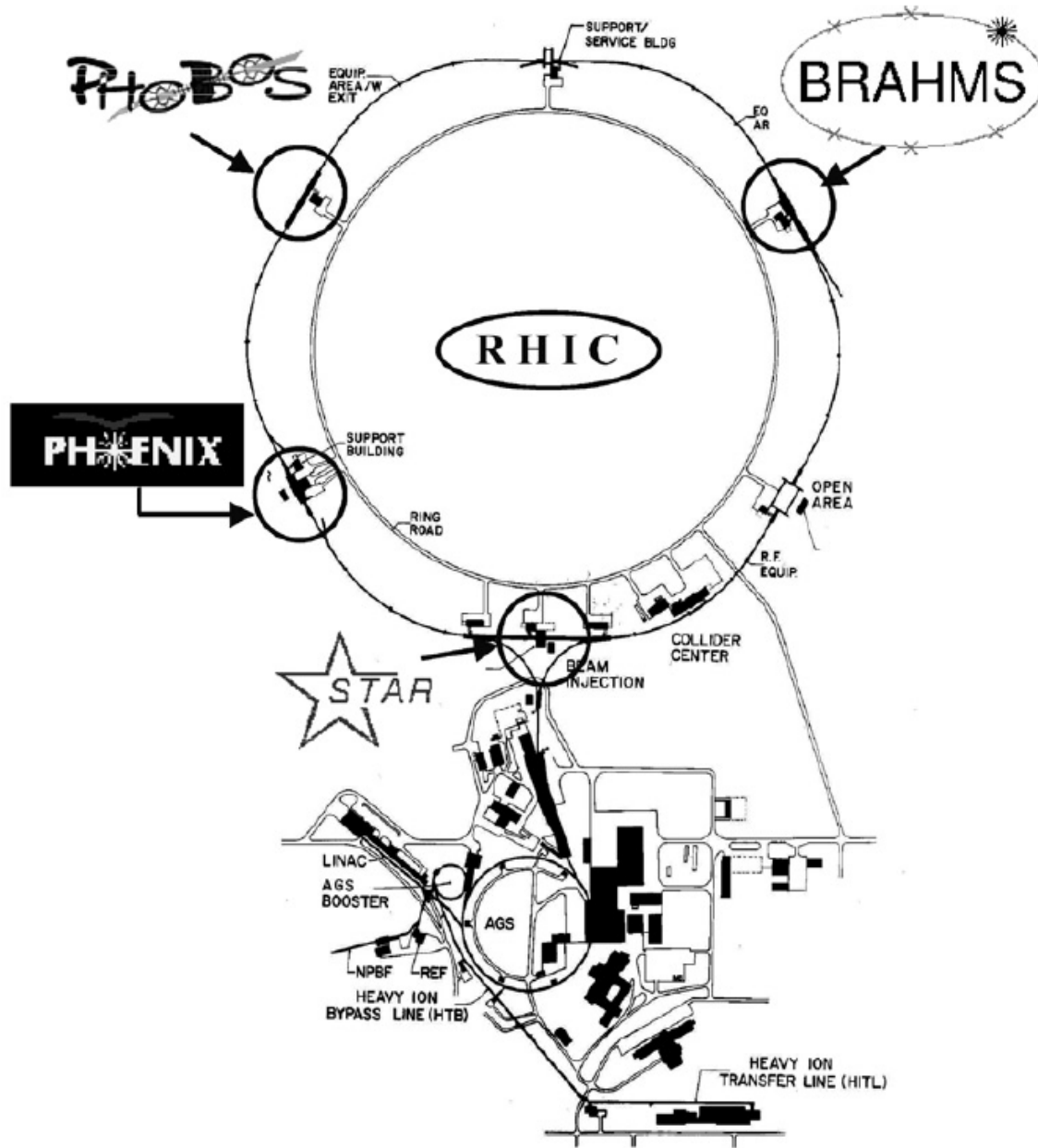


Figure 3.1: RHIC collider overview

3.1.1 RHIC accelerator and cooling

The RHIC accelerator consists of two concentric storage rings for counter-rotating beams. The rings intersect in six different locations around a total circumference of 3.8km. Each ring consists of 6 arc sections and 6 straight insertion sections.

Altogether 1740 super-conducting dipole magnets along the circumference are used for bending of the ion beams. These magnets need to be cooled down to 4.6 K during operation by the use of liquid nitrogen and liquid hydrogen. The recycling and refrigeration of these cooling agents consume a gigantical quantity of 21 mega-watts of electricity. This is the main reason for operating the accelerator only during the 6 winter months per year.

3.1.2 Accelerating heavy ions

The acceleration scenario up to full energy uses a chain of three accelerators in the injector chain. During this sequence the ions are successively stripped of their electrons. A pulsed sputter-source provides negatively charged gold ions to the Tandem Van de Graaff. There they are partially stripped of their electrons by passing through a carbon foil. At the end of this first acceleration stage the ions have acquired 1Mev/u and are now stripped of 32 electrons (Au^{+32}). They are then delivered to the Booster Synchrotron and further accelerated to 95 Mev/u. Next the beam is injected into the AGS (Alternating Gradient Synchrotron) in 24 bunches and with a charge of $Q=+77$. The AGS has now to bring these bunches up to the RHIC injection energy of 10.8 GeV/u. They are re-bunched into 4 bunches during this cycle and await ejection into the RHIC tunnel one bunch at a time. Before passing to the RHIC beam-line they are stripped of the remaining two electrons.

3.1.3 Accelerating protons

For the running with proton beams the injection procedure is different. Protons are injected directly from the existing 200MeV Linear Accelerator (LINAC). From there the beams pass through the booster system and are injected into the AGS for further acceleration before being injected into the RHIC rings. In the RHIC rings the protons are stored in so-called 'bunches' with 100×10^9 ions per bunch. The main reason for storing the ions in discrete bunches is to allow for optimized acceleration in the RF cavities. Furthermore, by tracking the location of the bunches, the experiments can be informed of their location and triggering is facilitated. The number of bunches can be varied by the operators according to the needs of the experiments. Up to 60 bunches can be stored, however the fewer the easier it is to keep a stable running condition.

3.2 The STAR detector system

The STAR detector system was designed for the investigation of strongly interacting matter at very high energy densities in order to search for signatures of the quark gluon plasma. Its unique feature is a large Time Projection Chamber (TPC) with full azimuthal and large pseudo-rapidity coverage around mid-rapidity gives it the capability of detecting a large range of charged hadrons. Furthermore it is especially well suited for the reconstruction of jet-events and multiple particle final state decays, i.e. strange and charmed baryons and resonances. Figure 3.2 and 3.3 show schematics of the STAR experiment. A solenoidal magnet with a uniform magnetic field of 0.5 T surrounds the whole detector system and provides for charged particle momentum analysis. Inside the magnet are the different detectors, starting

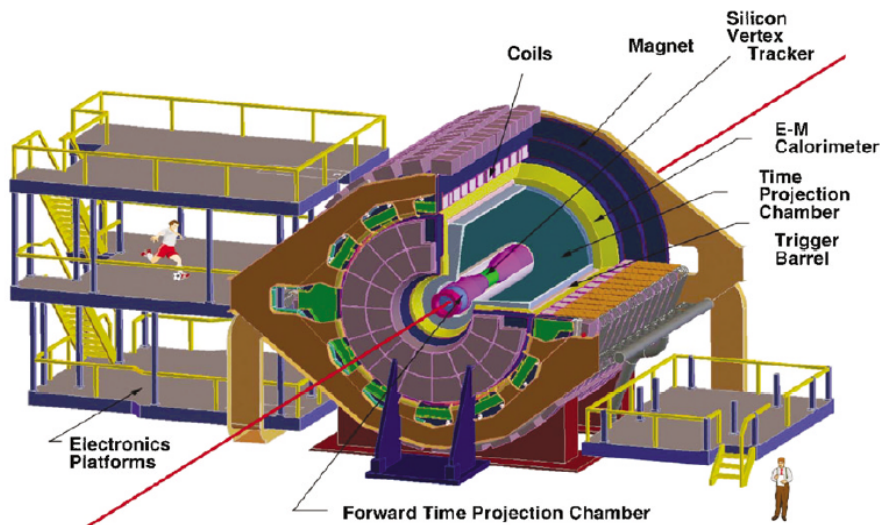


Figure 3.2: STAR Experiment. Cut-away taken from [44]

with the farthest from the beamline (ass seen in figure 3.3:

- Barrel Electromagnetic Calorimeter (EMC): measures total energy deposition of charged and neutral particles.
- Ring Imaging Cerenkov Counter (RICH): measures high momentum tracks.
- Central Trigger Barrel (CTB): Fast scintillator detector to measure charged particle multiplicity.
- Time of Flight (TOF): measures identified charged particles in the intermediate momentum range.
- Time Projection Chamber (TPC): measures charged tracks and specific energy loss (dE/dx) allowing identification of π, k, p and electrons.

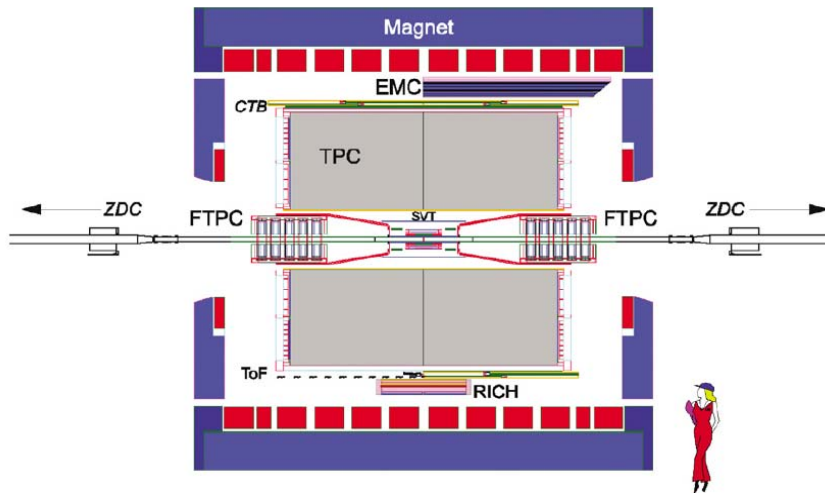


Figure 3.3: Schematic of STAR Detector systems. Taken from [44]

- Silicon Vertex Tracker (SVT): high precision tracking measurement of tracks close to the interaction vertex.
- Forward Time Projection Chamber (FTPC): measurement of charged tracks at high rapidity.
- Zero Degree Calorimeters (ZDC): Trigger detector sensitive to very forward spectator neutrons for Au+Au triggering.
- Beam Beam Counters (BBC) (not shown): Trigger detector sensitive to forward charged tracks used in $p + p$ triggering.

In addition to the original detectors installed at the start of the program several upgrades are now in place and operational:

- Endcap Calorimeter (EEMC)

- Silicon Strip Detector (SSD)
- Photon Multiplicity Detector (PMD)
- Forward Pion Detector (FPD)

A complete description of the STAR experiment can be found here [43, 44].

3.2.1 Time Projection Chamber (TPC) Design

The TPC is the primary tracking device of the STAR experiment. In central Au-Au collisions more than 1000 primary particles are produced per unit of pseudo-rapidity. This is a very challenging environment for reconstructing tracks. The TPC is capable of measuring charged tracks within $-1.8 < \eta < 1.8$ and with transverse momenta greater than 100 Mev.

The TPC consists of two concentric cylinders as shown in figure 3.5 located inside the STAR solenoidal magnet that operates normally at 0.5 T, but can also be operated at half-field or at zero-field optionally. The TPC is 4.2m long with inner and outer radii of 50cm and 200cm respectively. It is a gas filled cylindrical volume in which secondary electrons from ionizing particles are captured. Under the force of a uniform electrical field between the central membrane (High Voltage membrane) at 28kV and the anode planes at opposite ends of the TPC these electrons drift longitudinally, i.e. along the beam axis, towards the readout caps at the two ends of the cylinder. The uniformity of the electrical and magnetic fields is important since the precision of the hit reconstruction space-coordinates depends on it. The TPC gas is a mix of 10% methane and 90% argon (technically known as P10) and regulated at 2 mbar above atmospheric pressure. This mixture creates fast drift velocity at low electric fields. The total drift time is approximately 40

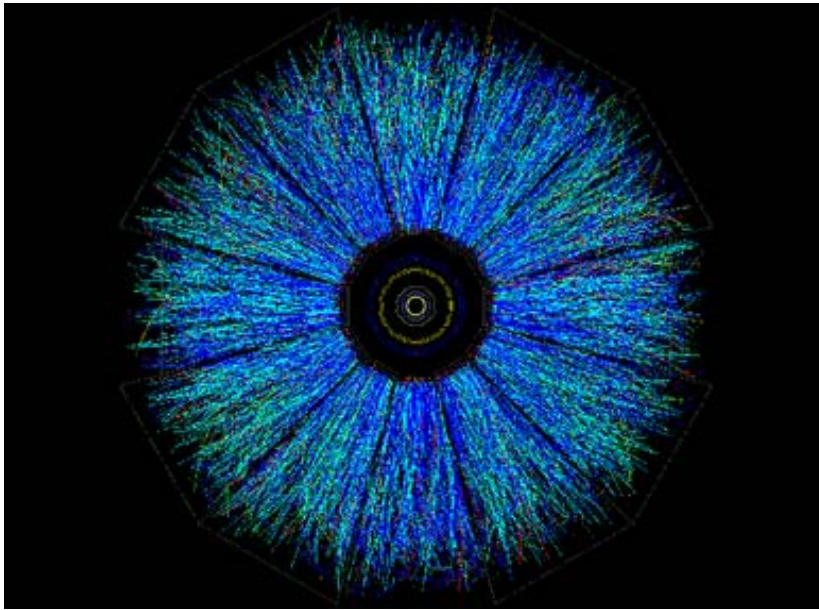


Figure 3.4: Reconstructed tracks with the STAR Time Projection Chamber in a Au+Au collision at $\sqrt{s} = 130$ GeV. Taken from [44]

μs and depends on the actual drift velocity. Since the drift velocity must be known with a precision of 0.1% it is measured periodically during the run via lasers. These lasers are disposed around the outer radius of the TPC and create artificial tracks when operated in between runs.

The anode pad plane where the electrons are read-out is divided into 12 sectors each with an inner and an outer subsector. Each sector is equipped with 5692 read-out pads and a multi-wire proportional-counter chamber (MWPC) for the amplification of the electron signal. The MWPC is composed of 3 wire planes as shown in figure 3.6, each with a specific function. The gating grid can be opened or closed by varying the potential and prevents electrons from un-triggered events reaching the anode wires. When an event is triggered the grid is opened, i.e. all the wires are set at the same potential, and

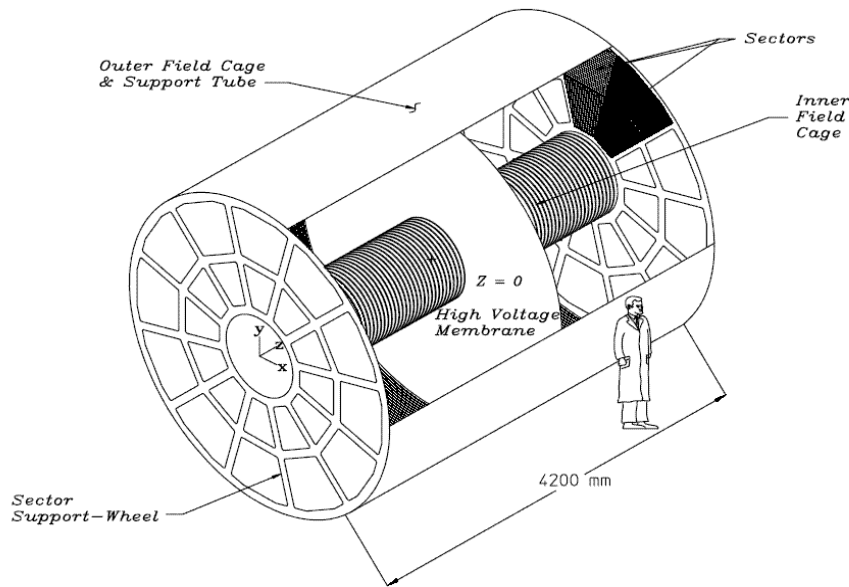


Figure 3.5: STAR Time Projection Chamber (TPC). Taken from [45]

the electrons can freely drift past it. The ground and anode wire together with the pad planes form the MWPC. When the electrons drift towards the anode wires held at a positive potential of 1170 volts (inner sectors) resp. 1390 volts (outer sectors) they accelerate and initiate an avalanche leaving a cloud of positively charged ions around the anode wires. The shape and size of the ion cloud depends on the number of parameters, i.e. primary ions, drift distance, diffusion and gas gain.

The configuration of the read-out pads within the inner and outer sub-sector is shown in figure 3.7. The 12 sectors at each end of the TPC have a dead spacing of 3 mm. In the inner sub-sector, where the track density is highest the 1750 pads each have a dimension of 2.85mm X 11.5mm. In the outer sub-sector the pads are larger with a dimension of 4mm X 20mm but spaced differently as seen in figure 3.7.

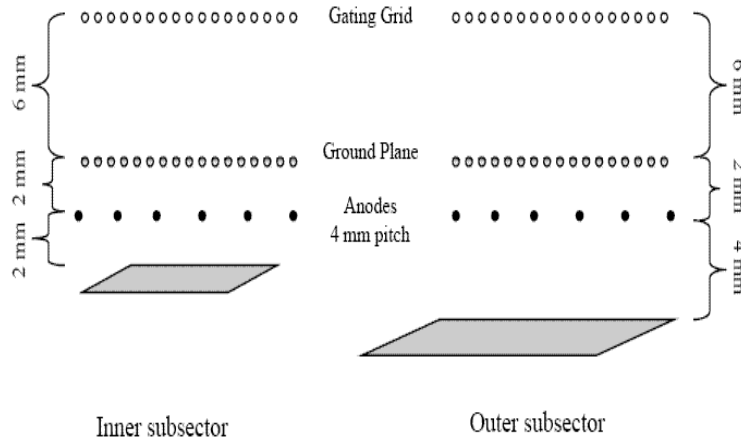


Figure 3.6: The TPC MWPC including the configuration of the wire planes and the pad readout plane. Taken from [46].

When charge is collected in a pad, the three dimensional space-coordinates are reconstructed from the information of the pad-location in r and ϕ and the drift-time (z). The mean drift velocity is measured to be $\approx 5.45\text{cm}/\mu\text{s}$ and the electronics are read-out in 512 time-bins (100ns apart). Thus the distance in z from the center of the TPC can be calculated by using this information. Since the charge of one hit is usually distributed over several bins in r , ϕ and time a cluster algorithm needs to be applied to determine the center and size of the hit.

3.2.2 Time Projection Chamber performance

The TPC performance is characterized mainly by the hit-resolution which ultimately translates into physical quantities such as tracking efficiency, momentum resolution and dE/dx resolution. The dE/dx measurement of charged tracks, i.e. the measurement of specific energy loss by charged tracks due to

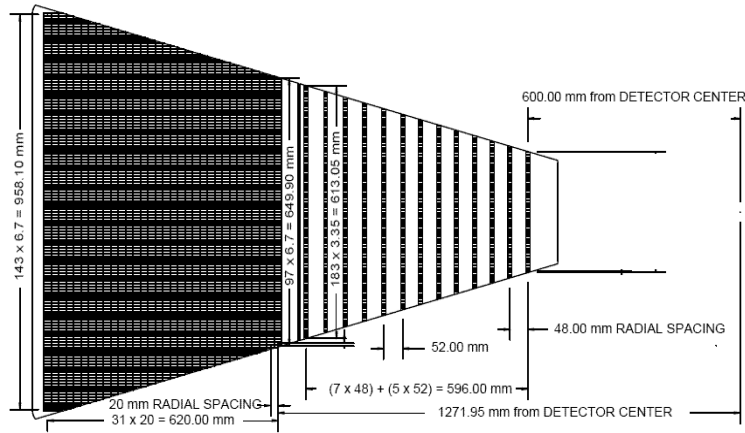


Figure 3.7: TPC anode pad plane for 1 sector. The geometrical arrangement of the 5692 pads within the inner and outer sector are shown. Taken from [45].

ionization, is very important and this information is used in nearly every STAR analysis to identify pions, kaons, protons and even electrons. The theoretical curves of specific energy loss in matter are given by the Bethe-Bloch formula:

$$\frac{dE}{dx} \approx Kz^2 \frac{Z}{A} \frac{1}{\beta^2} \left(\frac{1}{2} \ln \frac{2m_e c^2 \beta^2 \gamma^2 T_{max}}{I^2} - \beta^2 \right) \quad (3.1)$$

gives the amount of energy a particle with charge z will lose via ionization when traversing a gas of charge number Z and mass number A . m_e is the electron mass, $K \approx 0.31 \text{ MeV cm}^2$, β and γ are the relativistic variables, T_{max} is the maximum kinetic energy imparted to a free electron in a single collision and I is the average ionization energy of the material. The dE/dx resolution is defined as the number of gaussian σ between two particle bands as shown in figure 3.8. It depends on the track length and has been measured to be

8% for a track crossing 40 pad-rows. Practically this means that pions and protons can be separated up to a momentum of 1 GeV/c.

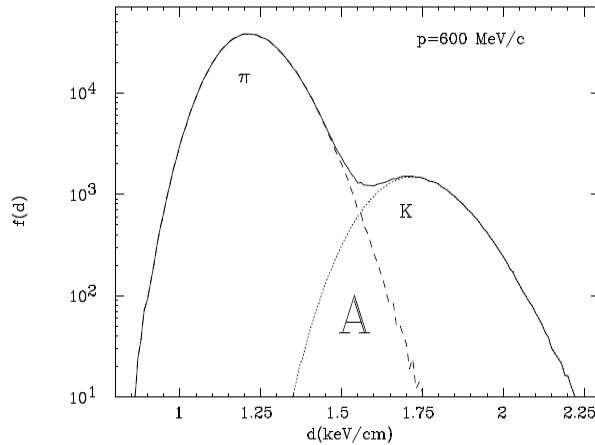


Figure 3.8: TPC dedx resolution. Taken from [47]

The hit-resolution for vertical tracks normal to a padrow is between 0.4-0.7mm in the transverse direction and between 0.7-1.2mm in the drift direction. The main distortions that can affect these resolutions are due to non-uniformities in the fields which lead to a non-uniform drift of the electrons. In STAR the electric and magnetic fields are parallel and distortions along the pad row are typically small. However millimeter scale distortions in the transverse directions are important because they affect the transverse momentum (p_T) determination especially for high- p_T particles. To correct for this, the magnetic field was carefully mapped and the electric field calculated using the detector geometry. The field distortions are entered into the drift equations which determine the resulting corrections in x and y that are applied to the hit positions [50].

Finally the tracking efficiency for pions has been experimentally estimated

in Au+Au collisions using Monte-Carlo (MC) simulations and is shown in figure 3.9. For peripheral collisions, with track multiplicities similar to p+p, it can be seen that the efficiency reaches 90% at > 0.3 GeV/c in p_T .

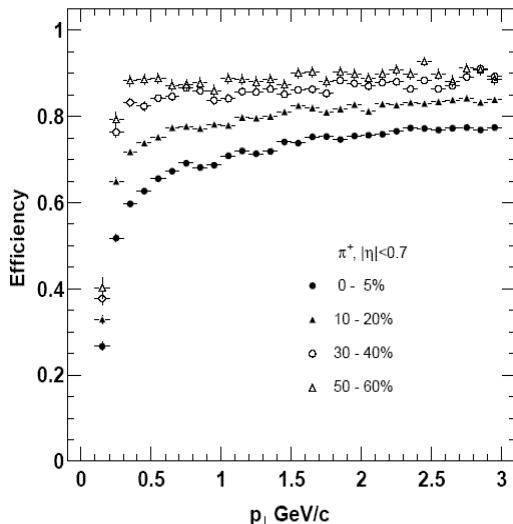


Figure 3.9: Tracking efficiency for pions in Au+Au collisions in STAR vs. collision centrality at half-field magnetic setting (0.25T). Taken from [51].

Another important quantity is the p_T resolution. This has also been measured using MC simulations and is dependant on track p_T . It increases roughly linearly from 2% for $p_T = 0.5$ GeV/c to 7% at $p_T = 9.25$ GeV/c [52].

3.2.3 Trigger Detectors

Since the interaction rate of the collisions at RHIC is ≈ 10 MHz and the slow detectors (TPC, SVT and others) that yield the physics are not capable of working at these frequencies Trigger detectors are used in order to 'pre-filter' events that may contain the desired physics. These trigger detectors can record at the interaction frequency and will select, based on the requested

trigger conditions, which events to 'trigger-on' and gather information from the other slower detectors. The slow detectors can only record data at ≈ 100 Hz and so the fast detectors have to reduce the rate of triggering by almost 5 orders of magnitude. The storage rate for events that pass the trigger criteria is again significantly less ≈ 5 Hz.

The STAR detector consists of five primary trigger detectors: a Central Trigger Barrel (CTB), two Zero Degree Calorimeter (ZDC), a Multi-wire Counter (MWC), two Beam-Beam Counters (BBC) and a Barrel Electromagnetic Calorimeter (BEMC). In this section we will only discuss the CTB and the BBC in detail since they were used during the p+p run of 2001/2002.

The **Beam-Beam Counters (BBC)** are the main trigger detectors used in p+p running. They were installed shortly before the p+p run to provide an efficient trigger for events with low multiplicity in the mid-rapidity region. The BBC's are installed along the beam axis ≈ 374 cm away from the interaction region. They cover the pseudo-rapidity region from $3.4 < |\eta| < 5.0$ which is equivalent to an outer radius of 9.64cm around the beam pipe.

They consist of 18 scintillator tubes as shown in figure 3.10 which are connected via optical light-guides to 8 photo-multiplier tubes (PMT). In order to trigger on an event coincident signals, above a certain threshold, are required between the BBC's at positive and negative η . The BBC coincidence rate is also a good measure of the beam luminosity. The efficiency of the BBC trigger for non-singly diffractive (NSD) p+p cross-section has been estimated at 86% during the 2001/2002 run [52].

The **Central Trigger Barrel** shown in figure 3.11 consists of 240 scintillator slats arranged cylindrically around the outside of the outer TPC-radius and covering $|\eta| < 1.0$. It's purpose is to measure charged particle density within this pseudo-rapidity range over the full azimuth. The scintillator

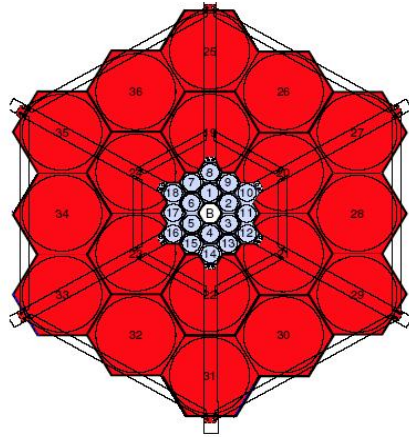


Figure 3.10: Schematic view of Beam Beam Counter (BBC) components. The active components are the 18 small tiles (blue) arranged in a hexagonal shape. The location of the beam-pipe is designated by "B".

slats consist of a radiator, light guide and a photo-multiplier tube (PMT). The accuracy of the multiplicity measurement is $\approx 3\%$ for $N_{ch} > 1000$ and the average occupancy for Au-Au collisions is $\approx 10/\text{slat}$. Since the CTB is a fast detector and is read-out every bunch-crossing it can also be used in this analysis to identify TPC tracks that have matching hits in the CTB. This is useful for identifying tracks from pile-up events which is explained in more detail in section 4.1.3.

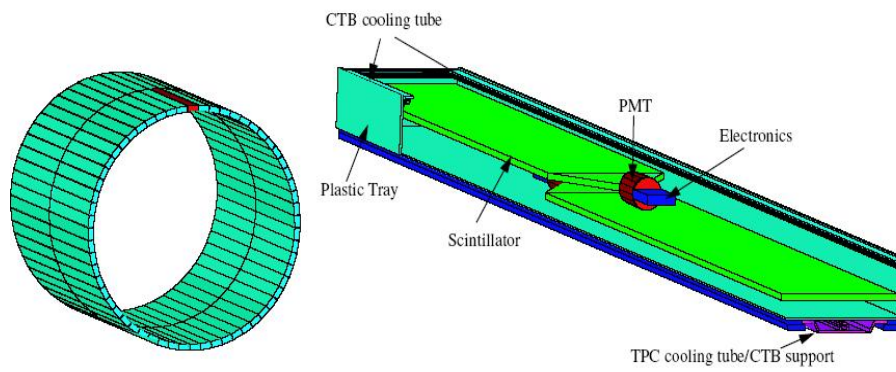


Figure 3.11: Schematic view of Central Trigger Barrel (CTB) components. The rectangular radiators have dimensions of 1cm x 21cm x 112/130cm

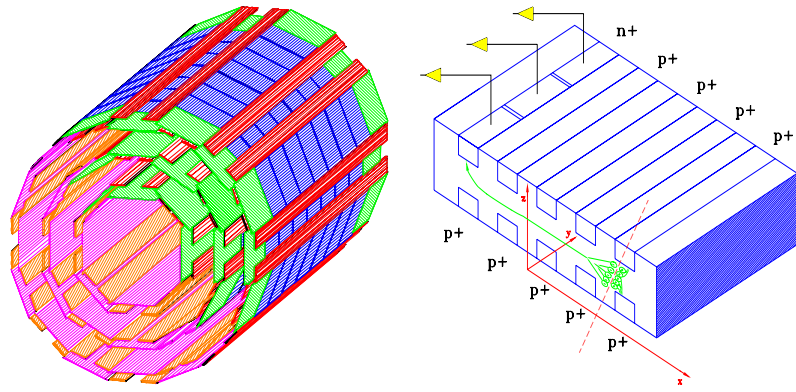
3.2.4 Silicon Vertex Tracker (SVT)

The Silicon Vertex Tracker was introduced into the STAR detector in the second year of RHIC running. It is a three barrel micro-vertex detector based on solid-state silicon drift detectors (SDD). The design allows for high accuracy position resolution ($\approx 20\mu m$) close to the primary interaction vertex, thereby improving the vertex resolution from the TPC.

The main physics goals for the SVT are to enhance the detection of short-lived strange and charmed particles at low p_T through the addition of high precision hits at the inner radii.

The SVT consists of a total of 216 wafers arranged on three concentric barrels of radii, 5.97cm, 10.16 and 14.91cm as shown in figure 3.12a). Each wafer is 63mm by 63mm and 280 μm thick. Figure 3.12b) shows the detail of a generic n-type silicon wafer. The p^+ strips, acting as cathodes, are implanted symmetrically on both top and bottom of the wafer. The applied potential has a gradient in drift direction "x" towards the anodes. The segmented anodes n^+ are located at the edge of the wafer and run parallel to the p^+ strips along the anode direction "y". The most important calibration issue of this technology consists in the precise measurement of the drift velocity in order to achieve an accurate hit resolution in drift direction. This is done by measuring the drift profile, i.e. drift distance vs drift time, for each wafer "on a bench" prior to installation using a laser scan method. The individual drift profiles are stored in a database and accessed during hit reconstruction.

A total of 103680 channels are read out at a rate of 25 MHz. The system is cooled by a closed water loop system, pumping approximately 40l/min to remove up to 1.6 kW of heat produced by the silicon chips. More technical details can be found here [48].



(a) Schematic of the wafer layout of the SVT (b) Diagram of a generic Silicon Drift Detector

Figure 3.12: Layout of SVT ladders (left). Generic Silicon Drift Detector (right). Taken from [48]

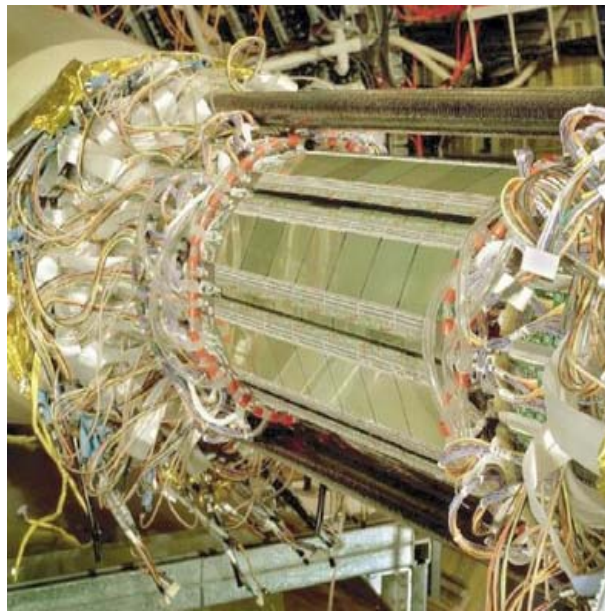


Figure 3.13: Photo of STAR Silicon Vertex Tracker (SVT) detector

Chapter 4

Analysis

4.1 Event reconstruction

Event reconstruction is the name of the procedure used to extract physical quantities from the data stored during data-taking periods. Depending on the size of the event, i.e. track multiplicity, and the number of events taken it can take several months to process the raw data into a form that is easily accessible to all STAR users.

4.1.1 Cluster and Track reconstruction

Charged particles traversing the TPC produce a trail of ionization which is converted into ADC-counts by the read-out electronics of the detector. As mentioned in the previous section each sector of the TPC contains 5690 read-out pads. During the drift time of the TPC these pads are sampled 512 times and thus give a total of ≈ 70 million pixels in all three dimensions. A charged track can leave a maximum of 45 hits in the TPC, which is equal to the total number of padrows.

The ADC data from all the different detectors are collected in a standard DAQ (Data Acquisition) output format, which contains the information at the level of digitized signals. Then the reconstruction software does the task of finding clusters of charge in each detector and converting their local coordinates into the global STAR coordinate system. At the reconstruction level several calibrations have to be applied off-line to account for non-uniformity of the TPC-magnetic field and geometrical alignment of the sub-detector systems.

Starting from the outermost padrow of the TPC the tracking algorithm TPT (TPC Tracker) identifies track seeds, i.e. a collection of three hits close in space, and constructs segments of tracks by extrapolating inwards towards the center of the TPC. In a second step a helical extrapolation is used to add more points to the track segments and extend them inwards and outwards. Once a hit is attributed to a track it is removed from the hit-collection. Once all hits have been associated to tracks a procedure of helix-merging is performed to identify low p_T tracks, with a large curvature, that have been wrongly identified as two separate tracks.

In a last step the found tracks are passed through a Kalman Filter algorithm. This fitting algorithm uses a more realistic description of the track helix accounting for energy losses and multiple scattering and their effect on the momenta of the tracks. Furthermore, hits that lie far from the fitted track are eliminated and a χ^2 value is attributed to each track. A more detailed description of the Kalman Track Filter can be found here [49].

4.1.2 Primary Vertex Finding and Event Selection

A particularity of the reconstruction in $p+p$ collisions as compared to heavy ion running is the low multiplicity of the track environment. A special ver-

tex finding code (Low Multiplicity Vertex finder “LMV”) was developed to deal with the challenge of determining the collision or primary vertex when there are on average 5.5 tracks present in an event. It requires that only those tracks which have matches to the Central Trigger Barrel (CTB) are considered in the calculation of the primary vertex position to avoid problems due to ‘pile-up’, which will be discussed in the next section. Further, the assumption is made that primary vertex is located somewhere along the beam line axis, this is known as ‘beam-line’ constraint. The z ordinate is then determined as being that value for which the χ^2 , calculated using the distance of closest approach of the tracks, is minimized.

The efficiency for reconstructing the primary vertex was determined by using Monte Carlo (MC) simulations. It is less than unity and varies as a function of event multiplicity and beam luminosity. In this study Monte Carlo generated $p+p$ events are ‘embedded’ into so-called ‘abort-gap’ events. An ‘abort-gap’ event is a real beam-gas event within the TPC that did not trigger the BBC’s and provides for a more realistic background environment.

The embedding technique works by propagating the Monte Carlo (HIJING, PYTHIA) produced particles through the STAR detector simulation (GEANT) and then creating ADC counts in the slow simulators of the different detectors. These simulated counts are then combined with the real ADC counts from real particles and passed to the event reconstruction where tracks are generated. The reconstructed event characteristics can now be compared to the input characteristics from the MC event. The vertex distributions for the simulation and the reconstruction can be seen in the left panel of figure 4.1. It clearly shows that some events are lost in the reconstruction but nevertheless the shape of the distribution is conserved. A quantity $\Delta(PVz)$ is defined as follows:

$$\Delta(PVz) = PrimVtx(z)[MC] - PrimVtx(z)[reconstructed] \quad (4.1)$$

We denote the z-coordinate (along the beam-line) of the vertex as **PrimVtx(z)**. The probability distribution of $\Delta(PV(z))$ is shown in the right panel of figure 4.1. For those events where the software has found a vertex, we define good vertices as having a value of $\Delta \leq 2\text{cm}$, fake vertices are recorded if $\Delta > 2\text{cm}$. The remaining events are those where a vertex wasn't found.

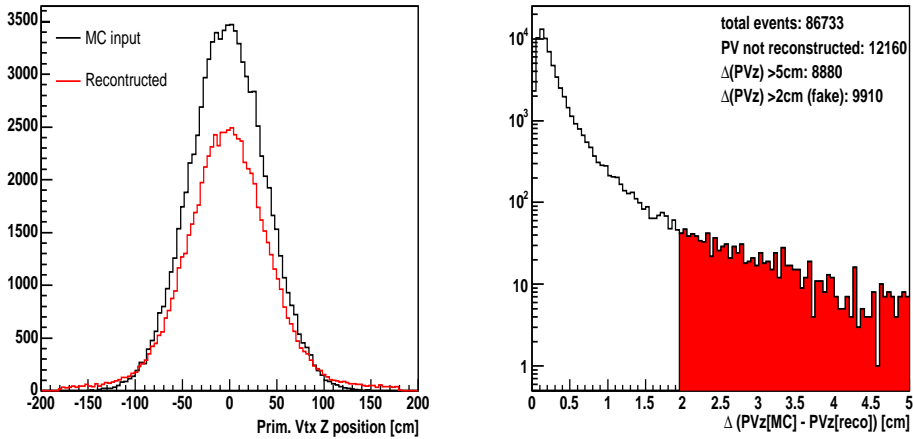


Figure 4.1: Left: Primary vertex position for Monte-Carlo simulation and reconstructed with vertex finder. Right: Distribution of quantity $\Delta(PV(z))$. Fake events are marked red.

As mentioned before the vertex finding probability is dependent on the multiplicity of the event, which we measure by number of MC global tracks. After separating the reconstructed tracks initiated from simulated particles from those of the background or beam-gas events we plot the global track (global track is used to designate both tracks from the vertex and secondaries) distributions for each event type, i.e. lost vertex, fake vertex and good vertex

Vertex Status	events	fraction
Total no events	86733	100 %
Lost vertex events	12160	14.0 %
Fake vertex events	9910	11.4 %
Good vertex events	64663	74.6 %

Table 4.1: Table of vertex "finding status" for events from the simulation study

as seen in the left panel of figure 4.2. The right panel of this figure is the probability for each type of vertex as a function of number of global tracks, obtained by dividing the distributions on the left by the distribution for all events.

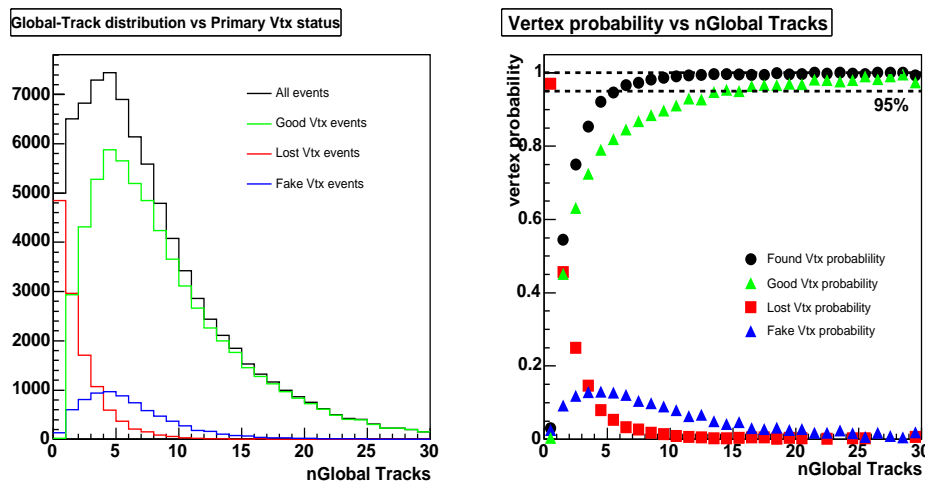


Figure 4.2: Left: Global track distributions for different event types. Right: Primary vertex efficiency η_{vtx} vs number of global tracks.

In a final step we need to convert our multiplicity scale (x-axis) from global tracks to primary tracks, since this is the standard multiplicity defini-

tion used in the analysis of real data. This is done by mapping the correlation between global tracks vs. primary tracks from the simulation study as seen in the left panel of figure 4.3. For each value of N primary track we then weight the vertex efficiency η_{vtx} vs global tracks by the probability according to this formula:

$$\eta_{Vtx}(nPrim) = \sum_{i=nGlob < nGlob} \eta_{Vtx}(i) * prob(i, nPrim) \quad (4.2)$$

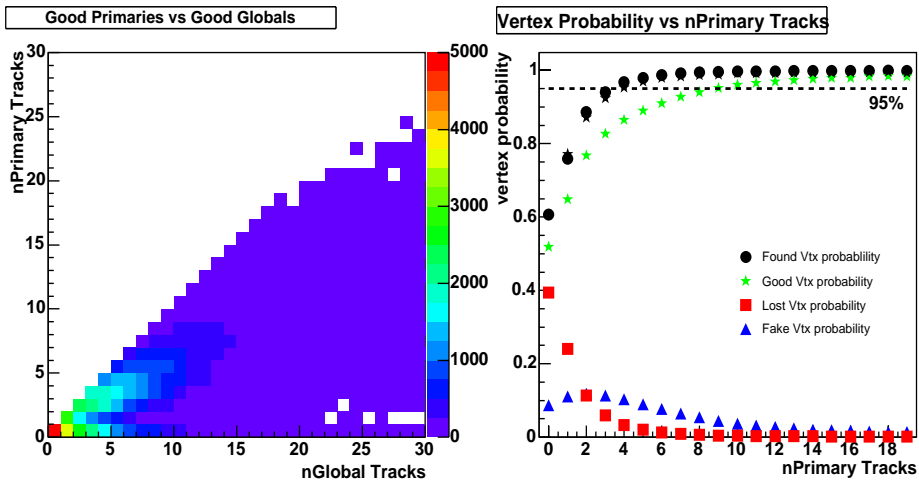


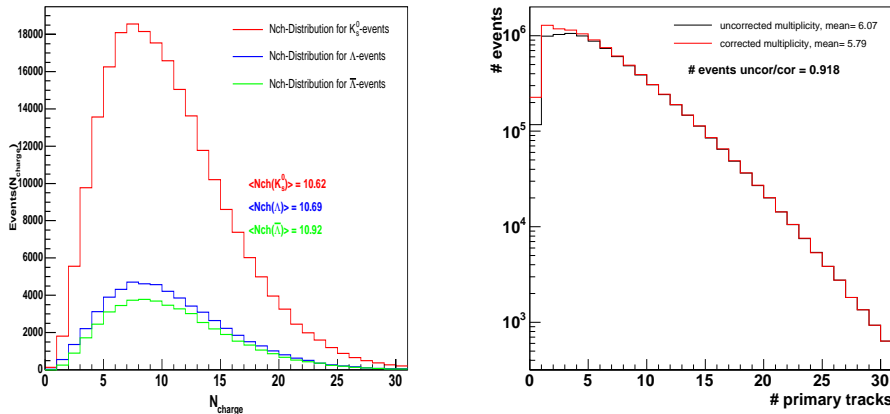
Figure 4.3: Left: Correlation between nPrimary tracks vs nGlobal tracks from Hijing events. Right: Primary vertex finding efficiency vs. number of primary tracks

The result of can be seen in the right panel of figure 4.3. These efficiencies can now be applied in the analysis after determination of the primary multiplicity. This correction has to be applied separately to the signal and to the normalization since their distributions as a function of number of primary tracks are different.

For the analysis in this thesis only those events which had a valid collision

vertex within $\pm 100\text{cm}$ along z -direction, of the mid-point of the TPC were accepted. After this selection a total sample of 10.26 million minimum bias $p + p$ events were available for analysis.

In the right panel of figure 4.4 the multiplicity distribution of charged tracks at mid-rapidity is shown before and after primary vertex corrections. The correction adds additional low multiplicity events and thus result in shifting the mean slightly to a 5% lower value. On the left panel of this figure the multiplicity distribution of events with a strange particle candidate is shown. A clear bias to higher multiplicity events is seen with respect to the minimum bias sample. The difference between the particle species however is very small.



(a) strange particle events

(b) minimum bias events

Figure 4.4: Left: Multiplicity distributions for events with strange particle candidates (left) and minimum bias events before and after vertex correction (right).

The relevance of this difference will become clear when we apply the computed primary vertex efficiency η_{Vtx} separately to our signal distribution

(K_s^0 and Λ) and the event normalization of our analysis.

Finally, the vertex reconstruction efficiency varies with beam luminosity (which varies over time) as shown in figure 4.5 and thus introduces a statistical fluctuation to the fraction of accepted events vs the total number of events. This variation of 3% has to be included in our systematic normalization uncertainty, which will be discussed in chapter 5.

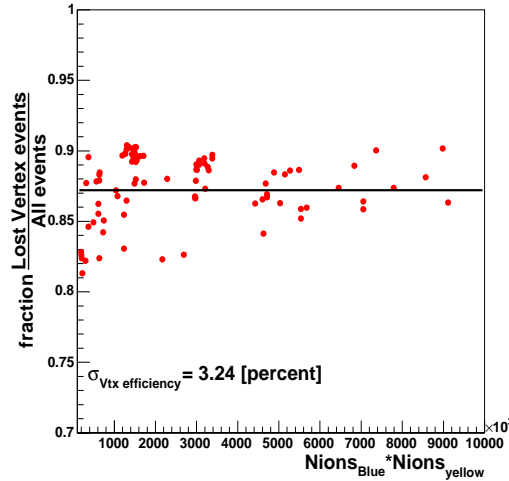


Figure 4.5: Percentage of lost vertex events as a function of the product of N_{ions} in the blue and yellow proton beams. This quantity is proportional to beam luminosity as shown in equation 4.3. The line shows the mean value of all measurements.

Cut	Both fields	Reversed Full F	Forward Full F
recorded	13'129'650	9'528'839	3'600'811
Found Prim Vtx	11'322'404	8'194'802	3'127'602
Found Prim Vtx, $Z < 100cm$	10'267'524	7'449'820	2'817'704

Table 4.2: Summary of events statistics after event selection cuts.

4.1.3 'Pile-up'

The STAR experiment triggers on the non-singly diffractive (NSD) $p + p$ cross-section which is small ($\approx 30\text{mb}$ as measured here [52]) compared to heavy ion collisions and therefore the luminosity of the RHIC beams was optimized in order to maximize the collision rate. The beam luminosity is defined by equation 4.3 where k_b is the number of filled bunches in each beam (56), $N_{1,2}$ are the number of ions in each bunch, f_{rev} is the frequency of revolution (78kHz) and σ is the beam width in either direction.

$$L = \frac{k_b f_{rev} N_1 N_2}{2\pi\sigma_x\sigma_y} \quad (4.3)$$

During the 2001/2002 run the luminosity varied from $5 \times 10^{28}\text{cm}^{-2}\text{s}^{-1}$ to $5 \times 10^{30}\text{cm}^{-2}\text{s}^{-1}$. Unfortunately, this high beam luminosity results in bunch-crossings that occur more frequently than the total drift time of the TPC, about $\approx 40\mu\text{s}$, which is the time to read-out the full volume of the TPC. Therefore there is a significant probability that two collisions are reconstructed as the same event. This occurrence is commonly called 'pile-up' since particle tracks from two or more events are mixed together in the same event and thus get reconstructed as one.

Pile-up events are hard to identify without inspecting the events one-by-one, and no attempt has been made to eliminate these events from the data taken. However since we know that the pile-up probability is a function of beam luminosity we can observe certain quantities over time and look for correlations with beam luminosity.

For example, the mean number of global tracks, meaning all tracks including primary and secondary tracks, is a quantity that should not vary for a given collision system, centrality and energy. However, this quantity is not constant over time in $p + p$ running and can be plotted against average lu-

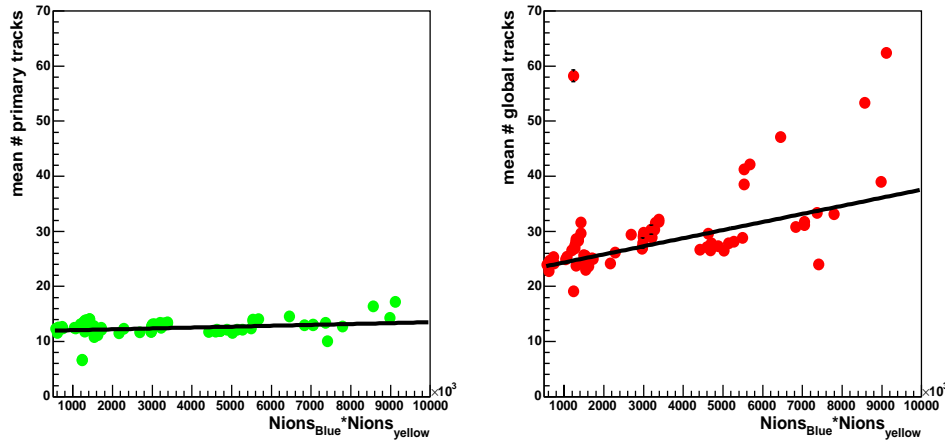


Figure 4.6: Mean number of primary (left) and global (right) tracks as a function of beam luminosity

minosity, measured once per run, as seen in the right hand side of figure 4.6. Indeed there is a correlation between the luminosity and the mean number of global tracks which is an indication for additional tracks from pile-up events.

The mean number of primary tracks, i.e. only tracks originating from the primary vertex, is shown on the left hand side of the same figure. It also shows some fluctuations with luminosity although to a much lesser extent. This can be understood since it is unlikely that tracks from pile-up events would appear to originate from the same vertex as the triggered vertex given our 'wide' vertex distribution (see figure 4.1). Thus, by matching the tracks to the event vertex we have created a quantity that is quite 'immune' to pile-up effects. Therefore this quantity will be used in the following thesis as the standard event multiplicity observable.

4.2 V^0 particle reconstruction

4.2.1 particle identification

The neutral strange " V^0 " particles presented in this thesis were identified by the predominant channel of their weak decay into charged daughter particles. The following decay channels with corresponding branching ratios (b.r.) were analyzed:

$$K_s^0 \rightarrow \pi^+ + \pi^- \quad (68.6\%) \quad (4.4)$$

$$\Lambda \rightarrow p + \pi^- \quad (63.9\%) \quad (4.5)$$

$$\bar{\Lambda} \rightarrow \bar{p} + \pi^+ \quad (63.9\%) \quad (4.6)$$

Negatively and positively charged tracks are paired together to form V^0 -candidates. This name has its origin in first bubble chamber photographs where the decay look like 'V' and the '0' denotes a neutral particle.

The charged daughter particles can then be identified within a certain momentum range via their ionization energy loss (dE/dx) in the TPC. This quantity can be plotted vs. total momentum of the particle and allows to identify pions, kaons and protons within a certain momentum range as seen in figure 4.7. The theoretical formula of ionization losses of charged particles in matter was derived by Bethe-Bloch and shown in equation 3.1. We define a quantity N_σ , as shown in equation 4.7, which is a measure of how 'far', in units of gaussian σ , the measured dE/dx is from the theoretical prediction for a given particle.

$$N_\sigma = \frac{dE/dx_{measured} - dE/dx_{Bethe-Bloch}}{\frac{r}{\sqrt{n}} dE/dx_{measured}} \quad (4.7)$$

Here n is the number of dE/dx measurements along a track and r is the resolution which has to be estimated experimentally. We use N_σ to identify the V^0 -daughters as π 's in the case of K_s^0 or as a pion and a proton for the Λ decay. Additional cuts are then applied based on the topology of the decay to further reduce combinatorial backgrounds.

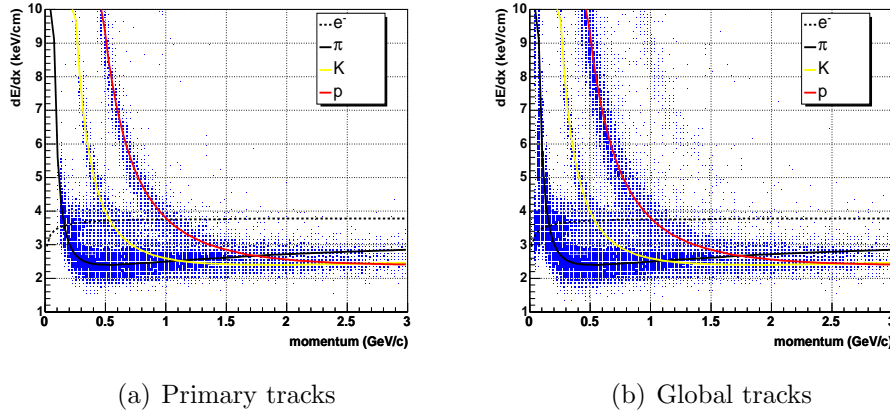


Figure 4.7: Track dE/dx vs total momentum for primary (left) and global (right) tracks. Lines represent Bethe-Bloch parametrizations. Tracks are required to have minimum 10 hits.

Figure 4.7 shows the distinct bands of different charged particles in the plane of dE/dx vs momentum. For primary tracks on the left pions are predominant whereas for global tracks on the right side the fraction of protons is increased and there is even a hint of the deuteron band to the right of the proton band.

4.2.2 Topological cuts in V^0 analysis

As mentioned in the previous section further cuts have to be applied to reduce combinatorial backgrounds. This is done by cutting on what are

called the topological variables of the decay. These variables are stored in the V^0 -collection and can be easily accessed. Figure 4.8 shows the different topological variables and their definitions.

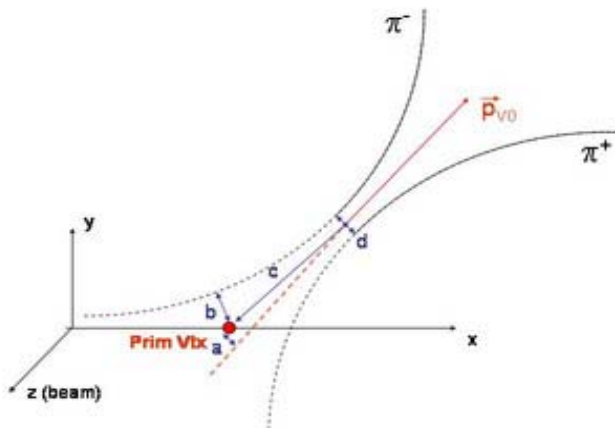


Figure 4.8: Schematic of V^0 -decay topology including all used cut variables: a) Distance of Closest Approach (DCA) to primary vertex(PV), b) DCA of V^0 daughter tracks to PV, c) V^0 decay length, d) DCA of V^0 daughters at secondary vertex. Shown is K_s^0 decay, for Λ replace π^+ with p.

The method used to determine the optimal value was based upon 2D-histogram of invariant mass vs. cut-variable as seen in figure 4.9. In these plots the range of values that yield signal is clearly visible by inspection and the adopted cut values are marked as black lines. The 'high density' areas of background V^0 's, outside the PDG-value of the K_s^0 (0.47-0.52), are excluded by these cuts. In table 6.2 the final cut-values of the analysis shown in this thesis can be found. Due to the finite primary vertex resolution (see figure 4.1) and the errors in the reconstruction of the V^0 momentum vector the

distance of closest approach (DCA) to primary vertex values are non-zero.

Cut	K_s^0	Λ	$\bar{\Lambda}$
V0 decay length (radial)	$> 2cm$	$> 2cm$	$> 2cm$
DCA of V0 to PrimVtx	$< 2cm$	$< 2cm$	$< 2cm$
DCA between V0-daughters	$< 0.9cm$	$< 0.9cm$	$< 0.9cm$
N(hits) daughters	> 14	> 14	> 14
N(σ) dE/dx	$< 3\sigma$	$< 3\sigma$	$< 3\sigma$

Table 4.3: summary of V^0 cuts

Figure 4.10 shows the invariant mass of K_s^0 and Λ after application of each cut. It is interesting to observe that for K_s^0 the decay length cut appears to reduce the background considerably, while for Λ the dE/dx has the most impact.

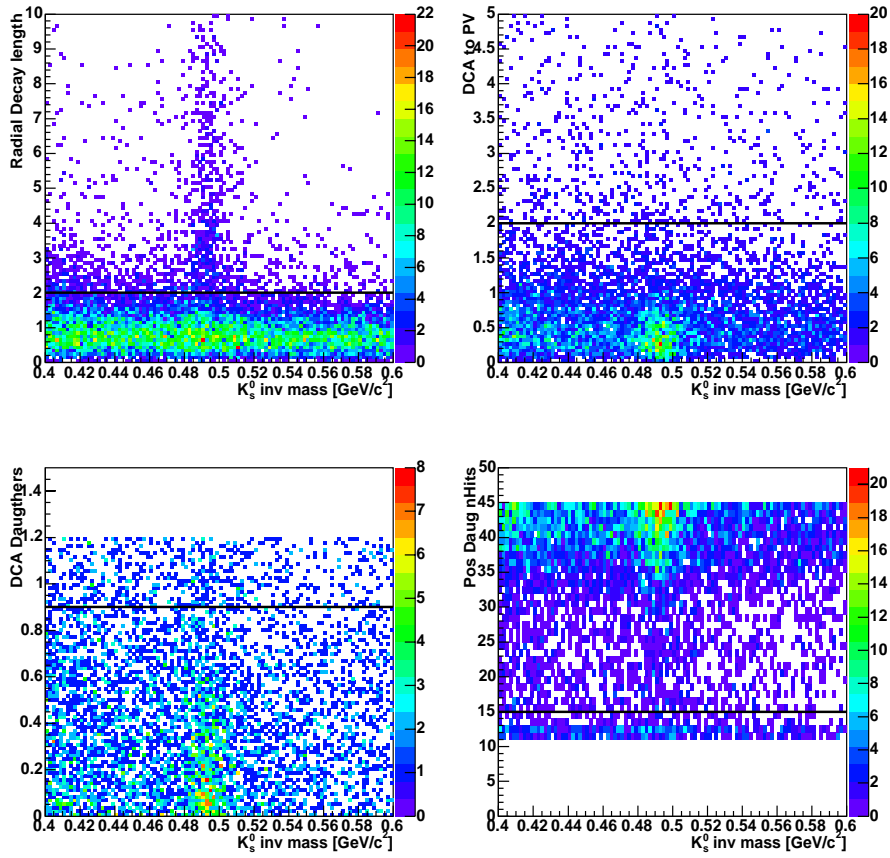


Figure 4.9: Invariant mass of K_s^0 plotted against a certain topological cut-variable

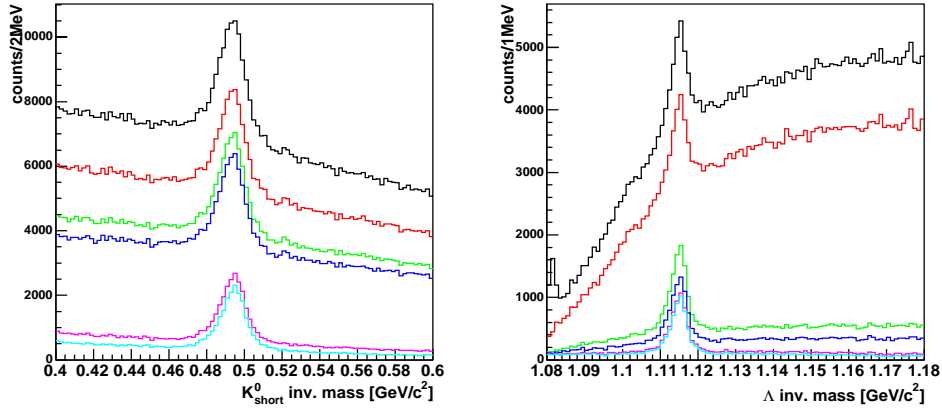


Figure 4.10: Invariant mass of K_s^0 (left) and Λ (right) after application of consecutive cuts in the following order: 1. no cuts (black), 2. N_{hits} (red), 3. dE/dx (green), 4. DCA to PV (blue), 5. 3D decay length (magenta) 6. radial decay length (light blue)

4.2.3 Cuts to reduce backgrounds from pile-up

Now let's turn to the V^0 vertices which are formed by combining two global tracks applying certain criteria that will be explained in the next chapter. It is reasonable to assume that since the global tracks are affected by 'pile-up' the combinations will be too. Indeed, the left panel of figure 4.11 shows how the number of V^0 candidates fluctuates as a function of beam luminosity (correlated with run-day) for different cuts.

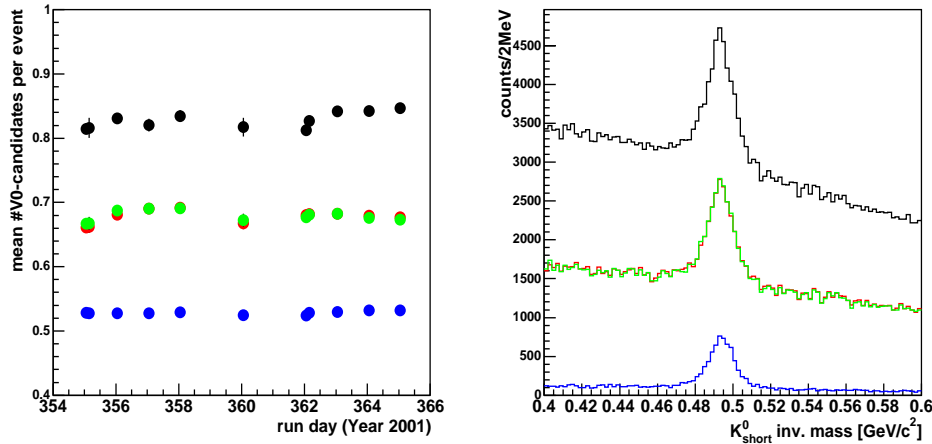


Figure 4.11: Left: Mean number of V^0 -candidates after certain cuts vs run-day (beam luminosity). Right: Invariant mass of K_s^0 . Colors described in text.

The black symbols in figure 4.11 are the mean number of V^0 's before applying any cuts. The green symbols are the result when applying CTB-matching of at least 1 daughter track. The red symbols (partly invisible) are the result for V^0 's that have a DCA to PV of less than 2cm. And finally the blue symbols represent the mean number of V^0 -candidates when applying all cuts (see table 6.2. This figure illustrates that by applying tighter cuts

the variation in the V^0 -yield vs. beam luminosity, is diminished and thus the contamination from 'pile-up' events is lessened. Thus figure 4.11 clearly shows that applying CTB-matching or tight DCA cuts are equivalent.

Another way of confirming this is shown in figure 4.12. We know that any track matching a hit in the CTB must be part of the triggered event. We can therefore match the V^0 -daughter tracks to CTB-hits and by this method select V^0 's that must be from the triggered event. Then the DCA to primary vertex distribution for V^0 's that have a certain number of CTB-matched daughter tracks can be plotted. Clearly, there is a correlation between these two variables and by applying a stringent cut on DCA one will automatically select V^0 's that have 1 or 2 CTB-hits and therefore must originate from the triggered event. The DCA-method will be used in the following analysis to minimize the impact of V^0 's from pile-up events.

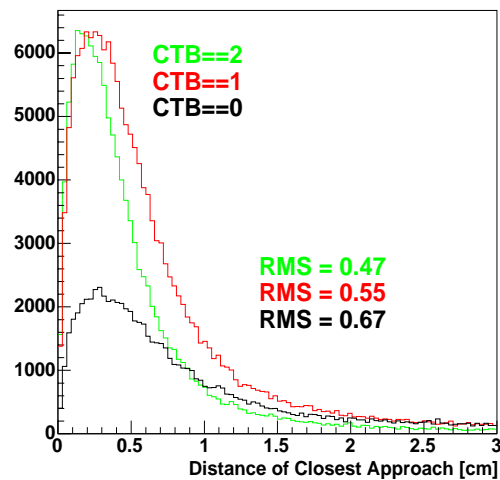


Figure 4.12: DCA to PV distribution for V^0 's with 0,1 or 2 daughter tracks matching CTB-hits

4.2.4 Yield extraction from invariant mass

From the final invariant mass distributions, shown in figure 4.13, a yield for each p_T -bin can be extracted. We compared two different methods of subtracting the residual background from the signal peak and thereby obtaining the raw yield. First, a Gaussian function can be fitted to the signal with a polynomial function to represent as background. This method is necessary when the background has a non-linear shape. The second method, referred to as 'bin-counting', consists of defining three regions in the invariant mass distribution, one in the (signal+background) interval around the peak and two in the pure background intervals above and below the peak. By counting the entries in the (signal+background) region and subtracting the counts from the regions that contain "pure" background we obtain the yield. Of course the summed width of the background regions has to be equal to the width of the (signal+background) region. This method assumes a linear background shape and is only applicable if this is the case. From figure 4.14 and 4.15 it can be seen that the linearity of the background depends on the p_T of the candidates and therefore each method may be more or less suited for a given p_T . Our final numbers are extracted using the bin-counting method for the signal and a polynomial background fit. The differences between the two methods are accounted for in the systematic errors.

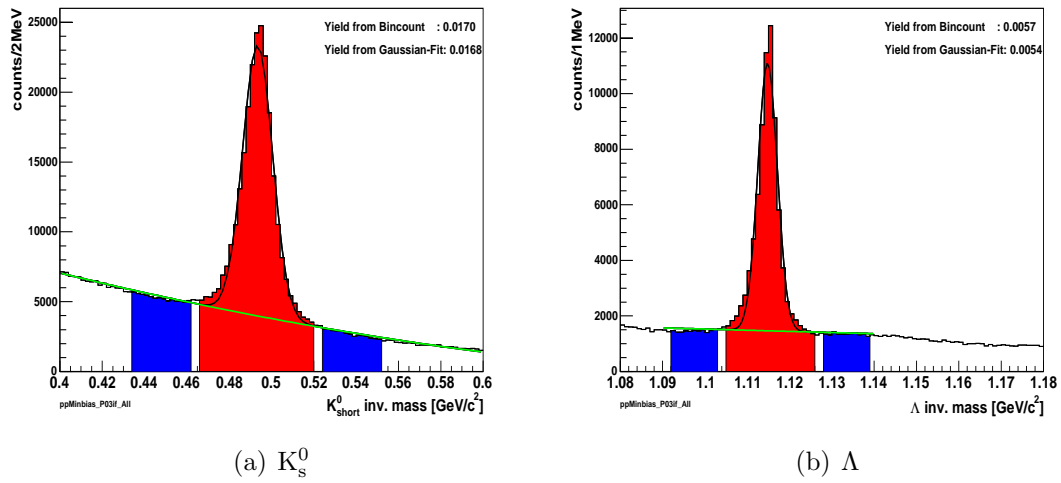


Figure 4.13: p_T -integrated invariant mass distribution of a) K_s^0 and b) Λ after final cuts. Signal region is red, background is blue

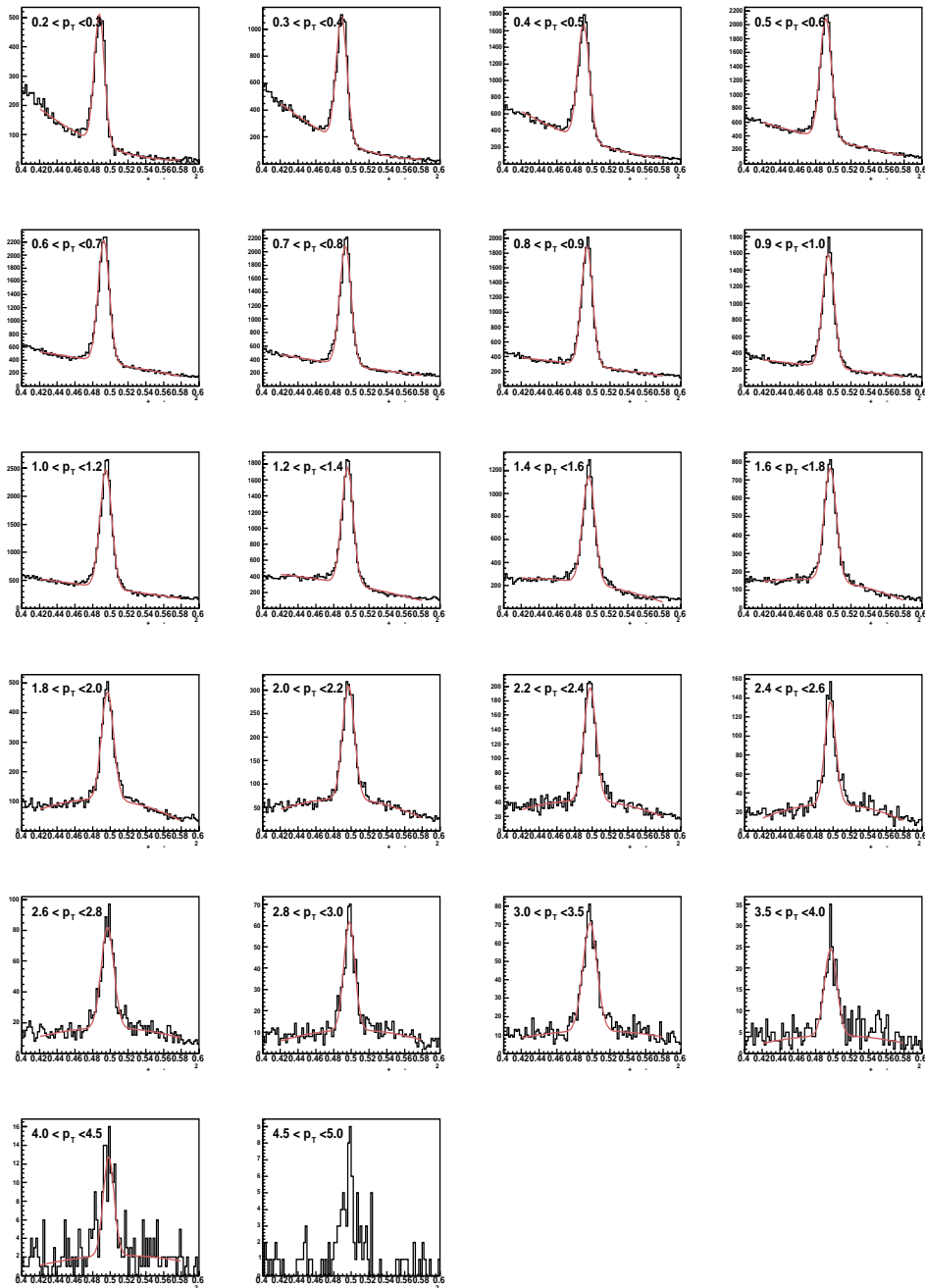


Figure 4.14: Invariant mass of K_s^0 in the 22 p_T -bins. Numerical Values are given in GeV/c. Red line is gaussian plus polynomial fit.

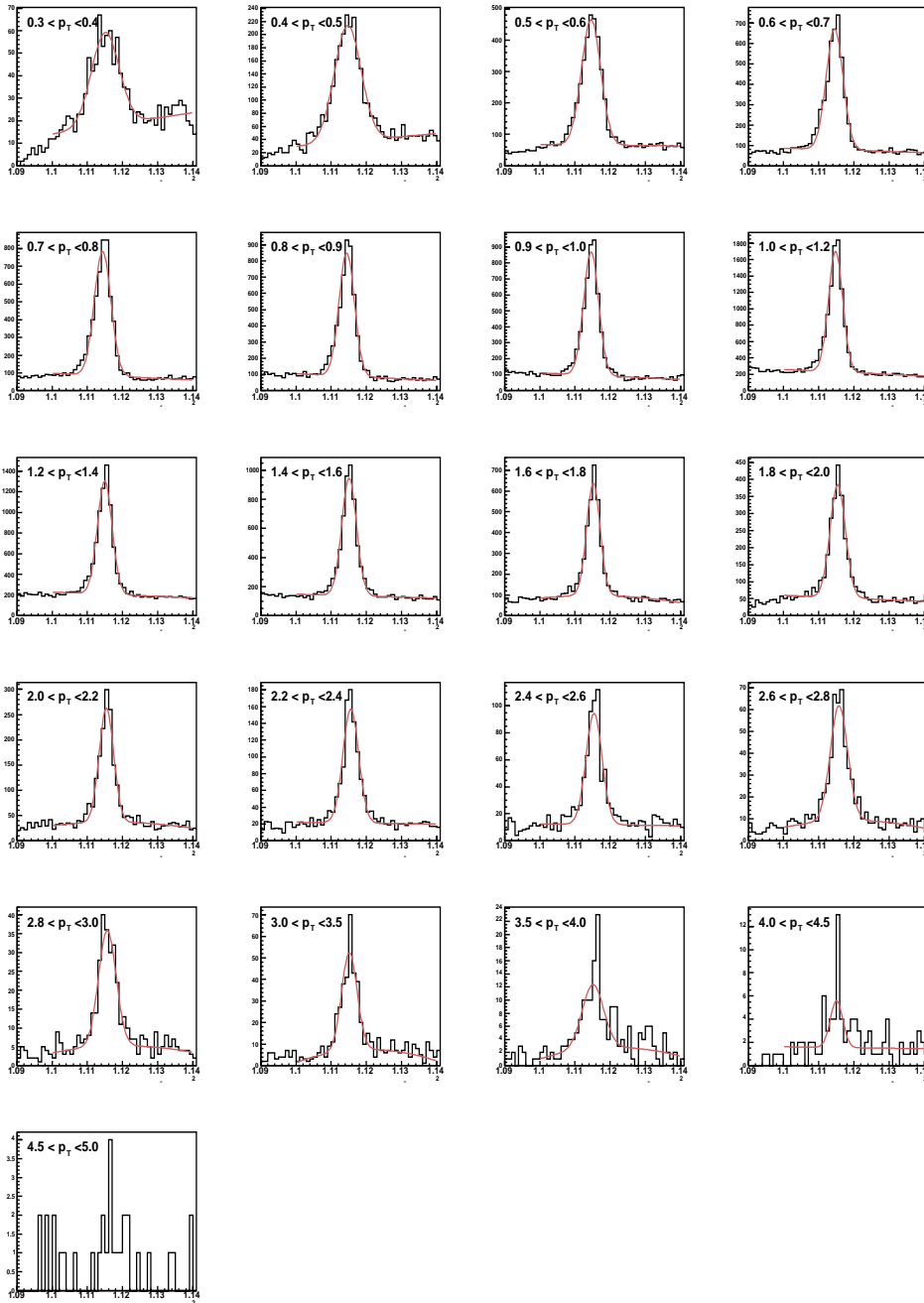


Figure 4.15: Invariant mass of Λ in the 21 p_T -bins. Numerical Values are given in GeV/c. Red line is gaussian plus polynomial fit.

4.2.5 Invariant mass peaks vs p_T

The position and width of the reconstructed K_s^0 and Λ mass peaks were analyzed as a function of p_T . To first approximation we have fitted gaussian distributions to the particle peaks and extracted the center and the gaussian width σ . For K_s^0 we observe a shift in mass of up to 10 MeV for the p_T region < 1.5 GeV/c with respect to the PDG value as seen in figure 4.16. For Λ a shift is also observed although it is much less significant and deviates at most by 1.5 MeV with respect to the PDG value as seen in figure 4.17. The width of the peaks are also shown and are wider than the PDG values due to the experimental momentum resolution.

These shifts have been observed in previous STAR V^0 analysis and have been identified as detector related issues. The energy loss of soft pion daughters is not well accounted for in the event reconstruction and these small momentum shifts can impact the invariant mass calculation. Also, the reason for a more pronounced effect in K_s^0 with respect to Λ is due to a higher Q-value of the K_s^0 decay.

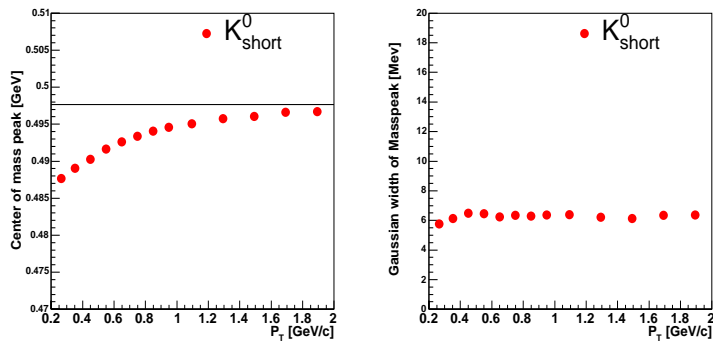


Figure 4.16: Mean and width of the gaussian fit to the K_s^0 mass peaks in the first 13 p_T -bins

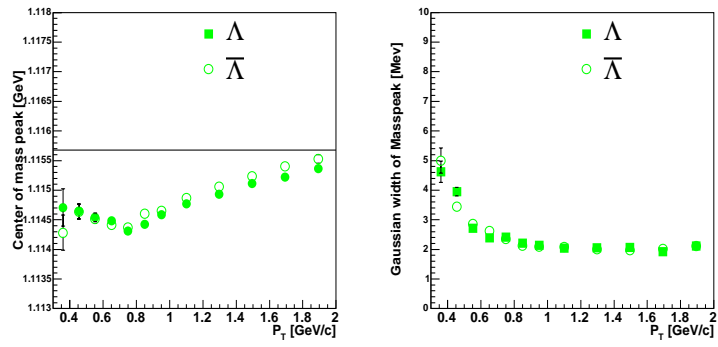


Figure 4.17: Mean and width of the gaussian fit to the Λ and $\bar{\Lambda}$ mass peaks in the first 12 p_T -bins

4.3 Corrections

4.3.1 Applying vertex corrections to spectra

In order to account for the particle yield losses due to the low vertex efficiency one more step has to be done before obtaining the final p_T -spectra. The data are analyzed in classes of different multiplicity and a separate p_T -spectra is extracted for each class.

$$N_{events}(VtxCorrected) = \frac{N_{events}(uncorrected)}{\eta[LostVtx]} \quad (4.8)$$

$$Yield(p_T) = \frac{1}{N_{events}(VtxCorrected)} \sum_{mult} \frac{Yield(p_T, mult)}{\eta[GoodVtx](mult)} \quad (4.9)$$

The corrected number of events is obtained by dividing by the integrated 'lost vertex' efficiency 0.86. Each spectrum is then divided by the 'good vertex' efficiency $\eta[Goodvtx]$ for a given multiplicity class, since both lost and fake events will not produce any particle signal, and then a summation is performed to retrieve a minimum bias spectrum. Finally the summed spectrum is normalized by the total number of events, including the events that were lost due to vertex inefficiency.

4.3.2 Efficiency and acceptance corrections

A large fraction of the produced strange particles in the collision are not reconstructed experimentally since the detectors geometrical acceptance and efficiency are limited. Additionally, the off-line cuts, which are applied in order to reduce the combinatorial background, also reduce the raw signal.

In order to determine the efficiency for each particle species and as a function of transverse momentum a process called embedding is applied.

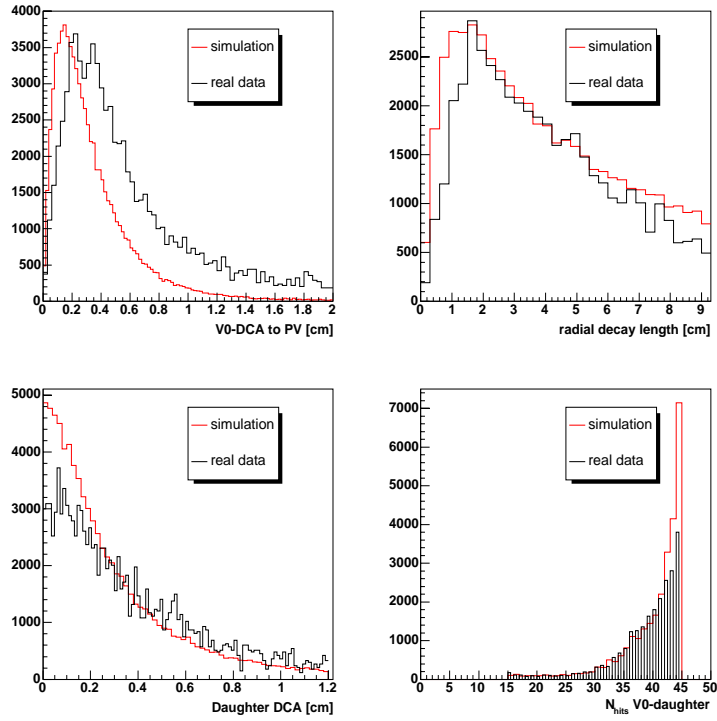


Figure 4.18: Comparison of the topological distribution variables for K_s^0 between real data and simulation.

This process consists of producing particles with Monte Carlo simulations (HIJING) and embedding these into real events using the information of the found primary vertex to determine where to initiate the HIJING particles [39]. This provides us with a realistic background track environment for finding the embedded particles. The embedded particles are also given a realistic, exponential transverse momentum distribution.

These particles are then propagated through the STAR detector simulation using the GEANT code, which simulates the particle interactions with the detector material and determines its trajectory. The so-called "slow simulators" create hits in the detectors and simulate ionization. This is used by the TPC response simulator (TRS) which converts the simulated TPC ionization into ADC counts. The simulated ADC and the raw data ADC counts are then mixed and reconstructed as a new event using the same software. An additional software tool creates associations between reconstructed and simulated tracks and stores them in an array. This array can then be used to exactly determine which simulated tracks were reconstructed by the code and the efficiency can then be easily derived as a function of track p_T and pseudo-rapidity. The final result for K_s^0 and Λ is shown in figure 4.19. The raw yields can now be divided by this efficiency and the branching ratio of the corresponding decay to obtain corrected yields.

This method requires that the decay topology of simulated and real V^0 particles is similar. Figure 4.18 shows the cut distributions for real and simulated V^0 's. The largest differences are seen in the DCA distribution of V^0 to PV due to the mediocre precision of the primary vertex determination.

Due to the low multiplicity environment in $p + p$ collision only one MC-particle was embedded in each event. Checks were made to ensure that with this criterion, the reconstructed primary vertex position after embedding was

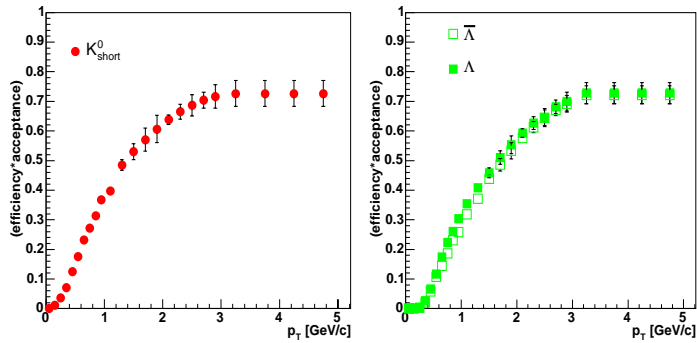


Figure 4.19: Total correction factor (efficiency * acceptance) for K_s^0 (left) and Λ (right) at mid-rapidity $|y| < 0.5$. This factor does not include the branching ratios.

the same as the original position within the vertex resolution.

4.3.3 Feed-down contributions to Λ

The measured Λ yield includes secondary Λ particles coming from weak decays of heavier hyperons, i.e. Ξ^- and Ξ^0 , and resonances, σ^* . In order to disentangle the primary Λ production from the secondary an estimation of this contribution, which is frequently called 'feed-down' is necessary. In the following the method of this correction is explained.

The considered weak decays are :

$$\Xi^- \rightarrow \Lambda + \pi^- (b.r. = 0.999) \quad (4.10)$$

$$\Xi^+ \rightarrow \bar{\Lambda} + \pi^+ (b.r. = 0.999) \quad (4.11)$$

There is also a contribution of Σ^0 in the inclusive Λ yield, however since this is a strong decay, and thus occurs at the primary vertex, no attempt to identify this contribution is made. Generally, Λ yields are understood to

be inclusive, i.e. including the Σ^0 yield. The contributions from $\Sigma^*(1385)$ resonance, measured by STAR in $p + p$ collisions [53], which has a decay channel directly into Λ (b.r. 88%), will be estimated by an overall factor of 9.5%.

The Ξ^- was measured in $p + p$ collisions by another member of the group and the results can be found here. The Ξ^0 is not measured in STAR and it is assumed to have the same yield as Ξ^- . In order to obtain the correction vs p_T we need to obtain a p_T -spectrum of the secondary Λ coming from the Ξ^- decay. This is done via an embedding simulation using the measured Ξ^- inverse slope as explained in the previous section. Figure 4.20 shows that scaled MC-spectra fitted to the data.

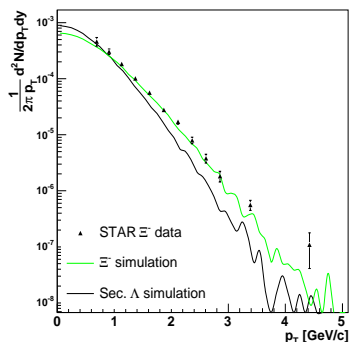


Figure 4.20: Transverse momentum distributions of simulated Ξ^- particles and their decay daughter Λ . The Ξ^- datapoints from the STAR measurement are shown as comparison and were measured here [86].

Now that we have the shape of the secondary MC- Λ spectrum we need to estimate how these particles influence reconstructed p_T -spectrum. Therefore we need to estimate the reconstruction efficiency of secondary Λ . This efficiency may be different due to the lifetime of the Ξ^- particle, $c\tau = 4.9\text{cm}$,

resulting in a decay away from the vertex and therefore a different topology of the Λ . Again we use Monte-Carlo simulation to obtain the reconstruction efficiency of secondary Λ as shown in figure 4.21.

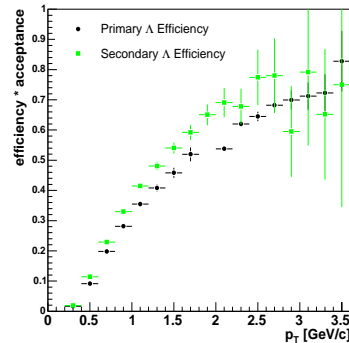


Figure 4.21: Total correction factors for primary Λ particles (black) and secondary Λ particles from Ξ^- decay (green).

It was also checked that secondary Λ from Ξ^0 decays have an identical efficiency as those from Ξ^- decays. Finally, using the 2 elements obtained by simulation we can estimate the 'feed-down' contribution as a function of p_T to the final spectrum:

$$Corrected(p_T) = Measured(p_T) \left[1 - \frac{Sec(p_T)R_{eff}(p_T)}{Measured(p_T)} \right] \quad (4.12)$$

In this equation enters R_{eff} which is the ratio of the secondary divided by the primary efficiency as shown in figure 4.21. The quantity $Sec(p_T)$ is the yield from secondary Λ as shown in figure 4.20. The final multiplicative correction factor vs p_T is seen in figure 4.22. The p_T -integrated value of this correction is about 13% on the yield.

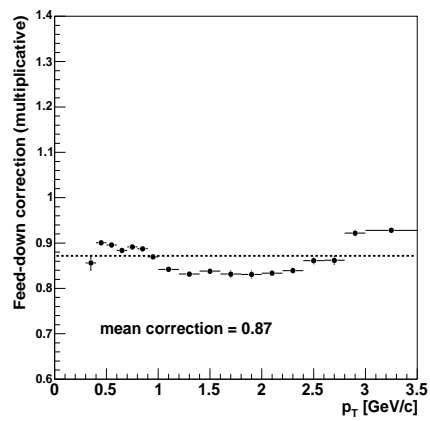


Figure 4.22: Final Feed-down correction factor vs. p_T .

4.4 V^0 -analysis using SVT information

The prospect of a silicon vertex detector (SVT) in STAR that enables to add additional position measurements of tracks close to the primary vertex is very interesting. Indeed the SVT is now so far integrated into the event reconstruction chain that tracks from the TPC can be matched to hits in the 3 layers of the SVT. This gives additional spatial resolution to tracks originating near the vertex.

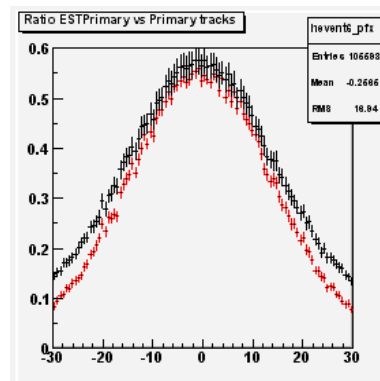


Figure 4.23: Matching efficiency for TPC tracks to SVT hits with the EST code package. X-axis is position of primary vertex along z in cm. Y-axis is ratio of primary tracks with at least 1 SVT hit divided by total number of primary tracks. Red and black curves show two different track definitions to estimate systematic error.

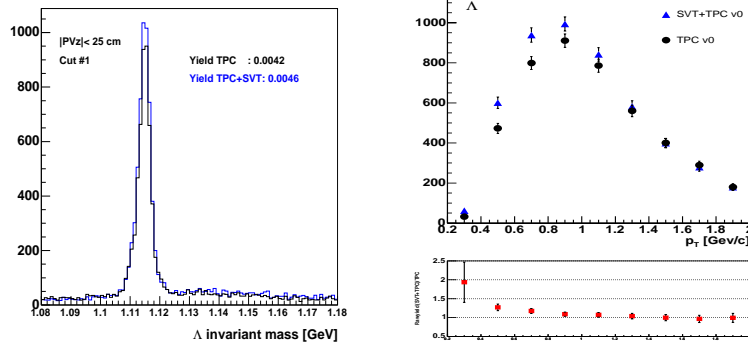
At this point independent tracking with the three SVT-layers cannot be done, however software exists to extrapolate tracks from the TPC to the SVT detector volume and match SVT-hits to tracks. This software uses a few parameters to define the “search-radius” on the SVT wafers and the tracks with added SVT-hits are stored in a separate track-collection. Figure

4.23 shows the fraction of primary tracks that are matched to at least one hit on the SVT as a function of the z-position of the primary vertex. This fraction peaks at $\approx 60\%$ for vertices that are within 10cm of the center of the SVT. Since the SVT is only 60cm long the strong drop of this efficiency at ± 30 cm is due to the limited acceptance.

The V^0 finder code runs the search for secondary vertices twice. First only 'pure' TPC tracks are considered, the second time all tracks are considered, i.e. also those that have matched SVT-hits. When a V^0 vertex is found, the number of SVT hits on each charged daughter is coded into the V^0 for further discrimination in the subsequent analysis.

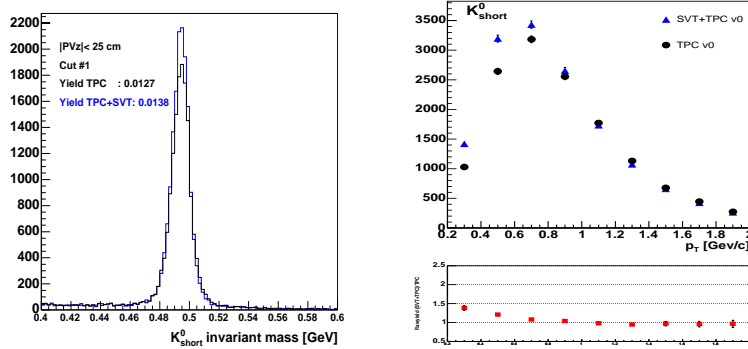
In the future, the physics analysis can be done using either collection of V^0 candidates, i.e. with or without SVT-tracks. In figure 6.1 and 4.25 we show the results with and without inclusion of the SVT. The p_T integrated raw signal improvement is currently $\approx 10\%$ for Λ and 8% for K_s^0 . More importantly the signal improvement in the lowest p_T bin is $\approx 40\%$ for K_s^0 and over 50% for Λ .

This enhancement will only be fully exploitable once an appropriate detector simulation is completed, which will allow efficiency correction of V^0 's with SVT-hits. The physics results presented in this thesis use V^0 's without SVT-hits.



(a) Λ invariant mass with and without SVT-hits (b) uncorrected yield vs p_T and ratio of SVT+TPC vs TPC only

Figure 4.24: Λ invariant mass for V^0 's with and without SVT-hits. Right plot shows the uncorrected yield vs. p_T .



(a) K_s^0 invariant mass with and without SVT-hits (b) uncorrected yield vs p_T and ratio of SVT+TPC vs TPC only

Figure 4.25: K_s^0 invariant mass for V^0 's with and without SVT-hits. Right plot shows the uncorrected yield vs. p_T .

Chapter 5

Results

5.1 Results from V^0 -Analysis

5.1.1 Transverse Momentum Spectra

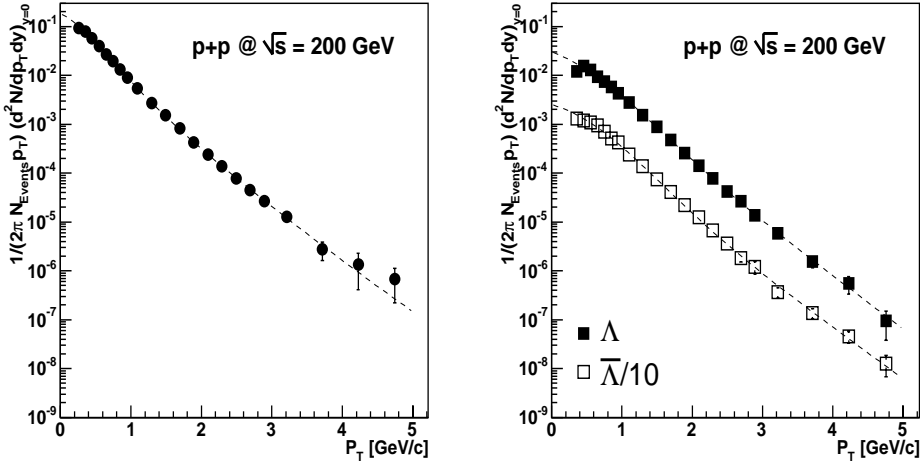


Figure 5.1: Corrected p_T -spectra for K_s^0 (left), Λ and $\bar{\Lambda}$ (right). Before feed-down correction from Ξ^- . Statistical errors only.

In figure 5.1 corrected p_T -spectra for K_s^0 , Λ and $\bar{\Lambda}$ are shown. The measurement is limited at low p_T by the TPC acceptance for charged particles at mid-rapidity to greater than 0.3 GeV/c for Λ / $\bar{\Lambda}$ and greater than 0.2 GeV/c for K_s^0 . In order to extract $\langle p_T \rangle$ and dN/dy it is necessary to fit the data with an appropriate parametrization and extrapolate the fit function over the full p_T range, i.e. $0-\infty$ GeV/c. In the past, the most commonly used parametrization for hadron-hadron collisions have been **exponentials in transverse mass** (see eq. 5.2), inspired by Hagedorn's thermal models [54] (for the low p_T part) or **power-law functions**, (Eq. 5.3) in the case of spectra including high- p_T hadrons from mini-jets fragmentation[56].

$$m_T = \sqrt{p_T^2 + m_0^2} \quad (5.1)$$

Where m_0 is the rest-mass of the particle.

$$\frac{1}{2\pi p_T} \frac{d^2 N}{dy dp_T} = A e^{-\frac{m_T}{T}} \quad (5.2)$$

$$\frac{1}{2\pi p_T} \frac{d^2 N}{dy dp_T} = A \left(1 + \frac{p_T}{p_0}\right)^{-n} \quad (5.3)$$

Here T , n and p_0 are fit variables. Parameter T in exponential functions is often referred to as **"inverse slope"** parameter. However, since this measurement has sufficiently small errors to constrain both the low and high p_T end of the spectrum a simple parameterizations with either of the above functions does not yield sufficiently small χ^2 fit values. The best fit results, as measured by χ^2 , were obtained from a combination of m_T -exponential and power-law functions. The m_T -exponential equation is a better fit at low p_T , whereas at high p_T the power-law describes the shape of the spectra better. Two variants of composite functions were tested and are defined below by equations 5.4 and 5.5.

$$\frac{1}{2\pi p_T} \frac{d^2 N}{dy dp_T} = C e^{\frac{-m_T}{T}} + D \left(1 + \frac{p_T}{p_0}\right)^{-n} \quad (5.4)$$

$$\frac{1}{2\pi p_T} \frac{d^2 N}{dy dp_T} = [C e^{\frac{-m_T}{T}}]_{p_t < x} + [D \left(1 + \frac{p_T}{p_0}\right)^{-n}]_{p_t > x} \quad (5.5)$$

We name equation 5.4 the 'inclusive composite' since it uses both the exponential and powerlaw over the full p_T -range and controls the contributions via the constant parameters C, D. Equation 5.5 will be referred to as 'exclusive composite' since it includes a sixth parameter x which controls the p_T -boundary between the exclusively exponential function and the exclusively power-law function. In addition the function is required to have a smooth derivative at $p_T = x$.

For the Λ and $\bar{\Lambda}$ spectra a slight variation of equation 5.4 is applied since it was noticed that the n -parameter of the power-law function tends to ∞ in an unconstrained fit. This asymptotic behavior of the power-law function is equivalent to an exponential function in p_T . Therefore, the second part of equations 5.4, 5.5 is replaced by an exponential in p_T and the final fit-functions are 5.6, 5.7. The fit is now well constrained and yields a good description of the Λ and $\bar{\Lambda}$ spectra.

$$\frac{1}{2\pi p_T} \frac{d^2 N}{dy dp_T} = A e^{\frac{-m_T}{T}} + B e^{\frac{-p_T}{T}} \quad (5.6)$$

$$\frac{1}{2\pi p_T} \frac{d^2 N}{dy dp_T} = [A e^{\frac{-m_T}{T}}]_{p_t < x} + [B e^{\frac{-p_T}{T}}]_{p_t > x} \quad (5.7)$$

The results of all the fits to the particle spectra are shown in table 5.1 and plotted in figures 5.2 and 5.3 with the values of χ^2 for all functions described previously. The fits to Λ and $\bar{\Lambda}$ are performed separately, once with and then without correction for feed-down from Ξ^- and Ξ^0 particles.

Particle	m_t -exponential	power-law	composite 5.4,5.6 (inclusive)	composite 5.5,5.7 (exclusive)
	χ^2/ndf	χ^2/ndf	χ^2/ndf	χ^2/ndf
Λ	8.3	4.2	1.5	1.3
$\bar{\Lambda}$	7.6	4.3	1.7	1.2
Λ (feeddown corr)	12.6	5.4	2.4	2.0
$\bar{\Lambda}$ (feeddown corr)	11.6	5.0	2.3	1.4
K_S^0	25.1	2.0	1.3	1.2

Table 5.1: A summary of χ^2/ndf values for all tested fit-functions to the different particle p_T -spectra.

Additionally, the agreement of the fit-functions with the data are shown in figure 5.2 and 5.3.

Finally the values for dN/dy and $\langle p_T \rangle$ are calculated from the mean of the two best fit-functions, as determined by the lowest χ^2/ndf , and tabulated in table 5.2.

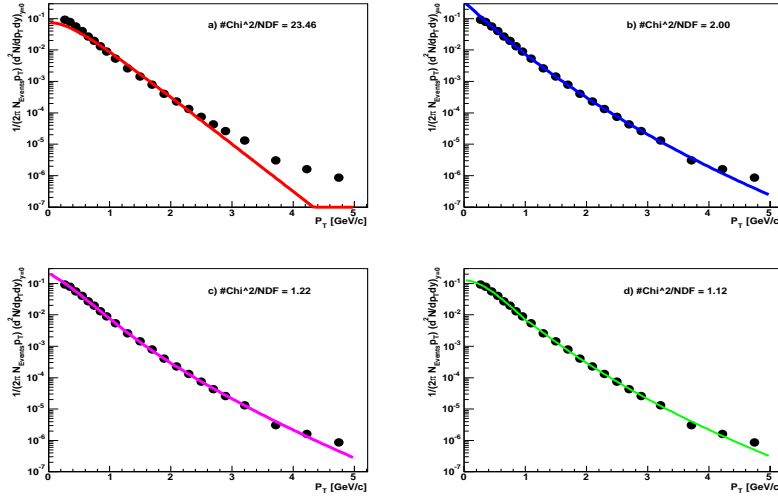


Figure 5.2: Fit-functions and their χ^2 values for corrected p_T -spectra for K_s^0 : a) m_T -exponential b) power-law c) composite(inclusive) d) composite(exclusive)

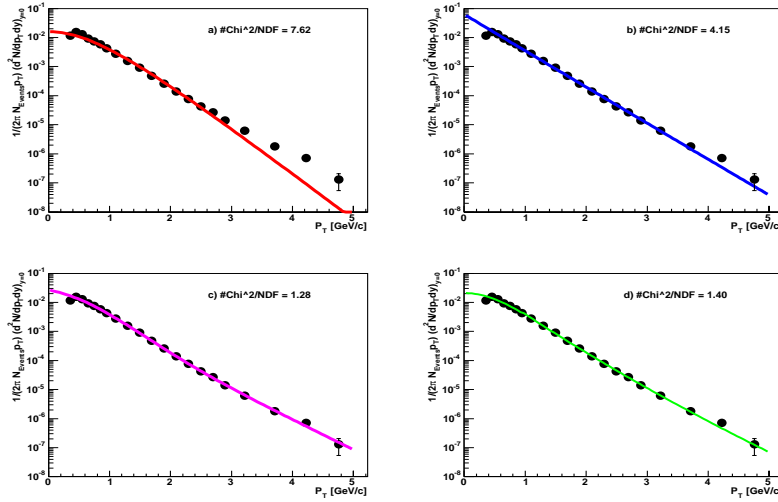


Figure 5.3: Fit-functions and their χ^2 values for corrected p_T -spectra for Λ : a) m_T -exponential b) power-law c) composite(inclusive) d) composite(exclusive)

Particle	yield (dN/dy) $ y <0.5$	feed-down corrected dN/dy $ y <0.5$	$\langle p_T \rangle$ (GeV/c) $ y <0.5$
Λ	0.0430 $\pm 0.0010(\text{stat}) \pm 0.0036(\text{syst})$	0.0333 $\pm 0.0009(\text{stat}) \pm 0.0032(\text{syst})$	0.77 $\pm 0.02(\text{stat}) \pm 0.04(\text{syst})$
$\bar{\Lambda}$	0.0402 $\pm 0.0010(\text{stat}) \pm 0.0036(\text{syst})$	0.0320 $\pm 0.0009(\text{stat}) \pm 0.0032(\text{syst})$	0.76 $\pm 0.02(\text{stat}) \pm 0.04(\text{syst})$
K_S^0	0.136 $\pm 0.003(\text{stat}) \pm 0.010(\text{syst})$	n.a.	0.60 $\pm 0.01(\text{stat}) \pm 0.03(\text{syst})$

Table 5.2: A summary of yields and $\langle p_T \rangle$ at mid-rapidity ($|y|<0.5$) including statistical and systematical errors. The feed-down corrected yields for Λ and $\bar{\Lambda}$ include contributions from Ξ and $\Sigma^*(1385)$.

5.1.2 Anti-particle to particle ratio

Once the transverse momentum spectra have been obtained for particle and anti-particle it is possible to produce the ratio of the yields vs p_T .

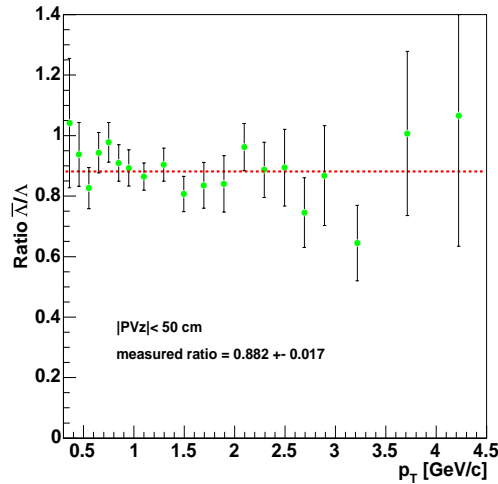


Figure 5.4: Ratio of $\bar{\Lambda}/\Lambda$ vs p_T in $|y|<0.5$. Dashed line is weighted fit to datapoints.

In figure 5.4 the non-feeddown corrected ratio of $\bar{\Lambda}$ to Λ is shown versus transverse momentum. Within statistical errors this ratio is constant with p_T . The mean value over the measured p_T -region is 0.882 and the value obtained from the composite fit extrapolation is 0.935 both consistent within statistical errors.

Particle	$\bar{\Lambda}/\Lambda$
measured p_T -range	0.882 ± 0.017
full p_T -range	0.935 ± 0.036

Table 5.3: A summary of $\bar{\Lambda}$ to Λ ratio at mid-rapidity ($|y| < 0.5$). Errors quoted are statistical only.

5.1.3 Systematic errors

Several sources of systematic errors have been quantified in this analysis. A summary of these uncertainties on the value of $\langle p_T \rangle$ and dN/dy can be found in table 5.4 shown in percent. Some of these errors may be correlated, such as for example the cuts and the yield extraction.

To obtain systematical errors we have performed the p_T spectra analysis for three different values of cuts, two methods of yield extraction, four different TPC sectors and two different magnetic field settings. Each time the standard deviation from the different measurements was determined and entered in the appropriate row of table 5.4. To obtain the total value of systematic uncertainty from data (row 1), the s.d. from the combined variation of all 11 settings was determined. The sum of systematical errors (row 4) is the geometrical sum of rows 1-3.

Systematic error source	K_s^0		Λ ($\bar{\Lambda}$)	
	$\frac{dN}{dy}$	$\langle p_T \rangle$	$\frac{dN}{dy}$	$\langle p_T \rangle$
Cuts	4.0	1.2	6.1	1.9
Yield extraction	7.8	1.1	2.5	0.9
TPC-Sector(ϕ) variation	3.1	0.4	2.0	0.7
Magnetic field setting	2.2	0.4	3.3	1.0
1) Syst. uncertainty from data	5.3	1.7	5.3	1.3
2) Syst. uncertainty from fit parametrization	4.9	3.7	6.3	4.7
3) Syst. uncertainty from normalization	3.2	n.a.	3.2	n.a.
4) Sum of all quoted syst. uncertainties	7.9	3.9	8.8	4.9

Table 5.4: A summary of systematic errors from various sources and their magnitude in percent

Here follows a brief discussion of the sources of these systematic errors.

1. **Cuts:** The off-line cuts that were applied to minimize the residual backgrounds also eliminate contamination from pile-up more or less effectively. The final cuts are a compromise between eliminating all background from pile-up with very stringent cuts and having a good efficiency allowing for high p_T reconstruction with loose cuts. The embedding simulation discussed in section 4.3.2 which does account for cut efficiencies is not perfect. Therefore certain cuts will be more or less well reproduced by this simulation and differences in the corrected yield may occur. Three different cut variations were used to determine the systematic error.
2. **Yield extraction method:** This figure estimates the systematic error from the two different methods of extracting raw yield from the

invariant mass histograms, discussed in the previous chapter.

3. **TPC sectors and magnetic field settings:** The analysis was performed as a function of azimuthal angle ϕ of the V^0 -decay in order to explore possible inhomogeneities in the TPC sectors and boundaries. Furthermore about 2/3 of the data were recorded with so-called 'Reversed' full magnetic field setting and 1/3 with 'Forward' full field setting. Previous STAR analyses have shown some systematic sensitivity to these different field settings due to inhomogeneities in the magnetic fields.
4. **Normalization:** This value estimates the systematic error from the vertex reconstruction and trigger efficiency as discussed in 4.1.2. It's cause is the strongly varying beam luminosity and the impact of this on vertex efficiency.
5. **Fit parametrization:** The systematic error from the different fit parameterizations to the spectra are summarized in this row. The s.d. from the three best fit-functions was used for each particle as determined by χ^2/ndf .

5.2 Multiplicity study

Thanks to the large statistics of our data sample I have been able to perform our analysis in different classes of charged event multiplicity (N_{ch}). We have divided the event sample into classes of event multiplicity, defined by the number of observed primary tracks within the STAR acceptance as seen in figure 5.5. The goal of this study is to measure the particle spectra for each class and determine $\langle p_T \rangle$ and dN/dy as a function of N_{ch} .

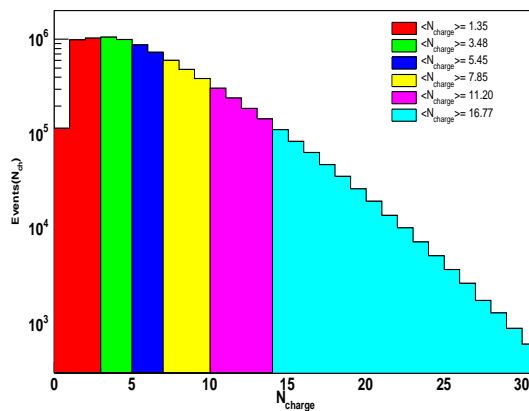


Figure 5.5: Definition of multiplicity classes used in this analysis with mean value per class

Table 5.5 shows the event classes and the number of events in each class that were used for this multiplicity study. The main constraint in choosing the boundaries being that sufficient statistics remain in each class to obtain a particle spectra up to sufficiently high p_T . The table also gives the values for the primary vertex efficiency corrected distribution of event multiplicity.

The p_T -spectra for the different multiplicity classes are shown in figure 5.6. No additional scaling has been applied and the increase of yield as a

	before primary vtx correction		after primary vtx correction		
Bin	Events	N_{ch}	Events	N_{ch}	$dN_{ch}/d\eta$ (uncorrected)
1	2580308	1.42	3338213	1.31	1.26
2	2441946	3.48	2603806	3.48	2.23
3	1912941	5.46	1964212	5.45	3.20
4	1752664	7.85	1778414	7.85	4.40
5	1049975	11.20	1058887	11.20	6.09
6	529690	16.77	533070	16.77	9.01
Σ	10267524	5.55	11276602	5.45	2.53

Table 5.5: Summary of number of events and mean N_{ch} for each multiplicity bin. Last column shows the corresponding uncorrected $dN_{ch}/d\eta$.

function of N_{ch} can be observed from these plots.

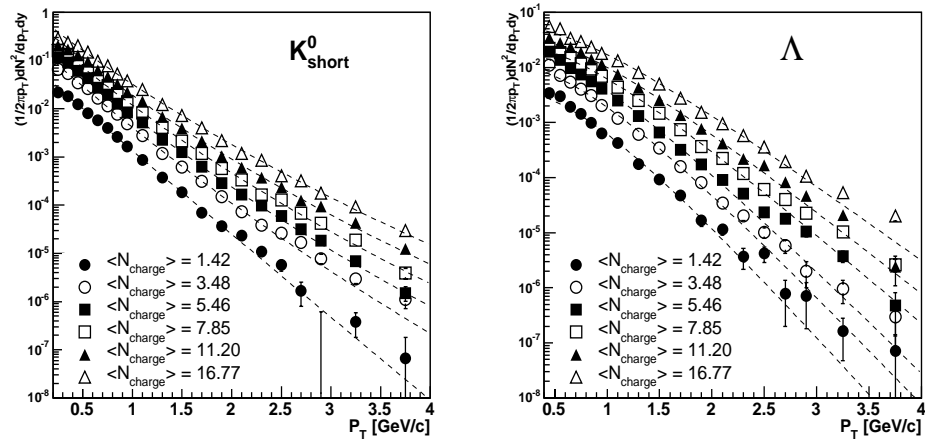


Figure 5.6: p_T -spectra for K_s^0 (left) and Λ (right) in the N_{ch} classes as described above. Dashed lines are composite function 5.4 and 5.6

5.2.1 $\langle p_T \rangle$ and dN/dy vs. event multiplicity

Using the three different fit-functions described in section 5.1.1 we can obtain values for $\langle p_T \rangle$ and dN/dy for each multiplicity class.

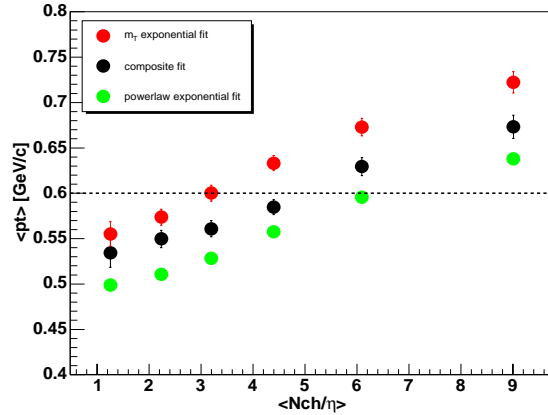


Figure 5.7: $\langle p_T \rangle$ vs $\langle dN_{ch}/d\eta \rangle$ for K_s^0 . Error bars are statistical and highly correlated.

As shown in figure 5.7 the $\langle p_T \rangle$ as a function of event multiplicity for K_s^0 increases nearly linearly. The increase in $\langle p_T \rangle$ from the lowest to the highest multiplicity bin is nearly 26% using the composite fit. As expected, the values of $\langle p_T \rangle$ obtained from the composite fit are systematically lower, those of the m_T -exponential fit and systematically higher than the power-law fit.

Figure 5.8 shows $\langle p_T \rangle$ of Λ vs event multiplicity. The shape of the increase for Λ seems to be slightly different than for K_s^0 , there may be a "level-off" a large N_{ch} . Again, the three different fit-functions were applied to give the reader a sense for the systematic dependence of this observable.

It has been previously observed in $\bar{p}+p$ at much higher $\sqrt{s} = 1.8$ TeV that there may be a mass ordering of correlation strength between $\langle p_T \rangle$ and N_{ch}

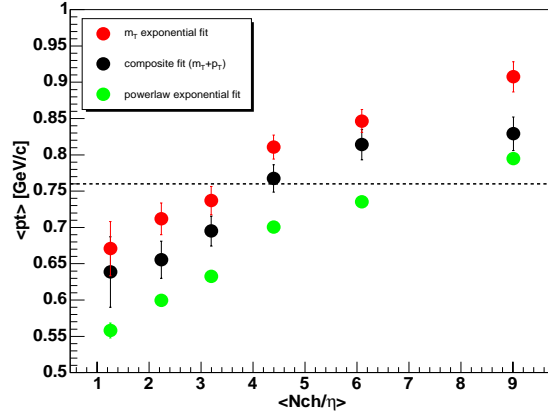


Figure 5.8: $\langle p_T \rangle$ vs $\langle dN_{ch}/d\eta \rangle$ for Λ . Error bars are statistical and highly correlated.

[70], which can also be said of the present data. The $\langle p_T \rangle$ for K_s^0 increases by $\approx 26\%$ whereas that of Λ by $\approx 30\%$.

Now let's investigate the strange particle yield ($dN/d\mathbf{y}$) as a function of N_{ch} . It seems natural that the yield will increase as a function of event multiplicity. In order to look for any increased strange over non-strange particle production we have divided the strange particle yield by the mean number of charged particles in each class.

It is interesting to observe that for both K_s^0 (figure 5.9) and Λ (5.10) the yield per charged particle is increasing, indicating increasing strange particle production over non-strange at higher multiplicities. There also seems to be a saturation of this value occurring at high $\langle N_{ch} \rangle$ values.

Figure 5.11 shows the $\bar{\Lambda}/\Lambda$ ratio vs multiplicity. The ratio appears to be constant except for the lowest multiplicity class.

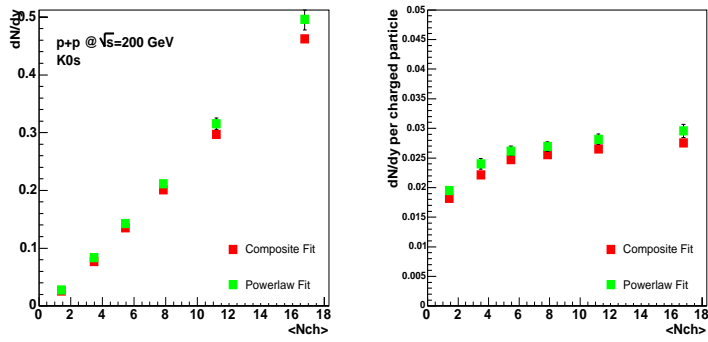


Figure 5.9: Left side is dN/dy of K_s^0 vs. event multiplicity, $\langle N_{ch} \rangle$. Results for the two best fit-functions are shown. Right side is dN/dy per charged track vs. $\langle N_{ch} \rangle$.

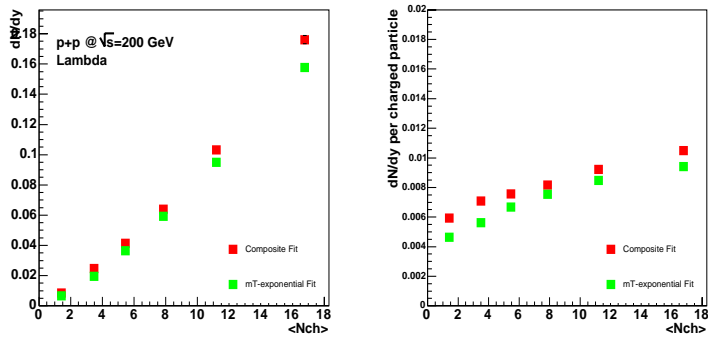


Figure 5.10: Left side dN/dy of Λ vs. event multiplicity, $\langle N_{ch} \rangle$. Results for the two best fit-functions are shown. Right side is dN/dy per charged track vs. $\langle N_{ch} \rangle$.

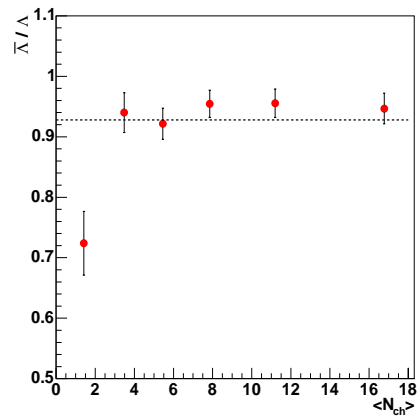


Figure 5.11: Ratio of $\bar{\Lambda}/\Lambda$ vs event multiplicity. Dashed line indicates minimum bias value of ratio.

5.2.2 R_{pp} vs. Event Multiplicity

Another way of presenting the particle spectra as a function of event multiplicity is shown in figure 5.12. By dividing the spectra for each multiplicity class by the min-bias p_T -spectra and scaling this ratio by the mean multiplicity of each class, the incremental shape changes are apparent as a function of p_T . This scaling is applied in order to normalize the ratio R_{pp} to ≈ 1 at low p_T for all multiplicities.

$$R_{pp}(p_T) = \frac{\langle N_{ch}(minbias) \rangle dN/dp_T(mult, p_T)}{\langle N_{ch}(mult) \rangle dN/dp_T(minbias, p_T)} \quad (5.8)$$

Equation 5.8 defines the ratio R_{pp} we will use in this section. It is clearly seen that for both K_s^0 and Λ the most dramatic changes in the spectra are seen at high p_T when going from low to high multiplicity events.

In figure 5.12 the low p_T region, i.e. < 1 GeV/c, is only slightly changed, whereas the high p_T region, > 3 GeV/c, is depleted by a factor of 10 in the low multiplicity sample and enhanced by a factor of 2-3 in the highest multiplicity sample. Therefore clearly the high-multiplicity events contribute strongly to the high p_T region.

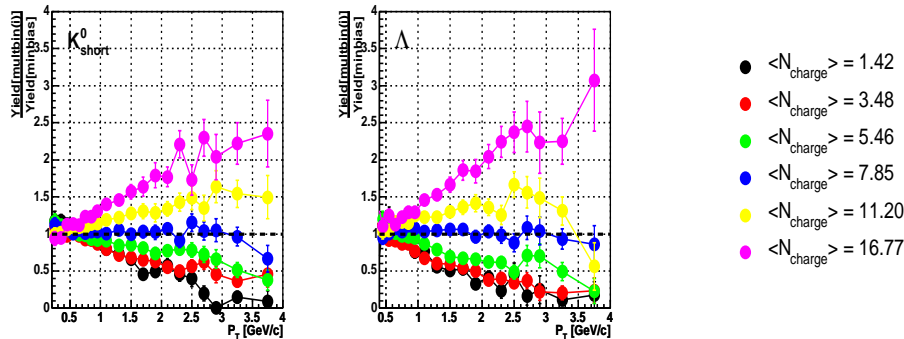


Figure 5.12: R_{pp} ratio for K_s^0 (left) and Λ as defined in equation 5.8 above.

Figure 5.13 shows the mixed ratio of $\frac{\Lambda}{K_s^0}$ vs. p_T and multiplicity. This ratio clearly shows a baryon over meson enhancement at intermediate p_T and has been frequently used to constrain certain hadronization models in Au+Au collisions using coalescence and recombination [93, 94, 95]. The ratio seems to be sensitive to the event multiplicity and saturates at a lower level for the low multiplicity class.

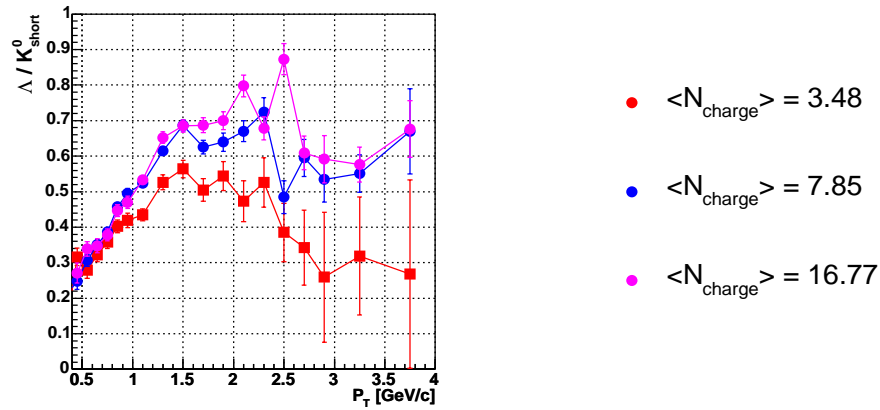


Figure 5.13: Ratio of Λ / K_s^0 vs p_T for three different event multiplicity classes. Lines connect the datapoints and are to guide the eye only.

Chapter 6

Exotic Searches

The search for **new** particles has always been a particular challenge for high energy physicists. The standard model classifies hadrons into mesons (2 quarks) and baryons (3 quarks) and up to now no bound states with more than 3 quarks have been observed. According to QCD there could be states formed out of more than 3 quarks, and theorists have predicted di-baryons (6 quarks) [104, 103] and pentaquarks (5 quarks) [110].

In 2003 the LEP5 collaboration made the first observation of a pentaquark state, named θ^+ , in a photo-production reaction at Spring-8 with a significance of 4.6σ [97]. This state had been predicted in 1997 by Diakonov et al. [110]. Shortly thereafter a number of other experiments confirmed the observation [112].

However, there have since been a number of non-observations of the θ^+ and other pentaquarks which have prevented the discovery of pentaquarks to be accepted by the wider community.

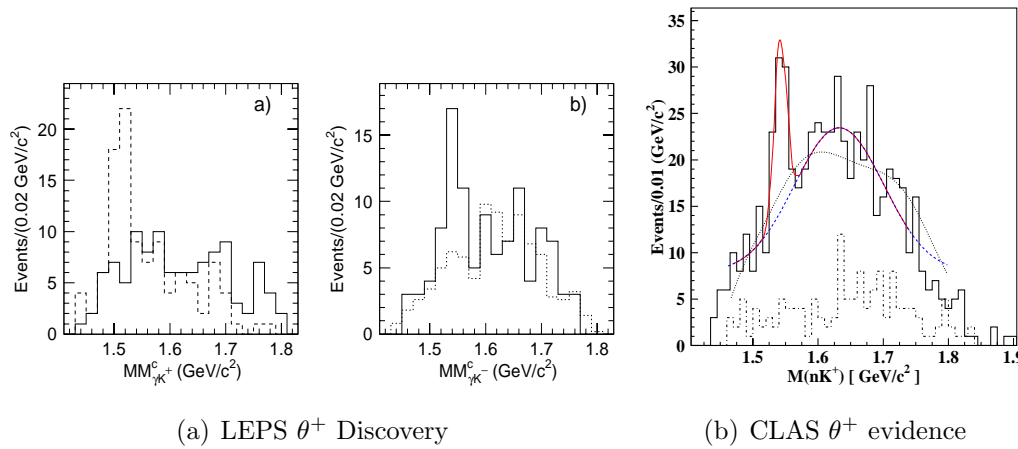


Figure 6.1: First observations of $\theta^+ \rightarrow K^+ + n$ by LEPS collaboration [97] and CLAS collaboration [99].

6.1 Experimental pentaquark evidence

6.2 Theory

We briefly review two theoretical models, the Chiral Soliton Model and the Diquark Model, that have tried to describe the pentaquark states and their masses. We don't expand to further models, e.g. Karliner-Lipkin, Lattice QCD results and others, due to the limited scope.

6.2.1 Chiral Soliton Model

Using the Chiral Soliton (CS) Model Praszalowicz in 1987 predicted that the $Y=2$ isosinglet member of the spin $\frac{1}{2}$ flavor anti-decuplet would lie near to 1540 MeV [109]. More precisely in 1997 Diakonov, Petrov and Polyakov predicted the θ^+ penta-quark (which they name Z^+) including an estimated width of 15 MeV in good agreement with experimental evidence [110]. This model was based on the Skyrme Model of baryons [107]. The CS model

predicts that the θ^+ has positive parity and a mass of 1530 MeV calculated through the predicted mass splitting of ≈ 180 MeV between the anti-decuplet members. In particular they assume that the non-strange member of the anti-decuplet can be identified with the known nuclear resonance $N(1710, \frac{1}{2}^+)$ [96] and all other masses are derived in consequence. More importantly, from an experimental point of view, Diakonov et al. also predict branching ratios and width of the exotic baryon candidates.

6.2.2 The Jaffe-Wilzcek Diquark model

The authors of this model assume the θ^+ to be an iso-singlet at the top of a flavor anti-decuplet as seen in figure 6.2 [106]. They further propose that the θ^+ ($udud\bar{s}$) consists of two highly correlated spin zero ud -diquarks and an anti-quark. This interpretation has some desirable features and makes predictions that distinguish it from the uncorrelated quark model and the chiral soliton model.

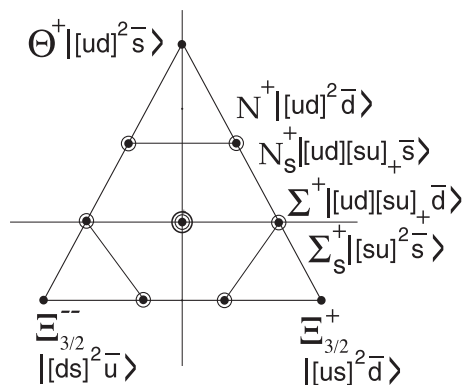


Figure 6.2: Flavor Anti-decuplet in the Jaffe-Wilzcek diquark model. Taken from [106]

In particular, the lowest lying state in the JW model is the N^+ at ≈ 1440

MeV whereas in the CS model it is the θ^+ . Moreover, in the JW model the Ξ^- pentaquark states lie close to the N_s and are much lighter than in the CS model. The authors consider the prediction of the light charge exotic Ξ^- 's as one of the distinctive signatures of their model. Indeed there has been experimental evidence for the Ξ^- found by the NA49 collaboration at ≈ 100 MeV above the predicted mass, but this result has not been confirmed and is still very controversial.

6.3 Analysis

Two datasets were analyzed for this exotic particle search, $p + p$ at $\sqrt{s} = 200$ GeV and $d + Au$ at $\sqrt{s} = 200$ GeV collisions. The first, $p + p$, yielded a 'hint' of a signal, which then triggered the analysis of the $d + Au$ sample, that has 5 times more events. Table 6.1 shows the statistics available in each set.

Cut	$p + p$	$d + Au$
recorded	14'729'936	9'979'656
Found Prim Vtx	12'698'221	8'603'152
Found Prim Vtx and $PV(z) < 100cm$ (normalisation)	10'853'180	7'260'684
prefiltered: $nK0 > 0, nP > 0$	208'649	1'130'403
prefiltered: $PV(z) < 100cm$	178'257	1'004'002

Table 6.1: Summary of event selection-cuts

Following the idea set forth by the CLAS collaboration [100] and later investigated by Karliner et al. and Azimov et al. we have focussed on analyzing a specific production channel [101, 102]. According to above references

the θ^+ can be produced via the decay of a N^* neutral resonance as shown in the Feynman diagram 6.3.

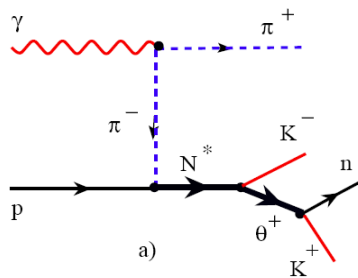


Figure 6.3: Possible θ^+ production channels via N^* (2400) resonance. Taken from [100]

This K^- may come from the N^* decay but even independent of the N^* existence it forces strangeness conservation in the event within the measured acceptance. The θ^+ is believed to decay in 2 different modes:

$$\theta^+ \rightarrow K^+ + n \quad (6.1)$$

$$\theta^+ \rightarrow K_s^0 + p \quad (6.2)$$

Out of the 14 experimental observations, 9 were in the charged kaon plus neutron channel and 5 in the K_s^0 plus proton channel. Since STAR does not have adequate neutron ID at mid-rapidity we measure the K_s^0 plus proton decay.

6.3.1 Pre-filtering of events

In a first stage of data reduction the events were analyzed and pre-filtered according to the number of θ^+ daughter candidates. To be retained the events

had to contain at least one loosely identified K_s^0 candidate and one proton. Table 6.2 and 6.3 summarize the pre-filtering cuts. This process dramatically reduces the file-size and the time to run the code. The negatively charged kaons are also stored in order to create the N^* invariant mass.

Cut	Value
V0 decay length (radial)	$> 3.0cm$
DCA of V0 to PrimVtx	$< 2.0cm$
DCA between V0-daughters	$< 0.8cm$
K_s^0 invariant mass	$0.45 < M_{inv} < 0.55$
N(hits) daughters	> 14
$N(\sigma)$ dE/dx	$< 3\sigma$

Table 6.2: Prefilter cuts for K_s^0

Track-Cuts	proton value	kaon value
Total momentum p	$< 1.5 \text{ GeV}/c$	$< 1.0 \text{ GeV}/c$
N(hits) daughters	> 14	> 14
Proton $N(\sigma)$ dE/dx	$< 3\sigma$	n.a.
Kaon $N(\sigma)$ dE/dx	$> 3\sigma$	$< 3\sigma$

Table 6.3: Prefilter cuts for protons and charged kaons

6.3.2 Reconstructing θ^+

Once the pre-filtering has been done and the actual mixing of daughter particles begins. A separate code runs three loops for each daughter of the N^* resonance. First all the K_s^0 and protons in an event are mixed, then the k^- are added to form the N^* invariant mass according to the decay:

$$\begin{aligned}
 N^* &\rightarrow \theta^+ + K^- \\
 &\hookrightarrow K_s^0 + p
 \end{aligned}
 \tag{6.3}$$

The cut-distribution for K_s^0 and proton variables after pre-filtering and after final cuts are seen in figure 6.4 - 6.6. The cut selections were guided by Monte-Carlo studies as well as from experience gained in the V^0 studies.

K_s^0 -Cuts	$p + p$ value	$d + Au$ value
V0 decay length	$> 3.5cm$	$> 5.0cm$
DCA of V0 to PrimVtx	$< 0.8cm$	$< 0.6cm$
DCA between pion daughters	$< 0.8cm$	$< 0.8cm$
K_s^0 invariant mass	$0.475 < M_{inv} < 0.515$	$0.475 < M_{inv} < 0.515$
pion daughter momentum	$< 2 \text{ GeV}/c$	$< 0.7 \text{ GeV}/c$
N(hits) daughters	> 14	> 14
$N(\sigma) \text{ dE}/dx$	$< 3\sigma$	$> 2\sigma$

Table 6.4: Final cuts for K_s^0

Track-Cuts	proton value		kaon value	
	$p + p$	$d + Au$	$p + p$	$d + Au$
Total momentum p	$< 1.2 \text{ GeV}/c$	$< 0.9 \text{ GeV}/c$	$< 1.2 \text{ GeV}/c$	$< 0.7 \text{ GeV}/c$
Track DCA to PV	$< 0.4 \text{ cm}$	$< 0.2 \text{ cm}$	$< 0.5 \text{ cm}$	$< 0.5 \text{ cm}$
N(hits) daughters	$> 14, > 55\%$	$> 14, > 55\%$	$> 14, > 55\%$	$> 24, > 55\%$
Proton $N(\sigma) \text{ dE}/\text{dx}$	$< 2\sigma$	$< 1\sigma$	n.a.	n.a.
Kaon $N(\sigma) \text{ dE}/\text{dx}$	$> 3\sigma$	$> 3\sigma$	$< 3\sigma$	$< 2.5\sigma$

Table 6.5: Final cuts for protons and charged kaons

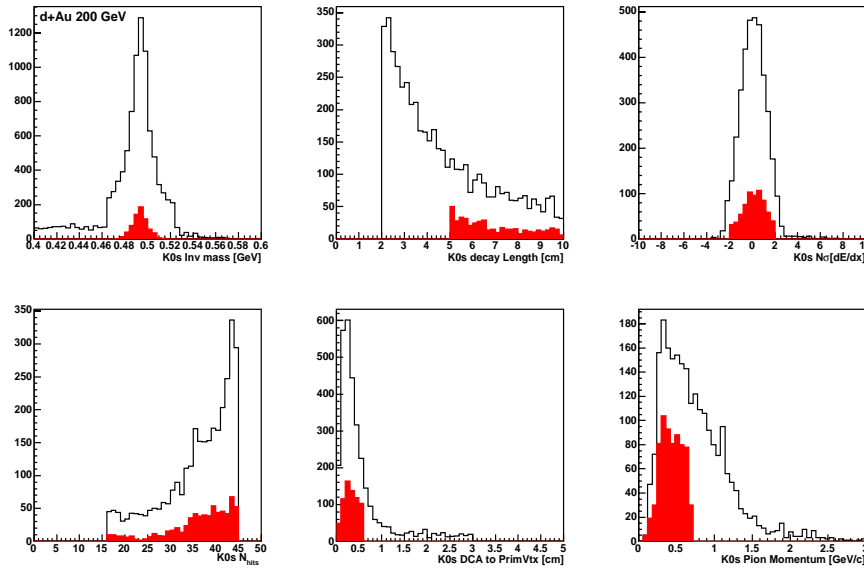


Figure 6.4: K_s^0 cut-distribution before (black) and after (red) cuts $d + Au$ collisions. a) invariant mass, b) decay length, c) $n\sigma \text{ dE}/\text{dx}$, d) daughter n_{hits} , e) Parent DCA to PV, f) pion daughter momenta

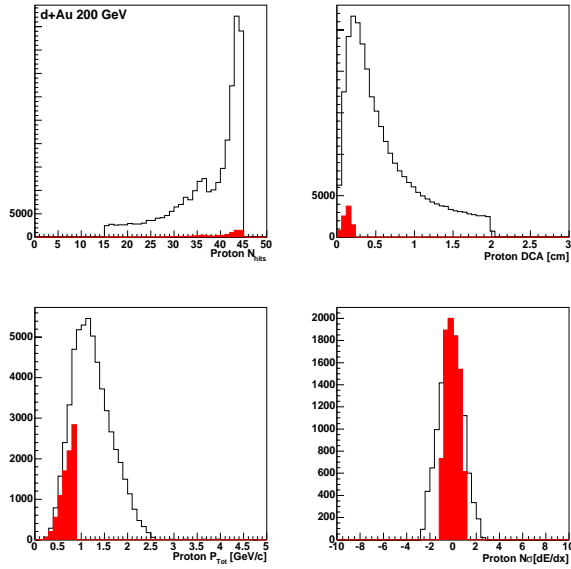


Figure 6.5: Proton cut-distribution before (black) and after (red) cuts $d+Au$ collisions. a) Track n_{hits} , b) Track DCA to PV, c) total momentum, d) $n\sigma$ dE/dx

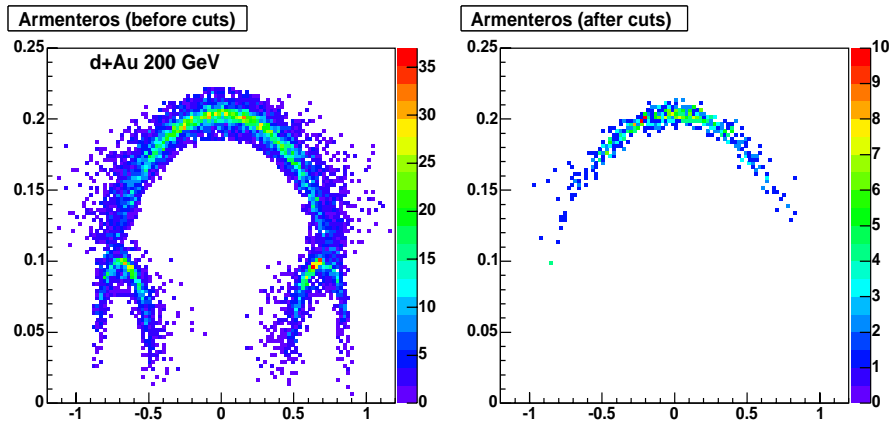


Figure 6.6: Armenteros-Podolanski plot for K_s^0 candidates before (left) and after cuts(right)

6.3.3 θ^+ background method

The background description of the θ^+ was obtained by the rotating particle method. To do this the momentum vector of the proton daughter is rotated around the z-axis by an angle β as seen in figure 6.7, thereby breaking the correlation of the decay. However since the total momenta remain the same the shape of the background is conserved.

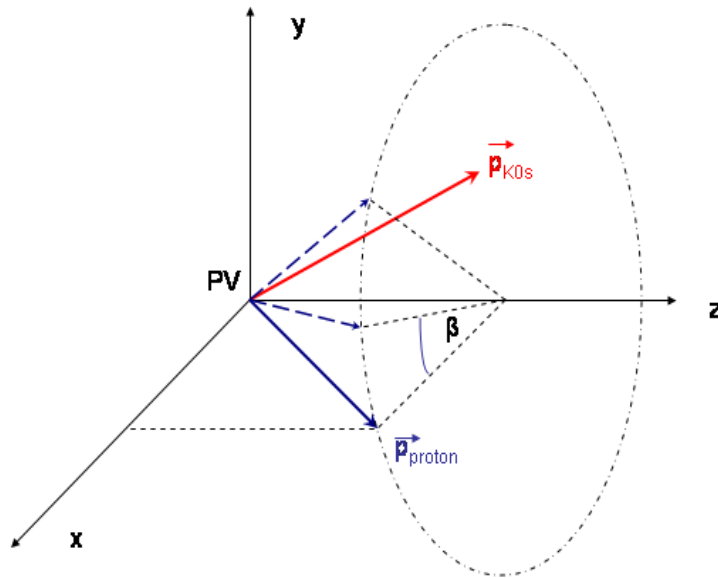


Figure 6.7: Sketch of rotating daughter background method. The momentum of the proton is rotated around the z-axis by an angle β and the θ^+ invariant mass is computed with the original K_s^0 momentum and the rotated proton momentum.

6.3.4 θ^+ Monte-Carlo simulation

Monte-Carlo simulations with the embedding technique (described in chapter 4.3.2) were performed θ^+ decay in $p + p$ and $d + Au$ collisions.

Since the simulation requests for $p + p$ and $d + Au$ were submitted at different times, thus at different stages of the search, the parameters were adapted differently. Table 6.6 shows the input parameter for the embedding studies in $p + p$ and $d + Au$.

System	$p + p$	$d + Au$
MC θ^+ (1 θ^+ per event)	20'000	100'000
θ^+ mass	1540 MeV	1550 MeV
θ^+ width	9 MeV	0 MeV
θ^+ p_T -distribution (inv. slope)	250 MeV	450 MeV
θ^+ rapidity distribution	$ y < 1.5$ (flat)	

Table 6.6: θ^+ Monte-Carlo simulation requests

Momentum Cut optimization

Monte-Carlo simulation can be used to optimize the cut-values by clearly distinguishing signal and background. We analyzed the distributions of the most important cut variables with the MC simulation, which enables us to choose our cut values.

In figure 6.8 we have compared the proton daughter momentum distribution from simulation and real data. Up to 1 GeV/c we have good proton identification via dE/dx . Above 1 GeV/c the contamination through pion tracks becomes apparent and dominates the distribution from real data. The

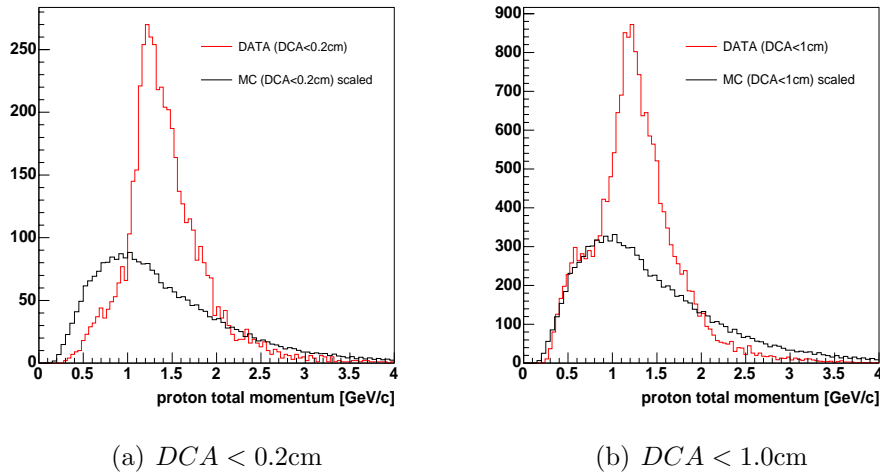


Figure 6.8: Comparison of proton-daughter momentum from real data and simulated θ^+ decay

ideal cut-value is set at 0.9 GeV/c in $d + Au$ collisions, in $p + p$ collisions we have opened it up to 1.2 GeV/c due to the poor statistics.

Cut efficiency estimation

In order to obtain a cross-section estimation we need to calculate the efficiency and acceptance of our offline cuts. This is done using the embedding technique explained previously.

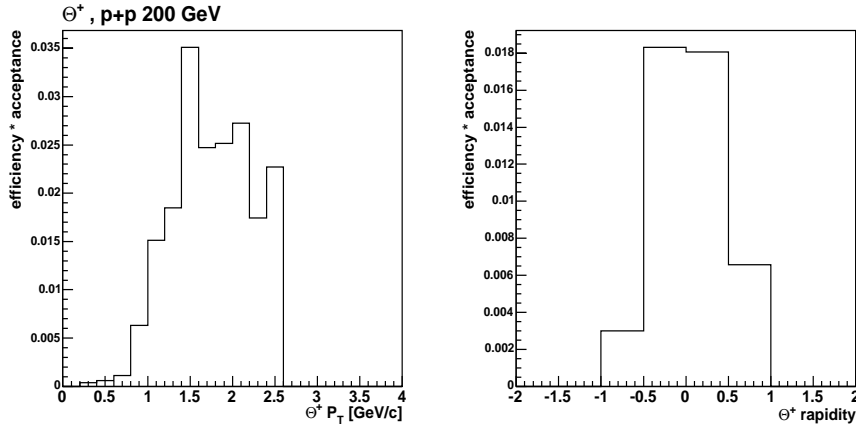


Figure 6.9: θ^+ reconstruction efficiency from MC study in $p + p$ collisions. Left: efficiency vs transverse momentum, right: efficiency vs rapidity.

The resulting total correction factor, i.e. efficiency * acceptance is shown in figure 6.9 and 6.10. From these plots we need to calculate the average value over the chosen phase space in y - p_T . The resulting correction factors which enter into the yield calculation for $p + p$ and $d + Au$ cuts are 1.2% respectively 0.2%.

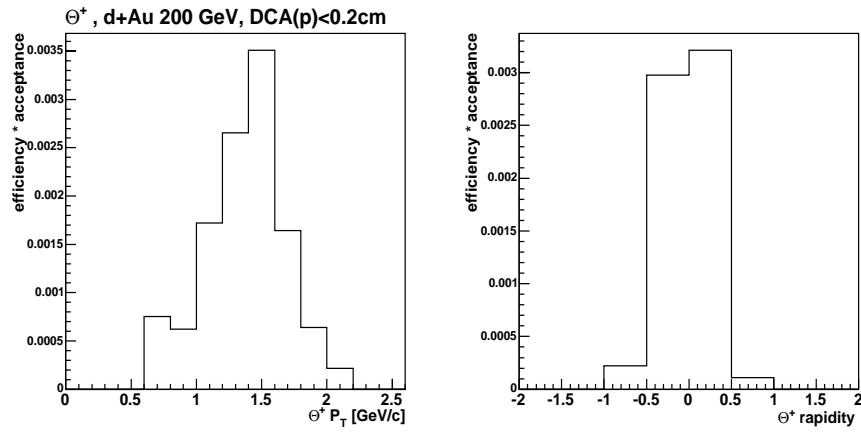


Figure 6.10: θ^+ reconstruction efficiency from MC study in $d + Au$ collisions. Left: efficiency vs transverse momentum, right: efficiency vs rapidity.

Determination of experimental resolution

The Monte-Carlo study was also useful to determine the experimental resolution for the decay $\theta^+ (1550) \rightarrow p+K_s^0$. In $p + p$ collisions our embedded signal had a width of 9.07 MeV and our reconstructed signal had a width of 10.91 ± 1.49 MeV as can be seen in figure 6.11. We can estimate the experimental broadening by quadratic sum to be ≈ 6 MeV.

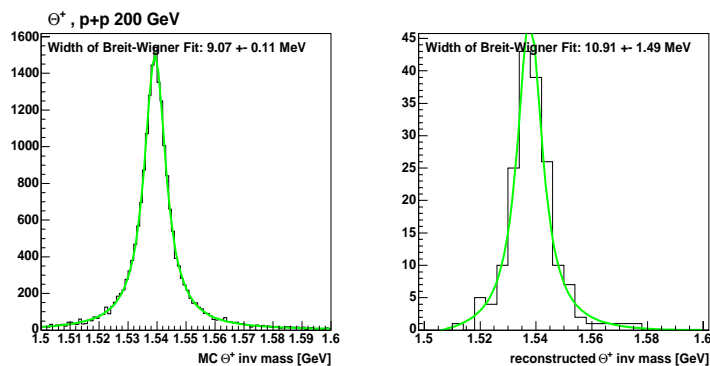


Figure 6.11: θ^+ invariant mass in $p + p$ simulation. Left: Simulation input, right: reconstructed peak showing experimental resolution of ≈ 6 MeV

In $d + Au$ collisions we simulated a signal with zero width. The reconstructed output as seen in figure 6.12 returned a peak of 4.96 ± 0.27 MeV width, which corresponds to our experimental resolution.

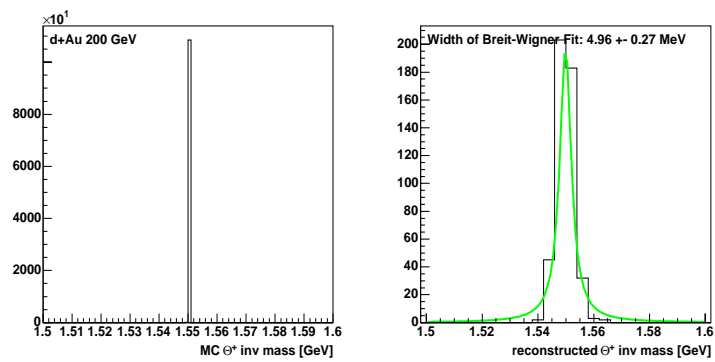


Figure 6.12: θ^+ invariant mass in $d + Au$ simulation. Left: Simulation input, right: reconstructed peak showing experimental resolution of ≈ 5 MeV

6.3.5 Cross-checks

Different cross-checks have been performed in order to exclude some common reasons for spurious signals and statistical fluctuations. The following checks have been done:

1. One potential hazard is a K^-/π^- mis-identification which could lead to a false reconstruction of the N^* resonance. In particular we checked that no θ^+ peak was visible when cutting on the invariant mass of this “false N^* ”.
2. According to Dzierba et al [98] some experiments measuring inclusive signals were victims to spurious signal peaks due to p/π^+ misidentification of a Λ decay. The Λ decay is then reconstructed as K_s^0 and mixed with the proton daughter resulting in a sharp peak around the expected θ^+ mass. We have verified that there are no entries in the Λ invariant mass region that could be created by such a mis-identification.

6.4 Results and Discussion

In figure 6.13 the invariant mass after all cuts is shown for $p + p$ collisions. The significance for the center row (requiring k^-) using the method, $sig = S/\sqrt{B} = 22.8/\sqrt{56}$, is only 3.04. The measured width is 4 ± 21 MeV consistent with our experimental resolution and thus a very narrow θ^+ peak.

The result from $d + Au$ collisions can be seen in figure 6.14. The significance in the center row is: $sig = S/\sqrt{B} = 23.9/\sqrt{19} = 5.48$. For the signal seen with the N^* mass requirement (bottom row) we do not have reliable background estimate. The observed width is 6 ± 2.7 MeV consistent with our experimental resolution.

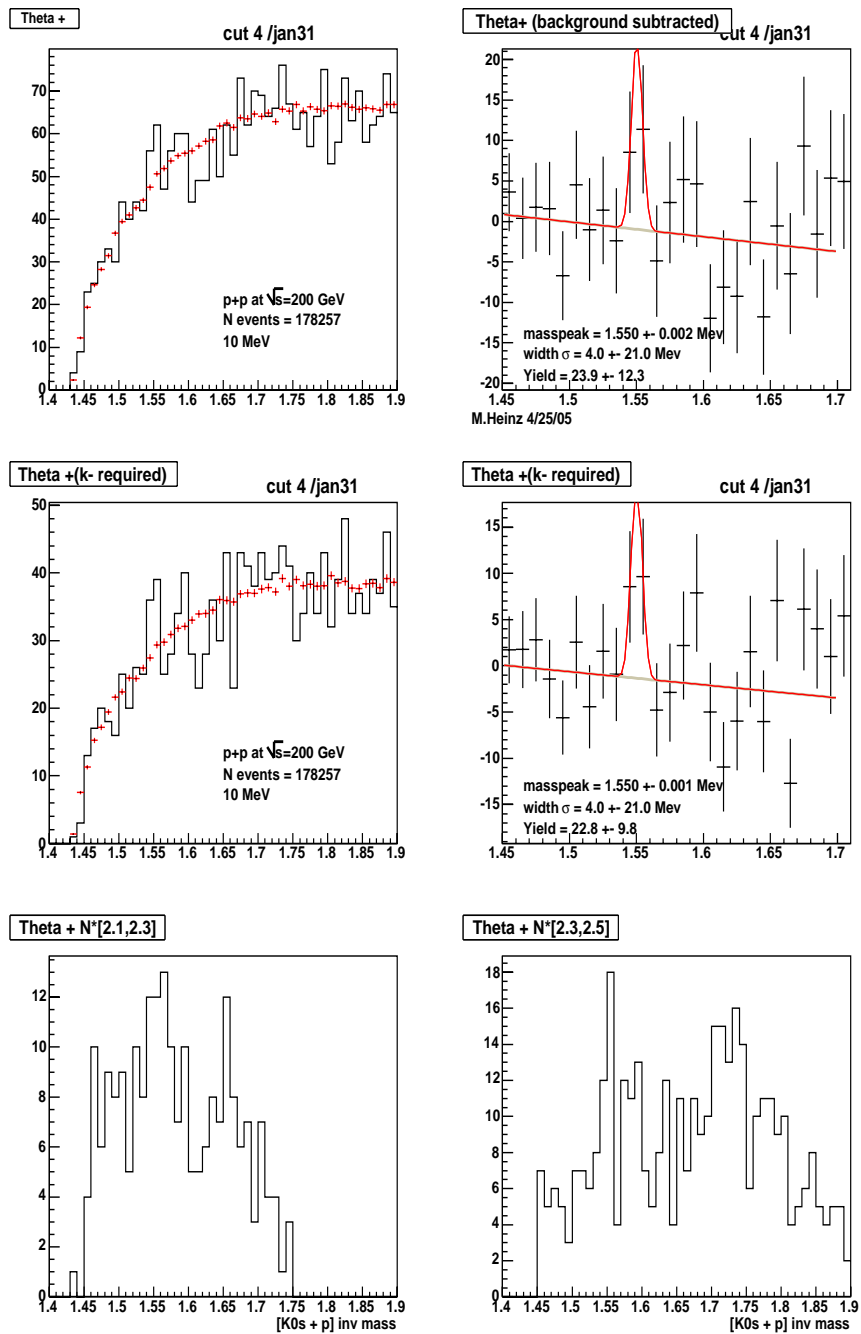


Figure 6.13: θ^+ invariant mass in $p + p$ collisions. Fit is gaussian plus linear background. Top row: Without strict k^- cut. Center row: k^- is required to pass the cuts. Bottom row: requirement on N^* invariant mass

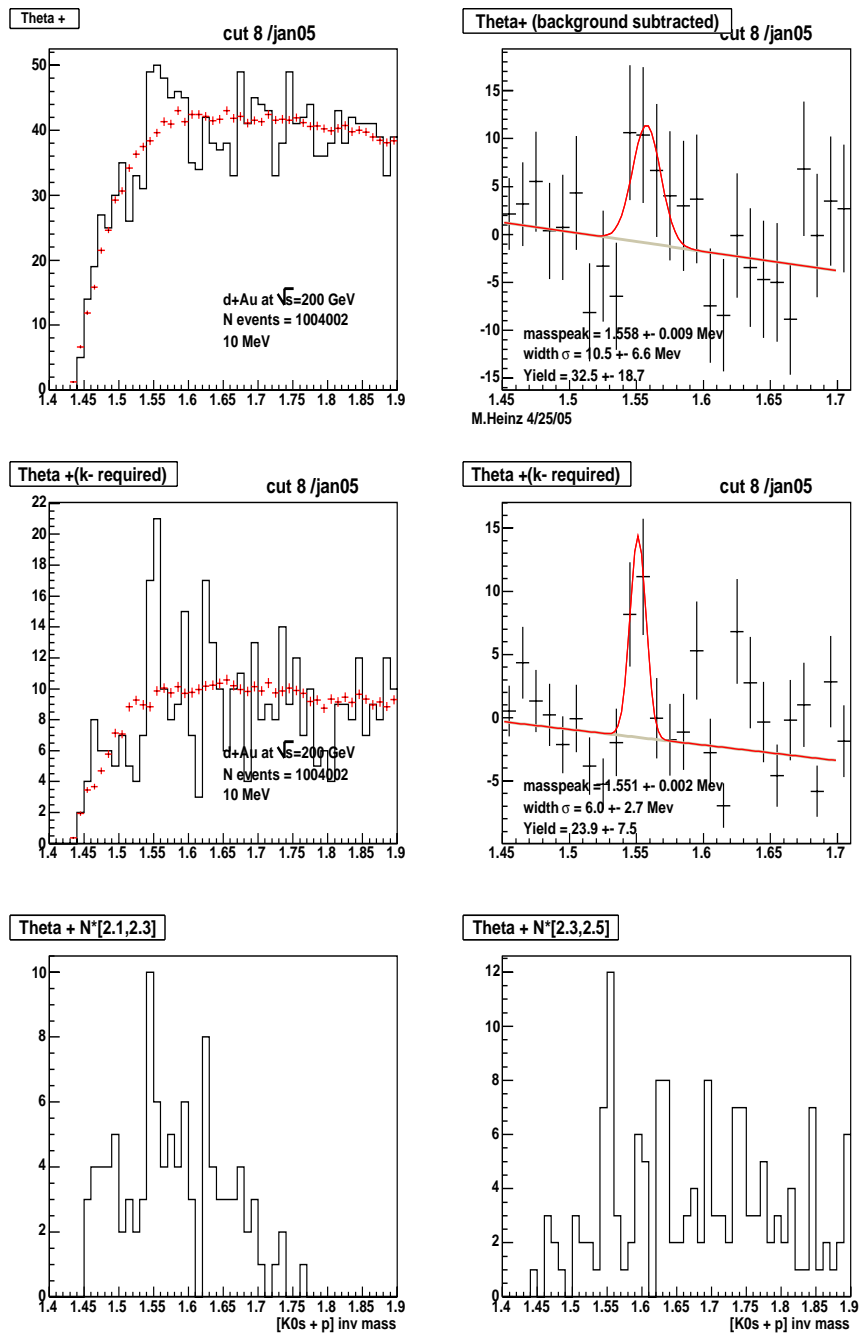


Figure 6.14: θ^+ invariant mass in $d+Au$ collisions. Fit is gaussian plus linear background. Top row: Without strict k^- cut. Center row: k^- is required to pass the cuts. Bottom row: requirement on N^* invariant mass

6.4.1 Cross-Section estimation

In order to make meaningful comparisons to theory and other experiments it is important to estimate a production cross-section of the observed 'signal'.

First, we need to assume a branching ratio of the observed channel, $\theta^+ \rightarrow K_s^0 + p$, to be 25%, due to an equal 50% splitting into the two decay modes, and an additional 50% due to the possible K_L^0 final state, which is not measured in STAR.

Second, we can now apply the acceptance and efficiency corrections computed with the MC simulation using our reconstruction cuts. We need to estimate a correction factor for the phase-space region in p_T and rapidity in which we measure our signal. These values are 1.2% and 0.2% for $p + p$ and $d + Au$ respectively with a statistical and systematical error of about 20%.

System	$p + p$	$d + Au$
Raw yield ($ y < 1$)	22.8 ± 9.8	23.9 ± 7.5
Raw yield per event	$1.97 \pm 0.85 \times 10^{-6}$	$3.14 \pm 0.93 \times 10^{-6}$
Efficiency in measured (y, p_T)	1.2%	0.2%
Eff. corrected yield/event	$1.64 \pm 0.70 \times 10^{-4}$	$1.57 \pm 0.46 \times 10^{-3}$
branching ratio (est.)	0.25	0.25
θ^+ yield $ y < 1.0$	$6.57 \pm 2.82 \times 10^{-4}$	$6.28 \pm 1.81 \times 10^{-3}$
θ^+ dN/dy	$3.28 \pm 1.41 \times 10^{-4}$	$3.14 \pm 0.91 \times 10^{-3}$
Ratio $\theta^+/\Lambda^*(1520)$	0.094 ± 0.060	0.21 ± 0.14
Ratio θ^+/Λ	0.0094 ± 0.005	0.018 ± 0.009

Table 6.7: θ^+ Cross-section estimation with respect to Λ and $\Lambda^*(1520)$ analysis [113, 114].

The Hera-B collaboration reported their negative results on θ^+ searches

in p+A collisions at $\sqrt{s}=47$ GeV [111]. They conclude that the upper limit for the ratios $\frac{\theta^+}{\Lambda}$ is 0.92% and for $\frac{\theta^+}{\Lambda^*(1520)}$ is 2.7% assuming a θ^+ mass of 1530 MeV. They also mention that these values may be 4 times higher if the θ^+ mass is 1540 MeV.

6.4.2 Conclusion

We have analyzed data from $p+p$ and $d+Au$ collisions at $\sqrt{s}=200$ GeV in the STAR experiment. We have selected our cuts in favor of a proposed θ^+ production mechanism via an $N^*(2400)$ resonance. We see a peak structure in the $K_s^0 + p$ invariant mass around 1550 MeV with a width of 6 MeV and 4 MeV in $d+Au$ collision respectively $p+p$ collisions. The statistical significance, S/\sqrt{B} , is ≈ 3.0 for $p+p$ and ≈ 5.5 for $d+Au$ collisions.

Using Monte-Carlo simulation we have estimated the reconstruction efficiency and obtained relative θ^+ cross-sections with respect to $\Lambda^*(1520)$ and Λ measured by STAR. The $\theta^+/\Lambda^*(1520)$ results are in agreement with being below the Upper Limit (UL) published by HERA-B experiment, while the θ^+/Λ results are below the upper limit as shown in table 6.8.

Experiment	STAR	HERA-B
CMS energy	200 GeV	42 GeV
collision	d+Au	p+A(A=C,Ti,W)
$\theta^+/\Lambda^*(1520)$	0.21 ± 0.14	< 0.11
θ^+/Λ	0.018 ± 0.009	< 0.037

Table 6.8: θ^+ Cross-section estimation by STAR compared to Upper Limits published by HERA-B [111].

In closing, let me emphasize, that this is still a preliminary, non-official

result of the STAR collaboration since it has not been independently verified. However further work is ongoing with more statistics to establish a more statistically significant result

Chapter 7

Discussion

7.1 Comparison to previous measurements

7.1.1 p_T -Spectra and yields

First we will compare our measurement of neutral strange particles to similar experiments at this energy . The closest comparison can be made to the $Spp\bar{S}$ (Super Proton-Antiproton Synchrotron) experiments of UA1-UA5 with the $\bar{p} + p$ beam [8, 6, 58]. Only UA5 published strange particle measurements at $\sqrt{s} = 200$ GeV, with others at $\sqrt{s} = 546$ GeV and 900 GeV whereas UA1 published high statistics strange particle measurements at $\sqrt{s} = 630$ GeV. In those days, the early 1980's, the experiments still had to 'manually' sort V^0 candidates and the statistics were poor, ie. the final Λ sample at $\sqrt{s} = 200$ GeV consisted of only 168 candidates [57]. As a comparison the STAR Λ sample consists of 58500 candidates.

Figure 7.1 shows the transverse momentum spectra from STAR and $Spp\bar{S}$ scaled by a factor obtained via PYTHIA simulation (see figure 7.2 accounting for the difference in rapidity coverage of the two experiments, UA5 measured

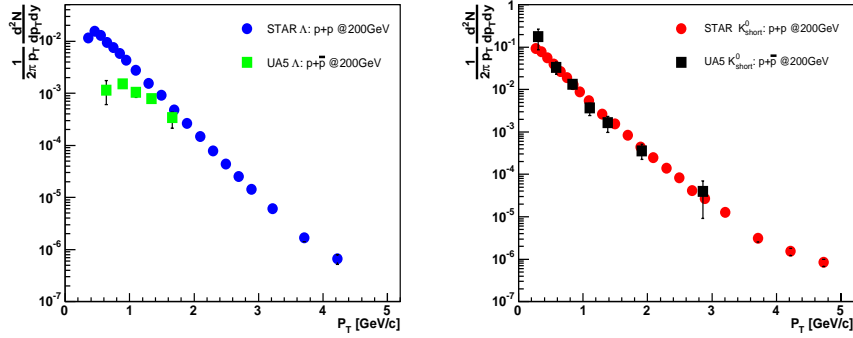


Figure 7.1: Comparison of inclusive p_T -spectra for K_s^0 (left) and Λ (right) for STAR vs CERN UA5 experiment [58, 57]

K_s^0 with $|y| < 3.5$ and Λ with $|y| < 2.0$. The K_s^0 spectra agree well whereas the Λ show a significant disagreement at $p_T < 1.5$ GeV/c. This may be due to the fact that for the Λ the difference in the rapidity interval of the measurement may affect the shape of the p_T distribution more.

The values of extrapolated dN/dy and $\langle p_T \rangle$ are tabulated in table 7.1. We have verified that the dependance of $\langle p_T \rangle$ on the different rapidity intervals between STAR and UA5 is small, i.e. 2-3 %. There is a good agreement with the previous measurements of K_s^0 and Λ in $\bar{p} + p$ collisions at UA5.

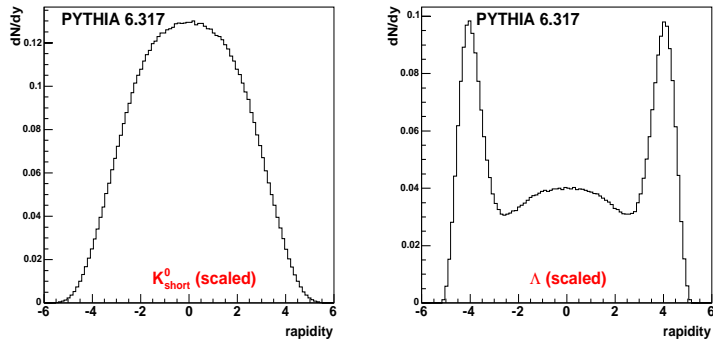


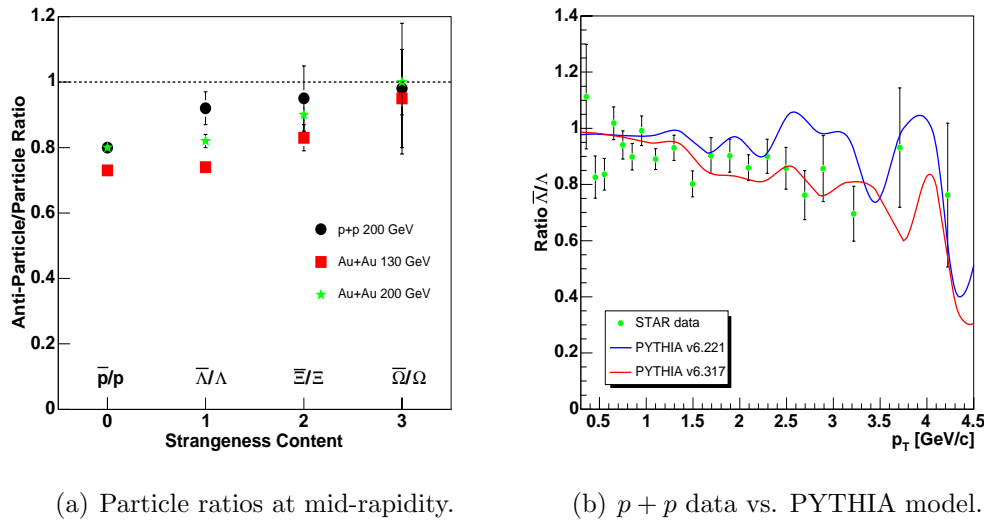
Figure 7.2: Rapidity distribution for K_s^0 (left) and Λ (right) from PYTHIA simulation of $p + p$ events.

Particle	STAR dN/dy $ y < 0.5$	UA5 dN/dy $ y < 3.5, y < 2.0$	UA5 dN/dy $ y < 0.5$	STAR $\langle p_T \rangle$ [GeV/c]	UA5 $\langle p_T \rangle$ [GeV/c]
K_s^0	0.136 ± 0.013	0.73 ± 0.11 [58]	0.15 ± 0.03	0.60 ± 0.04	$0.53 + 0.08, -0.06$
$\Lambda + \bar{\Lambda}$	0.083 ± 0.010	0.27 ± 0.07 [57]	0.08 ± 0.02	0.77 ± 0.06	$0.8 + 0.2, -0.14$

Table 7.1: A comparison of mid-rapidity yields and $\langle p_T \rangle$ for K_s^0 and Λ measured by STAR and UA5. STAR measurements include stat. and syst. errors. The UA5 measurements were made over a large rapidity interval and have been scaled down using the following factors obtained from PYTHIA simulation (see figure 7.2): $K_s^0 = 4.67 (|y| < 3.5)$, $\Lambda = 3.27 (|y| < 2.0)$

7.1.2 Particle ratios

The production of anti-particles happens via a different mechanism since they contain anti-quarks which are not present in the incoming nuclei and have to be produced in the collision. As the energy of the collision increases the net-baryon density at mid-rapidity, ie. the number of baryons minus the number of anti-baryons, decreases and tends to zero as shown by models and experiments [59, 20, 60]. In STAR we have measured baryon ratios with strangeness 0 through 3 at two different collision energies of $\sqrt{s} = 130$ GeV and 200 GeV as shown in the left panel of figure 7.3.



(a) Particle ratios at mid-rapidity.

(b) $p + p$ data vs. PYTHIA model.

Figure 7.3: Anti-particle to particle ratios.

It is interesting to notice that in both heavy ion and $p + p$ collisions these ratios tend to 1 with increasing strangeness. At $\sqrt{s} = 130$ GeV the net-baryon density is higher and therefore the values of these ratios are slightly lower.

On the right panel of figure 7.3 we show the $\bar{\Lambda}/\Lambda$ ratio vs. p_T up to 4.5 GeV/c in $p + p$ data. The ratio seems flat below $p_T = 2.5$ GeV/c but may

show signs of a downward slope above this value, although not significant within errors. This trend is supported by pQCD models such as PYTHIA and can be understood in the following way. At high p_T the Λ particle is produced by fragmentation from quarks and gluons, whereas $\bar{\Lambda}$ is mainly produced from fragmenting gluons. As we go higher in p_T we are probing high- x values where quark-jet production dominates over gluon-jets and thus $\bar{\Lambda}$ production becomes weak [69].

Also overlaid in this figure are the new most recent calculations from PYTHIA. It is interesting to observe that in the newer version of PYTHIA (6.317) the steepness of the 'falling slope' in the ratio seems to have increased over previous versions. We will discuss the PYTHIA comparisons more in detail later.

7.2 $\langle p_T \rangle$ Systematics

7.2.1 $\langle p_T \rangle$ vs N_{ch}

A special effort has been made in this thesis to analyze the p_T spectra of strange particles for different event multiplicity classes. The idea behind this is the following. According to pQCD in a hard p+p collision multiple mini-jets may be produced and their subsequent fragmentation will produce a larger charge particle multiplicity (N_{ch}) [42, 41, 71, 62]. At the same time strange particles are also produced from fragmenting mini-jets. Therefore, as the number and the 'hardness' of mini-jets increases the fraction of strange particles from fragmentation may increase and populate the high transverse momentum part of the spectrum. Thus by studying spectra as a function of N_{ch} we hope to study the effect of mini-jets on particle production compared to the production in "soft" $p + p$ collisions. The "soft" part of the

$p + p$ collisions, also known as "underlying event", consists of remnants of the incoming protons, i.e. particles that come from the breakup of the proton. These "beam remnants" are the reason why hadron-hadron collisions are more "messy", i.e. a lot of low- p_T background, than $e^+ + e^-$ collision. These phenomenologies are implemented in most pQCD models (PYTHIA, HIJING).

Only a few collider experiments have previously measured particle identified increase of $\langle p_T \rangle$ as a function of event multiplicity at similar energies. In figure 7.4 we compare our results to measurements in $\bar{p} + p$ collisions at SPS and Fermilab, both at higher \sqrt{s} .

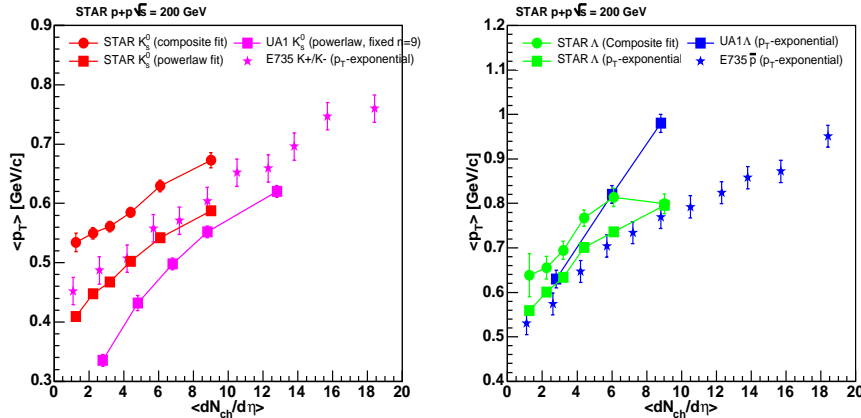


Figure 7.4: Comparison of inclusive $\langle p_T \rangle$ vs. N_{ch} for K_s^0 (left) and Λ (right) for STAR vs other experiments. p_T range of E735 was 0.3-1.5 GeV/c [61]. UA1 measurement extended to 6 GeV/c(K_s^0) and 7 GeV/c (Λ) [15]

UA1 measured $\langle p_T \rangle$ for K_s^0 , Λ and charged particles at $\sqrt{s} = 630$ GeV [15]. The parametrization used for extracting $\langle p_T \rangle$ was a powerlaw function with $n=8.9$ fixed for K_s^0 and an exponential function in p_T for Λ . Fermilab's E735

experiment measured charged kaons, anti-protons and pions at $\sqrt{s} = 1.8$ TeV [61].

On the left panel of figure 7.4 the comparison for kaons is shown. The $\langle p_T \rangle$ from STAR K_s^0 data has been extracted using the composite fit, described in detail in chapter 4, as well as a powerlaw fit with fixed \mathbf{n} to compare to UA1. The difference in $\langle p_T \rangle$ obtained from the two parameterizations illustrates the importance of the fit functions. The STAR $\langle p_T \rangle$ is consistent within systematical errors with the Fermilab measurement at much higher \sqrt{s} . The UA1 data however appears to be systematically lower. The expected ordering of $\langle p_T \rangle$ with \sqrt{s} is broken. It has to be noted that the powerlaw parametrization underestimates $\langle p_T \rangle$ in most cases since it does not account for the thermal “turnover” of the spectra at low p_T .

On the right panel of the same figure a comparison of Λ and anti-protons is shown. Since E735 did not publish a measurement of Λ vs. multiplicity the anti-proton data is brought into comparison being a baryon with comparable mass to the Λ . For UA1 we compare to Λ $\langle p_T \rangle$ obtained from 3 multiplicity classes at $\sqrt{s} = 630$ GeV. Again, the STAR data seem to agree better with the Fermilab data than the SPS data. Especially, the last data-point of UA1 seems very high.

In summary we have shown that the trends of $\langle p_T \rangle$ vs N_{ch} agrees qualitatively with previous measurements and establishes a new baseline at $\sqrt{s} = 200$ GeV. We have explored the systematics of using different fit parameterizations to obtain the $\langle p_T \rangle$ value.

Another interesting comparison is to look at $\langle p_T \rangle$ vs N_{ch} for different particle species at the same collision energy. Figure 7.5 shows $\langle p_T \rangle$ measurements of five different particles species in $p + p$ collisions by STAR [86, 88, 89]. The mass ordering of the mean values is apparent, but also the increase in the

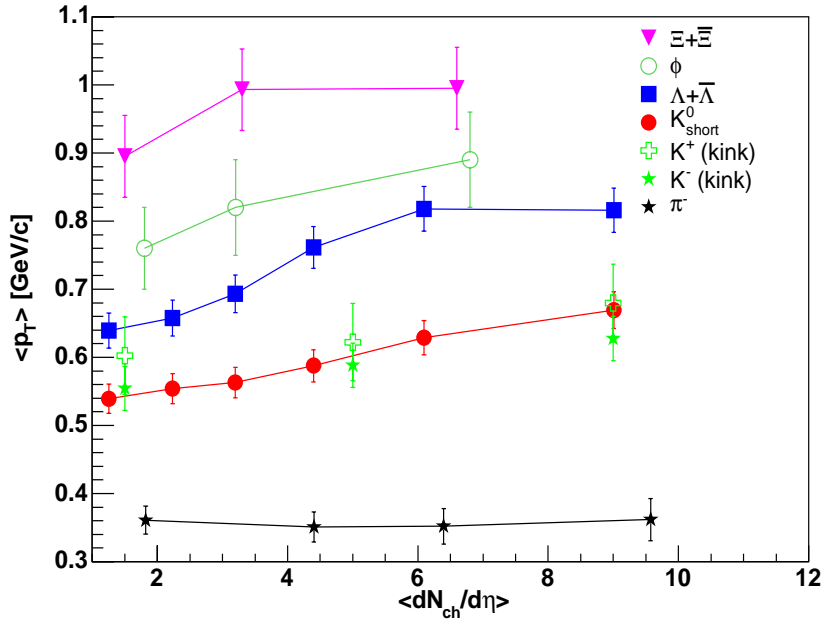


Figure 7.5: $\langle p_T \rangle$ vs $\langle dN_{ch}/d\eta \rangle$ for different particles measured by STAR in $p + p$ collisions at $\sqrt{s} = 200$ GeV.

strength of the dependence with charged multiplicity. This seems to indicate that indeed heavier strange particles have more contributions from mini-jets and therefore there $\langle p_T \rangle$ is more sensitive to N_{ch} .

The conclusion has been made by previous authors and been attributed to the fragmentation of multiple mini-jets [70]. In another reference by McLerran *et al.* conjectures that the broadening of intrinsic gluon momentum could cause such an effect [64].

7.2.2 $\langle p_T \rangle$ vs. particle mass

More evidence for strange particle production via mini-jets may be found in observing the dependency between $\langle p_T \rangle$ and particle mass.

In heavy ion collisions a strong correlation between the inverse slope T (indicative of $\langle p_T \rangle$) and particle mass was observed [66]. This effect has been attributed by different authors to the mass-dependant effects of radial flow, i.e. the collective expansion of the particles. Radial flow is a consequence of the initial energy density of the system or the "explosive" energy of the collision. The collective expansion of the particles in a fireball implies that all particles have the same velocity and therefore the momenta of heavier particles will be influenced more strongly. It also seems natural that radial flow is stronger in heavier systems, i.e. higher atomic mass, as well as in more central collisions [67].

In the past, measurements in low energy $p + p$ collisions of inverse slope T showed no dependance of particle mass, and this generally believed to be proof, that the system is too "small" for collective behavior and radial flow to develop [68].

As shown in figure 7.6 STAR has measured a multitude of particle species in Au+Au and p+p collisions. On the y-axis we use $\langle p_T \rangle$ rather than inverse slope T since it is independent of the assumption of exponential spectra shapes. As in previous measurements we observe a strong dependence of $\langle p_T \rangle$ vs mass in heavy ion collisions, indicative of radial flow.

In contrast to previous experiments we now also measure a dependence of $\langle p_T \rangle$ vs. particle mass in $p+p$ collisions. We still believe that the system size is too small for radial flow to develop and therefore need alternative explanations. In pQCD models the dependance of $\langle p_T \rangle$ on particle mass can be explained by mini-jet production and a stronger contribution to higher mass particles

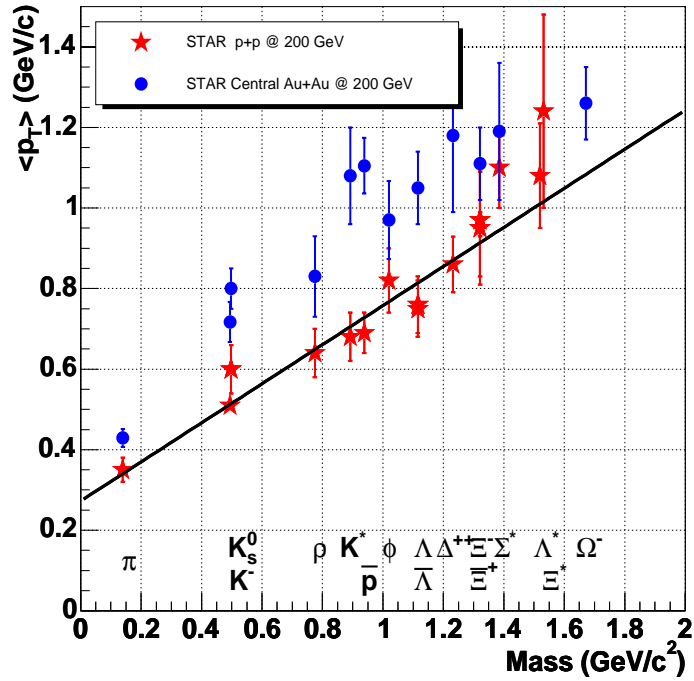


Figure 7.6: $\langle p_T \rangle$ vs particle mass in central Au+Au and $p + p$ collisions measured by STAR

is expected to be seen [70]. In a technically different approach Dumitru *et al.* analyzed the inverse slope parameters vs particle mass from PYTHIA simulation and also concluded that the increase was due to multiple mini-jet production and could not be explained by hydro-dynamical models [65].

7.3 Comparison to model predictions

In this section we will compare our data to several phenomenological models on the market for hadronic collisions: PYTHIA, NLO and EPOS. The goal being to establish how well the implemented theoretical processes are capable of reproducing the $p + p$ data. Furthermore, we hope to get an understanding of which parameters in these models are particularly sensitive to our measurements.

7.3.1 PYTHIA 6.221

Comparing to a widely used Monte-Carlo Event Generator such as PYTHIA can be a useful exercise and give us insight about the processes that should be implemented and those that may be missing. Of course any model comparison should be interpreted with care since most models can be tuned via their input parameters and their meaningful physical ranges are often unknown.

We used PYTHIA v6.221, as available from the authors website ¹, and first looked at the results from the default parameter set. PYTHIA, although a LO-calculation, is a highly complex model with a large number of parameters covering both the perturbative and non-perturbative aspects of a collision.

Since the default parameters did not yield satisfactory agreement with our data, see later, we started by tuning two parameters, the LO K-Factor and the parton intrinsic k_T . The K-Factor is a phenomenological “fudge” factor allowing for higher order parton processes to be approximated by a singly multiplicative factor as shown in equation 2.4. It is generally dependant on the outgoing quark flavor and collision energy [79]. Intrinsic parton k_T is

¹<http://www.thep.lu.se/~torbjorn/Pythia.html>

assumed to be caused by initial state (before the hard scattering) or final state (after the hard scattering) gluon radiation. This broadening of the parton momentum can cause effects in the final state hadrons thereby modifying their momentum spectra.

A list of the parameters that were tuned in this thesis are shown in table 7.2.

Parameter description	K-Factor	Intrinsic k_T
Program variable	MSTP(33)	MSTP(91)=1
Default value	1.0	$\langle k_T^2 \rangle = 1 \text{ GeV}$
Tune A (K-factor)	2.0	1.0
Tune B (K-factor)	3.0	1.0
Tune C (k_T)	1.0	2.0 GeV
Tune D (k_T)	1.0	4.0 GeV

Table 7.2: A summary of tuned PYTHIA parameters.

Simulating STAR trigger

To save computing power the output from PYTHIA was not reconstructed through the full STAR geometry and detectors. Rather we simulated the STAR p+p event trigger (BBC), by requiring that a simulated event has to contain at least one charged track with $3.3 < |\eta| < 5.0$ in forward and backward direction, ie. within the STAR BBC acceptance. This condition assumes 100% BBC efficiency but yields sufficiently precise trigger condition to compare to real data.

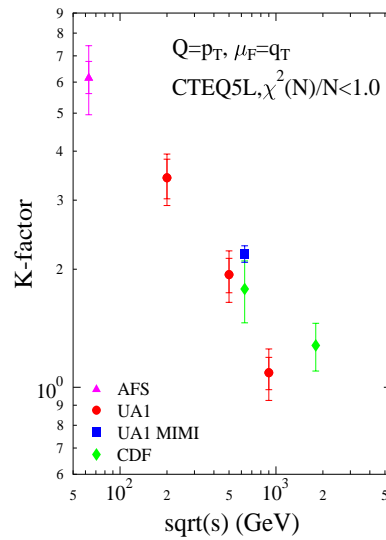


Figure 7.7: Compilation by Eskola et al. of K-Factors for charged hadrons spectra computed at different \sqrt{s} using KKP fragmentation functions. The inner error bars are the statistical errors calculated, the outer reflect the systematic errors reported by the experiment. Taken from [79]

Charged event multiplicity

The first observable I compared to was the mid-rapidity charged multiplicity (N_{ch}) in events that were triggered. This distribution is highly dominated by low- p_T particles from non-perturbative processes, where we do not expect good agreement with data. Nevertheless PYTHIA includes an extrapolation into the semi-hard QCD processes responsible for particle production in this momentum region.

Clearly only tune B, ie. K-factor=3, produces a similar number of high multiplicity events as compared to our data. All other parameter settings show a large discrepancy of events with multiplicity > 10 compared to our data.

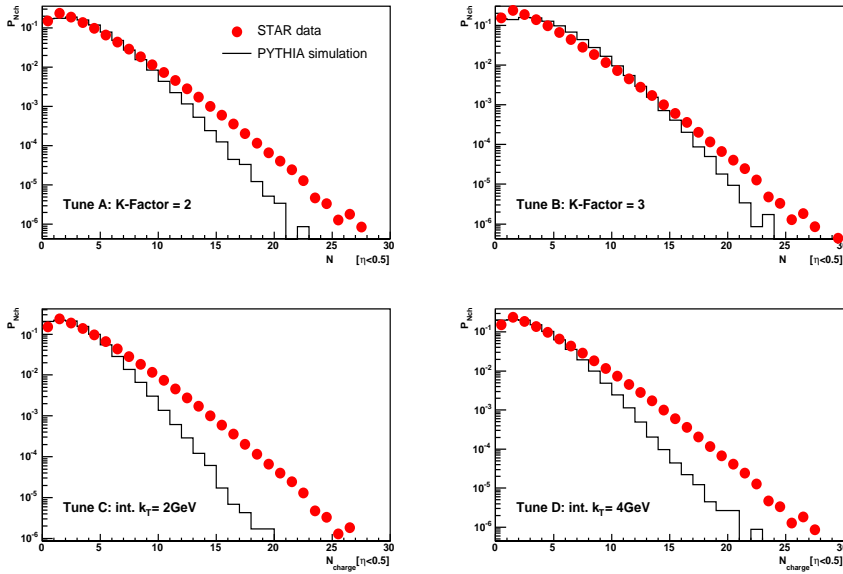


Figure 7.8: N_{ch} distribution for $p + p$ minbias at $|y| < 0.5$ from PYTHIA vs STAR data for different tunes.

Transverse momentum spectra

Figure 7.9 and 7.10 show the comparison of the K_s^0 and Λ p_T spectra to different PYTHIA settings.

There is a large discrepancy between the data and the default version of PYTHIA for $p_T > 1 \text{ GeV}/c$. By tuning the K-Factor to 3 (Tune B), a value suggested by figure 7.7, we get a much better description for K_s^0 and Λ , although for the latter the simulation still underestimates the yield at high p_T . Augmenting the intrinsic k_T to 4 GeV/c , does improve the simulation prediction for Λ in the intermediate p_T regime (1-3 GeV/c), however at high p_T it overpredicts the particle yields.

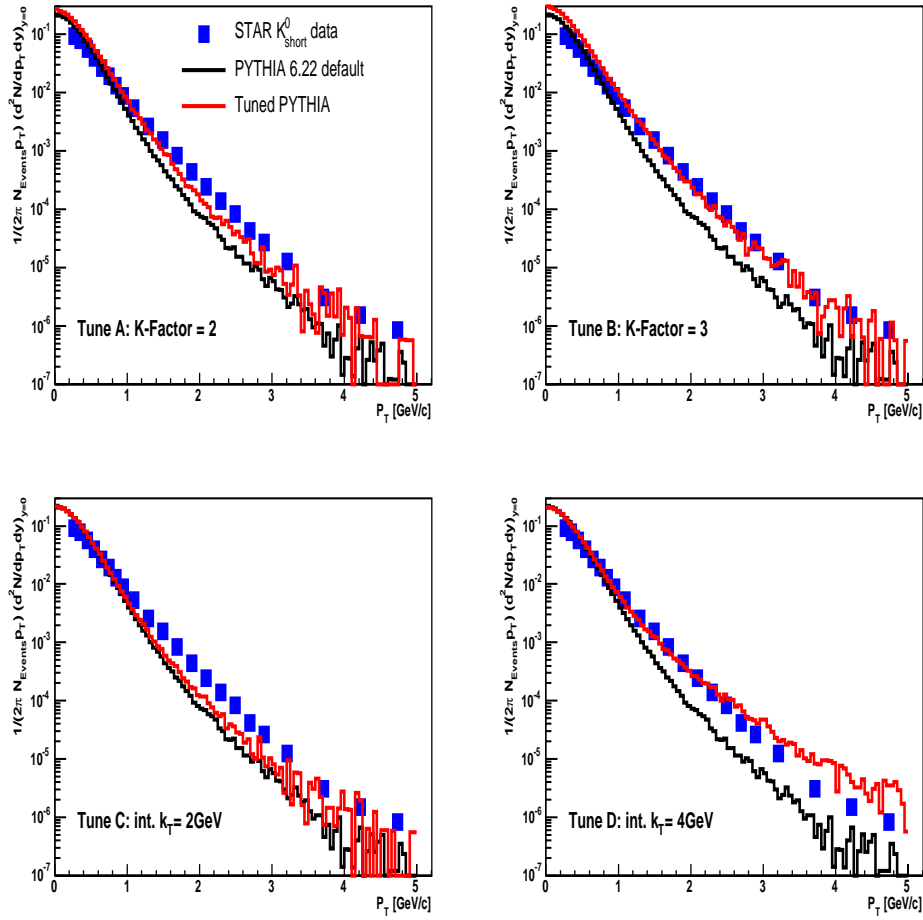


Figure 7.9: K_s^0 particle spectra (squares) for $p+p$ minbias at $|y| < 0.5$ compared to default (black line) and tuned (red line) PYTHIA (v6.221, MSEL1)

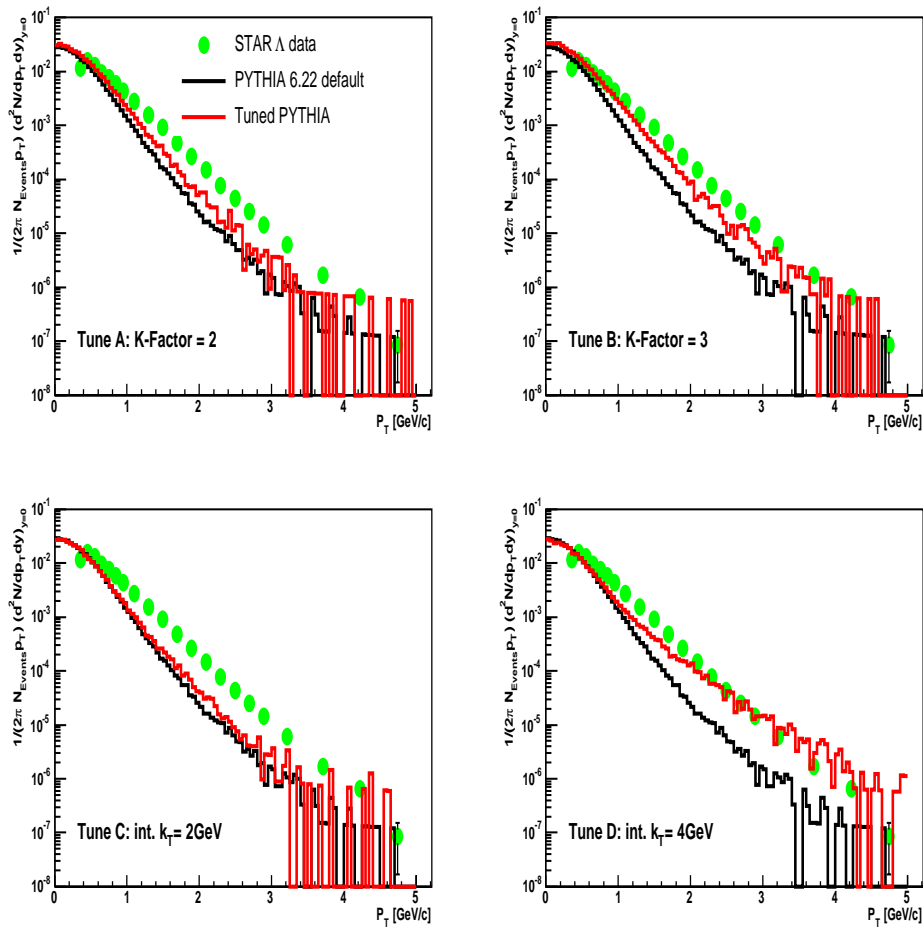


Figure 7.10: Λ particle spectra (circles) for $p+p$ minbias at $|y| < 0.5$ compared to default (black line) and tuned (red line) PYTHIA (v6.221, MSEL1)

$\langle p_T \rangle$ vs multiplicity

Now let's see how well PYTHIA reproduces our results of $\langle p_T \rangle$ vs N_{ch} . As stated previously, the dependence of $\langle p_T \rangle$ as a function of event multiplicity in $p + p$ collisions has been used to explain the particle production via mini-jets [70]. Therefore it is interesting to see how well this dependency is modeled by the processes incorporated in PYTHIA. Figure 7.11 shows the comparison of our data to the Pythia model for the four different tune settings.

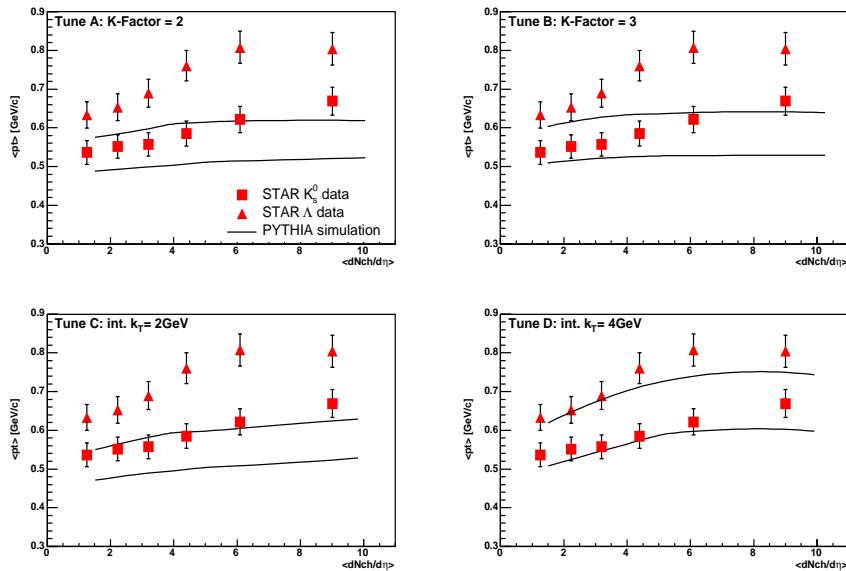


Figure 7.11: $\langle p_T \rangle$ vs N_{ch} for K_s^0 (square) and Λ (triangles) from data compared to different tuned PYTHIA results (black lines). Lower line is K_s^0 , upper is Λ .

Clearly, in all but one setting, the simulation is quite far from being a good description of the data. Although Tune B, with K-Factor = 3, does a good job at describing the minimum bias value of $\langle p_T \rangle$, it fails to describe the more detailed dependency on N_{ch} .

Tune D, ie. $k_T = 4$ GeV/c, on the other hand is a reasonable reproduction of the value as well as the shape of the $\langle p_T \rangle$ increase with charged multiplicity. However this value of k_T is larger than any theoretical prediction to date.

Similar discrepancies between data and PYTHIA have been observed for charged particle $\langle p_T \rangle$ by CDF collaboration [63].

7.3.2 PYTHIA Summary

In the previous pages we have discussed in detail the differences of the tested PYTHIA tunes. Clearly the addition of a K-Factor as well as the increasing of the intrinsic k_T value are needed to reproduce our experimental data. In table 7.3 we have summarized the yield and $\langle p_T \rangle$ values for data and the different PYTHIA settings.

Source	K_s^0 dN/dy	$K_s^0 \langle p_T \rangle$	Λ dN/dy	$\Lambda \langle p_T \rangle$	$\bar{\Lambda} / \Lambda$
experiment	0.136 ± 0.013	0.60 ± 0.04	0.043 ± 0.005	0.77 ± 0.06	0.92 ± 0.03
default 6.221	0.141	0.46	0.027	0.54	0.97
Tune A (K=2)	0.184	0.50	0.035	0.60	0.97
Tune B (K=3)	0.224	0.52	0.041	0.63	1.00
Tune C ($k_T = 2$)	0.145	0.49	0.028	0.57	0.97
Tune D ($k_T = 4$)	0.156	0.55	0.030	0.67	0.96
default 6.317	0.153	0.51	0.029	0.63	0.97

Table 7.3: Comparison of dN/dy and $\langle p_T \rangle$ obtained from PYTHIA and experiment

A substantially updated version of Pythia, 6.317, was released in December 2004 and first comparisons have just been finished. It is apparent that the agreement with our data as seen in figure 7.12 is much better than the

previous default version. According to the authors, important modifications includes a total re-write of the multiple parton-parton interactions as well as a new algorithm for p_T ordered gluon radiation (initial and final state) [24].

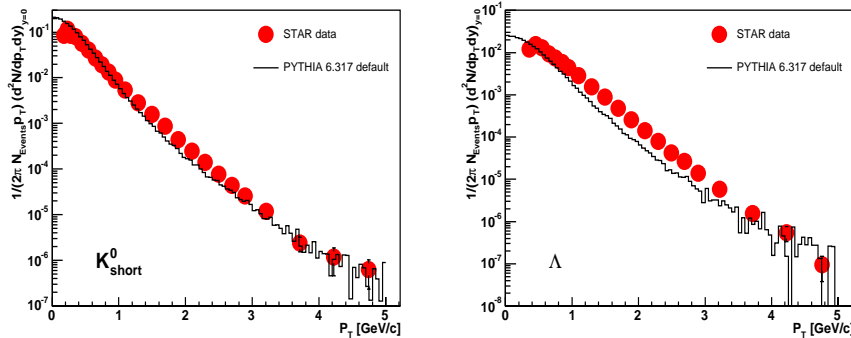


Figure 7.12: Comparison of most recent version of PYTHIA (6.317) to K_s^0 (left) and Λ (right)

7.3.3 Next-to-leading order calculations (NLO)

A number of next-to-leading order perturbative calculations have been performed to reproduce high energy particle physics data in the last 10 years. These calculations were shown to be very successful in reproducing the inclusive hadron cross-sections in $\bar{p} + p$ collisions at SPS and Fermilab [72, 73]. Due to the perturbative nature of these calculations, ie. requiring fairly large momentum transfers, these predictions start at a transverse momentum scale of $p_T > 1.5$ GeV/c.

Predictions for particle species separated spectra have been recently performed for pions at RHIC and show good agreement [81]. NLO calculations have also been successful in describing heavy quark production [80].

As more and more precise data are becoming available from $e^+ + e^-$ collisions, the fragmentation functions are being better constrained and even quark flavor separation is possible. Very recently NLO calculations for K^0 and Λ have been obtained based on fragmentation functions from KKP (K_s^0) [74] and Vogelsang et al (Λ) [75]. The comparisons to these calculations are shown in figure 7.13. The dashed lines represent the theoretical uncertainties in the renormalization and factorization scale. The agreement is quite good for K_s^0 , however for Λ there is a large discrepancy.

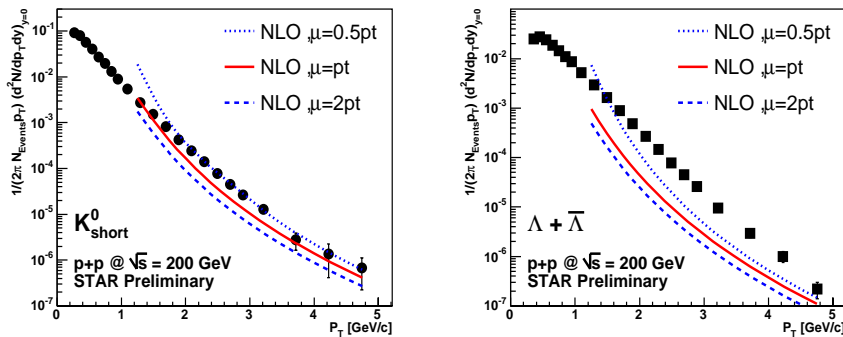


Figure 7.13: Comparisons of NLO calculation from W. Vogelsang with STAR data for K_s^0 (left) and Λ (right). μ is the factorization scale of the calculation and its variation gives an estimate of the uncertainty.

A satisfactory explanation for this large discrepancy has not yet been found. One speculation is that this may be due to the specific production mechanism of octet baryons, another is that it is due to the break-down of the massless quark formalism which cause the (m/p_T) -scale approximations to become non-negligible.

More recently Albino, Kramer and Kniehl (AKK) have analyzed new light flavor tagged OPAL data in $e^+ + e^-$ at $\sqrt{s} = 91.2$ GeV [78]. Using this

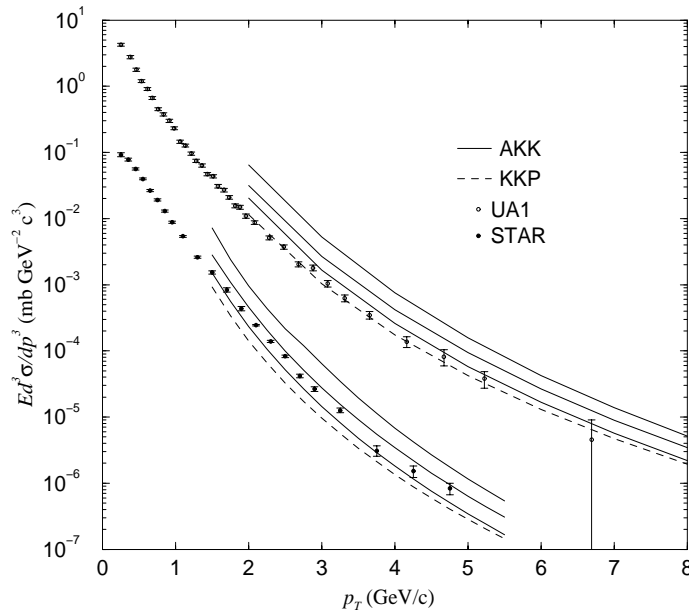


Figure 7.14: NLO calculations for K_s^0 by Albino, Kramer and Kniehl (AKK) (full lines) together with $p + p$ data from STAR at $\sqrt{s} = 200$ GeV (lower points, scaled down by 30) and $\bar{p} + p$ data from UA1 at $\sqrt{s} = 630$ GeV (upper points). Dashed lines are previous NLO calculations by Kramer, Kniehl and Potter (KKP) with older parametrizations. Taken from [77]

data, the authors obtain for the first time phenomenological descriptions of individual light quark flavor fragmentation functions. With these FF they calculate p_T -spectra for K_s^0 in NLO at $\sqrt{s} = 200$ GeV and $\sqrt{s} = 630$ GeV as shown in figure 7.14. It is interesting to notice that these new calculations now fit the STAR data much better, however they fit the UA1 data less well.

Elementary particle collision data for strange baryons has also been obtained from the OPAL experiment. Bourelly and Souffer have attempted to extract the fragmentation functions for these rarer octet baryons [76]. However we have not yet obtained a full NLO calculation of p_T -spectra from these

authors to compare our data to.

Clearly, the high statistics STAR data measured for strange baryons should provide us with a unique opportunity to test the validity of these NLO predictions.

7.3.4 EPOS v1.02 (formerly NEXUS)

The EPOS model is quite a different phenomenological approach to a standard leading-order string fragmentation models such as PYTHIA. Multiple scatterings between parton ladders (pomeron) before the hard scattering process are the pre-dominant interaction channels in this model.

It has been quite successful in describing multiplicities in both $p + p$ and heavy ion collisions [32, 33, 37]. I have obtained the latest version of the EPOS event generator code from the author and have compared the model results to our data.

The charged multiplicity distribution is shown in figure 7.15 and agrees very well with the distribution from $p + p$ collisions at STAR. The maximum deviation is seen at low N_{ch} where the model underpredicts the data by $\approx 15\%$.

Figure 7.16 and table 7.4 shows the comparison of the K_s^0 and Λ p_T -spectra to the EPOS model. The EPOS model agrees very well with the measured particle spectra; within 18% for K_s^0 and 25% for Λ .

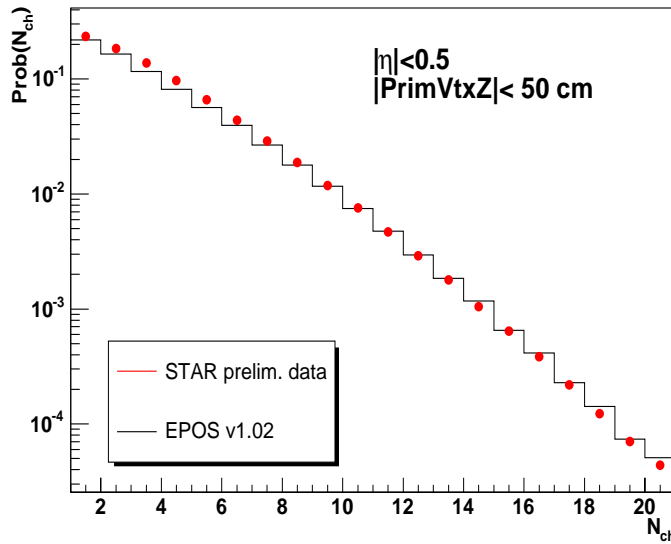


Figure 7.15: Comparison of charged multiplicity distributions N_{ch} for $p + p$ minbias between data and EPOS v1.02.

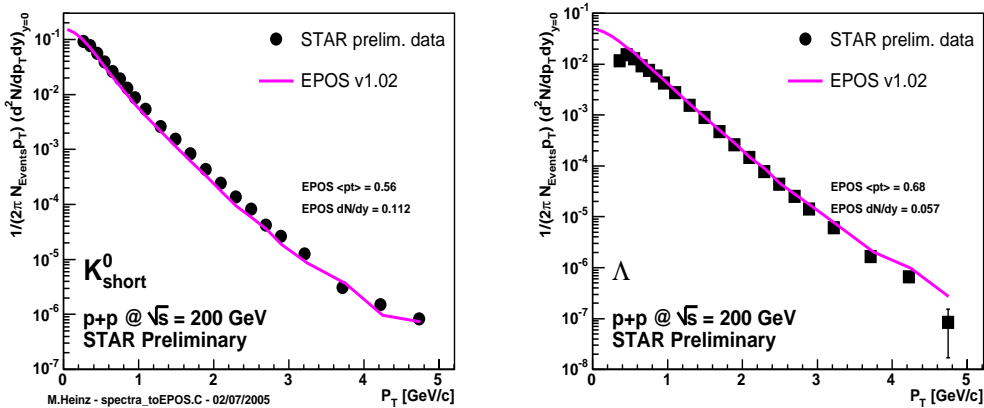


Figure 7.16: Comparison of most recent version of EPOS to $p + p$ minbias p_T -spectra for K_s^0 (left) and Λ (right)

Source	K_s^0 dN/dy	$K_s^0 \langle p_T \rangle$	Λ dN/dy	$\Lambda \langle p_T \rangle$
experiment	0.136 ± 0.013	0.60 ± 0.04	0.043 ± 0.005	0.77 ± 0.06
EPOS v1.02	0.112	0.56	0.057	0.68
$\Delta\%$	18	10	25	12

Table 7.4: Comparison of dN/dy and $\langle p_T \rangle$ obtained from EPOS and experiment. Statistical and systematical errors shown for data.

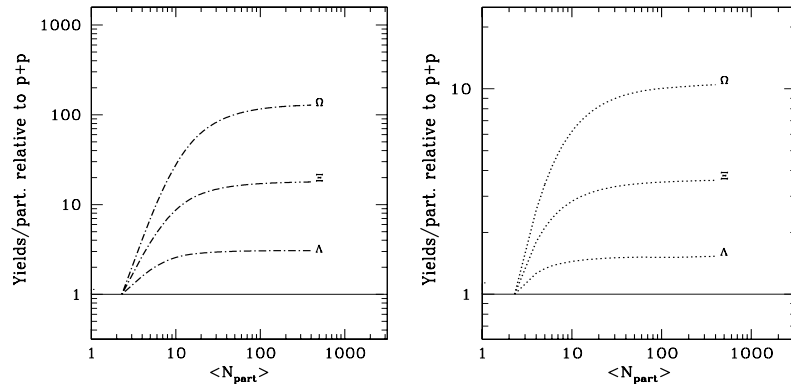
7.4 Strangeness Enhancement at STAR

At the beginning of this thesis we introduced strangeness and the concept of its enhancement as a signature of quark gluon plasma in heavy ion collisions. The $p + p$ measurement for Λ particles is important in order to compare to measurements in heavy ion experiments. A common way of defining strangeness enhancement is given in equation 7.1 and has been calculated for strange (anti-) baryons in STAR [87].

$$E = \frac{(Yield/N_{part})_{Au+Au}}{(Yield/N_{part})_{p+p(A)}} \quad (7.1)$$

Here N_{part} defines the number of participants and is a measure of the collision volume. The statistical hadronization model by Rafelski has predicted an enhancement of multi-strange (anti-) baryons with respect to singly strange particles [18]. Other statistical models by Redlich *et al* also predict the enhancement as a function of correlation volume or N_{part} and a function of strangeness content as shown in figure 7.17 [83].

Figure 7.18 we show enhancement values for STAR and NA57 (CERN SPS) at two different collision energies and for Λ and Ξ^- particles and their anti-particles [82]. The values from the Ξ^- analysis in STAR are documented here [85, 86]. As predicted, the multi-strange Ξ^- is more enhanced than the singly strange Λ at both energies. Also, as predicted by Redlich and others, the enhancement at $\sqrt{s} = 17.3$ GeV is slightly stronger than at $\sqrt{s} = 200$ GeV. For the anti-baryons the enhancement differences for identical particles between the STAR and NA57 measurement are indicative of a lower net-baryons density at RHIC. A rather unexpected feature of the measurement in figure 7.18 is the fact that the enhancement continues to grow as a function of centrality and does not saturate as shown in figure 7.17.



(a) Enhancement vs. centrality in Pb+Pb at $\sqrt{s} = 8.73$ GeV
 (b) Enhancement vs. centrality in Pb+Pb at $\sqrt{s} = 130$ GeV

Figure 7.17: Prediction of strange baryon enhancement in Pb+Pb collisions with respect to $p + p$ collisions at $\sqrt{s} = 8.73$ GeV and $\sqrt{s} = 130$ GeV. Taken from [84]

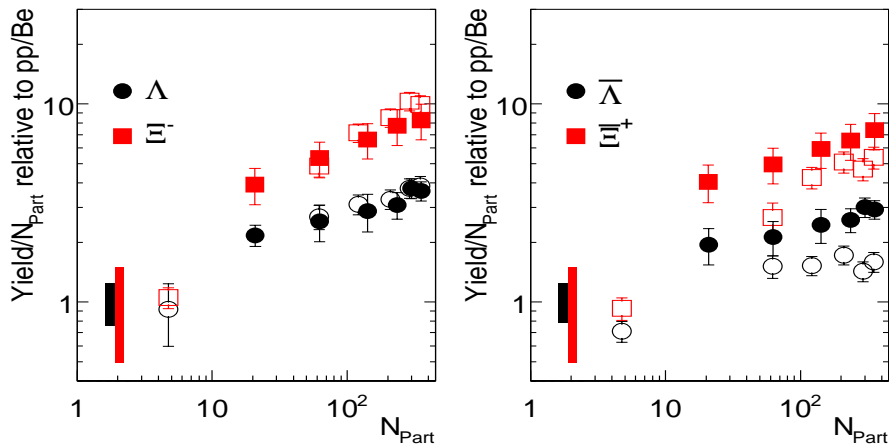


Figure 7.18: Strangeness enhancement for Λ and Ξ^- in central collisions at STAR (full symbols) and NA57 (open symbols, $\sqrt{s} = 17.3$ GeV). Left panel is for particles, right panel is for anti-particles.

7.5 Nuclear modification factor

The strangeness enhancement plots shown previously were on the basis of integrated particle yields, which are dominated by the low p_T , non-perturbative part of the spectrum. More recently, with new high statistics RHIC data at hand, the heavy ion community has started to look at the particle production as a function of p_T . In order to learn more about the perturbative QCD processes one has to look at intermediate and high p_T .

$$R_{AA}(p_T) = \frac{d^2 N^{AA}/dp_T dy}{\langle N_{bin} \rangle d^2 N^{pp}/dp_T dy} \quad (7.2)$$

The so-called nuclear modification factor, as defined in equation 7.2, is a way of analyzing high- p_T suppression in heavy ion collisions. It is simply an appropriately scaled “heavy-ion-to- $p + p$ -ratio” of differential particle yields assuming the nuclear collision to be a superposition of elementary binary collisions. Nuclear effects are then seen as deviation from unity. The necessary baseline for the R_{AA} factor is the measurement in $p+p$ where nuclear effects are absent.

This measurement has been successfully performed at $\sqrt{s} = 200$ GeV by STAR for inclusive hadrons and its result has yielded quite some excitement in the heavy ion community [90]. It shows a clear suppression of hadron production at intermediate p_T , 5-10 GeV/c, with respect to binary collisions and therefore provides stringent model constraints for partonic loss of energy in the QGP phase.

With the high- p_T strange particle measurements we are now in the position to extend the nuclear modification measurement to the particle identified level. Astonishing differences between the suppression of mesons and baryons have already been observed in STAR via the R_{CP} ratio (CP=’central to peripheral’) as shown in figure 7.19 [91]. One type of model successful in

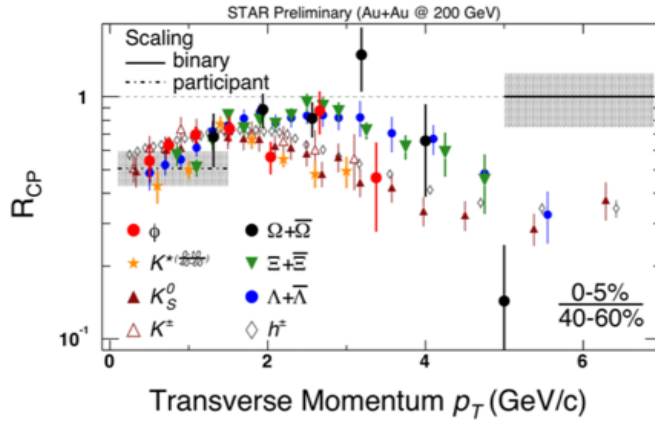


Figure 7.19: Nuclear modification factor R_{CP} for mesons and baryons at $\sqrt{s} = 200$ GeV. Taken from [92].

describing this novel phenomenology between mesons and baryons has been the recombination models [93, 95].

With the $p + p$ measurements for Λ and K_s^0 in this thesis we can now similarly produce an R_{AA} ratio for identified strange particles as shown in figure 7.20. Whereas all mesons species seem to be suppressed with respect to binary scaling, the baryons show an enhancement as a function of particle species. Since this enhancement above unity is not present in R_{CP} , it could be related to a suppression of these baryons at in $p + p$ collisions. Further studies and comparisons to models are ongoing to understand these new effects.

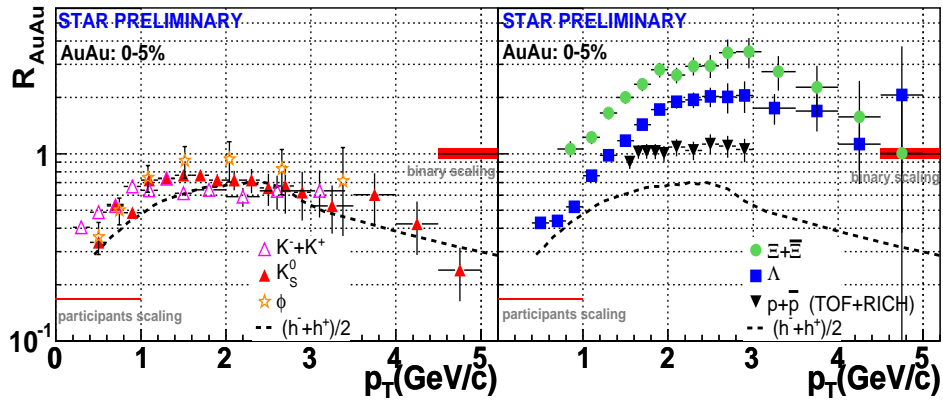


Figure 7.20: Nuclear modification factor for mesons (left) and baryons (right) in STAR at $\sqrt{s} = 200$ GeV [88]

7.6 Conclusions

The aim of this thesis was to investigate the properties of strange particles in $p + p$ collisions at STAR. By doing so we had two separate goals in mind:

1. Constrain pQCD and phenomenological models with high p_T data, thereby advancing the understanding of mini-jet production
2. Establish a baseline measurement of strange particle production in a smaller system in order to compare to heavy ion collision

The experimental challenge we faced in this measurement included the low primary vertex efficiency due to the low multiplicity environment in $p + p$ collisions as well as the contamination of reconstructed events by “pile-up”. We have shown methods to correct for both these effects in this thesis.

Our measurement of K_s^0 , Λ and $\bar{\Lambda}$ transverse momentum spectra are consistent with previous measurements by $Spp\bar{S}$ $\bar{p} + p$ experiments but significantly improved in precision. They clearly unveil the pQCD nature of the high p_T part of the spectrum and the need for a parametrization inspired by such processes. In order to account also for the low p_T shape of the spectra a combined (m_T -exponential plus power-law) function has to be applied.

We have studied the dependance of strange particle $\langle p_T \rangle$ with charged event multiplicity. The observed behavior is indicative of multiple mini-jet production at high multiplicity. Moreover, there is a particle mass dependance of $\langle p_T \rangle$ which also indicates that higher mass strange particles are pre-dominantly produced via mini-jet fragmentation.

In order to further investigate these assumptions we compared our measurements to different phenomenological pQCD models. We show that tuned PYTHIA and NLO describe the K_s^0 p_T -spectrum quite well, whereas the Λ p_T -spectrum shows significant discrepancies between data and model. The

EPOS model is able to reproduce both the K_s^0 and Λ p_T -spectrum well but its parameters have been tuned specifically to RHIC.

Heavy ion related subjects such as strangeness enhancement and nuclear modification factors rely on high precision $p+p$ data as a reference. We have shown that strangeness enhancement factors for Λ and Ξ^- are only slightly lower than at $\sqrt{s} = 17.3$ GeV in contradiction with statistical models. The nuclear modification factor for baryons and mesons is clearly different. For mesons it is consistent with binary scaling in the intermediate p_T -range (2-3 GeV/c) whereas for baryons it reaches values of 2-3 times the binary scaling value in the same range. It remains to be understood whether this effect is produced by an enhancement in Au+Au or a canonical suppression of strange baryons in $p+p$ or a combination of both.

A separate part of this thesis was motivated by recent experimental evidence of exotic baryons (pentaquarks). The confirmation of the existence of such particles in hadronic/nuclear collisions would be very important. Preliminary results of the search for θ^+ pentaquark in $p+p$ and $d+Au$ collisions show a peak structure in the $p+K_s^0$ invariant mass around 1550 MeV with a width consistent with predictions for θ^+ . However the significance of our measurement is small, i.e. $sig = S/\sqrt{B} = 3 - 5$. This analysis remains to be confirmed by other authors of the RHIC experiments.

7.7 Outlook

The usage of high- p_T identified particles is going to be the diagnostic tool of the future in order to probe the strongly interacting medium of quarks and gluons produced at RHIC. Exciting measurements of jet-quenching in azimuthally correlations have been recently published and with the future

heavy ion runs more statistics will be available for more precise measurements. This will allow for a particle species dependant nuclear modification factor measurement which will help constrain fragmentation and recombination models.

With more statistics the measurement of open charm, J/Ψ and maybe even Upsilon will become possible. First measurements of strange resonances (Σ^* , Λ^* , $\Xi^*(1530)$) can be significantly improved with more statistics.

New heavy ion species (Cu-Cu) have been tested this year at RHIC and will yield interesting results for strangeness enhancement and nuclear modification factors in a smaller collision volume. Cu-Cu may also be a more ideal environment to search for penta-quark candidates and solve the mystery of their existence.

Appendix A

Table of values

A.1 Table of p_T -Spectra

$\langle p_T \rangle$	dp_T	$\frac{1}{2\pi p_T} \frac{d^2N}{dp_T dy}$	σ
0.25	0.1	0.0926529	0.00826534
0.35	0.1	0.0824857	0.00504225
0.45	0.1	0.0586867	0.00280398
0.55	0.1	0.041718	0.00174837
0.65	0.1	0.0284763	0.00116154
0.75	0.1	0.0198238	0.000822002
0.85	0.1	0.0136211	0.000598307
0.95	0.1	0.00916605	0.00042273
1.1	0.2	0.0055656	0.000216744
1.3	0.2	0.00257896	0.000122538
1.5	0.2	0.00144624	9.41167e-005
1.7	0.2	0.000809657	7.01683e-005
1.9	0.2	0.000394681	3.99227e-005
2.1	0.2	0.0002247	1.09142e-005
2.3	0.2	0.000128021	8.40501e-006
2.5	0.2	7.36452e-005	6.5605e-006
2.7	0.2	4.33391e-005	3.72183e-006
2.9	0.2	2.47779e-005	2.94988e-006
3.25	0.5	1.28031e-005	1.34665e-006
3.75	0.5	2.58393e-006	4.92225e-007
4.25	0.5	1.5506e-006	3.16061e-007
4.75	0.5	8.39443e-007	1.80149e-007

Table A.1: K_s^0 spectra values as plotted in figure 5.1

$\langle p_T \rangle$	dp_T	$\frac{1}{2\pi p_T} \frac{d^2N}{dp_T dy}$	σ
0.35	0.1	0.0128186	0.00196229
0.45	0.1	0.0155991	0.00122722
0.55	0.1	0.0128203	0.000759373
0.65	0.1	0.0101679	0.00051343
0.75	0.1	0.00766237	0.000358084
0.85	0.1	0.00591732	0.000274488
0.95	0.1	0.00447281	0.00021405
1.1	0.2	0.00294808	0.000106516
1.3	0.2	0.00167849	7.14312e-005
1.5	0.2	0.000996602	5.01891e-005
1.7	0.2	0.000508311	3.24017e-005
1.9	0.2	0.000254947	1.99775e-005
2.1	0.2	0.000133821	7.80711e-006
2.3	0.2	7.80001e-005	5.66102e-006
2.5	0.2	3.94826e-005	4.01571e-006
2.7	0.2	2.57e-005	2.46792e-006
2.9	0.2	1.36181e-005	1.73119e-006
3.25	0.5	6.29007e-006	7.36025e-007
3.75	0.5	1.69871e-006	3.36162e-007
4.25	0.5	6.65798e-007	2.09785e-007
4.75	0.5	1.8251e-007	9.73668e-008

Table A.2: Λ spectra values as plotted in figure 5.1

$\langle p_T \rangle$	dp_T	$\frac{1}{2\pi p_T} \frac{d^2 N}{dp_T dy}$	σ
0.35	0.1	0.0133512	0.00182435
0.45	0.1	0.0146274	0.00117509
0.55	0.1	0.0105969	0.000607045
0.65	0.1	0.00959344	0.000473109
0.75	0.1	0.00749317	0.000358943
0.85	0.1	0.00538405	0.000255187
0.95	0.1	0.00399347	0.000188739
1.1	0.2	0.00254867	9.47139e-005
1.3	0.2	0.00151729	6.51801e-005
1.5	0.2	0.00080437	4.15496e-005
1.7	0.2	0.000424614	2.74004e-005
1.9	0.2	0.000214342	1.68881e-005
2.1	0.2	0.000128756	7.26368e-006
2.3	0.2	6.91812e-005	5.07914e-006
2.5	0.2	3.52971e-005	3.4935e-006
2.7	0.2	1.91587e-005	2.31176e-006
2.9	0.2	1.18192e-005	1.67246e-006
3.25	0.5	4.05697e-006	6.25167e-007
3.75	0.5	1.71072e-006	3.12035e-007
4.25	0.5	7.09907e-007	1.80417e-007
4.75	0.5	2.3274e-007	1.10701e-007

Table A.3: $\bar{\Lambda}$ spectra values as plotted in figure 5.1

A.2 Table of $\langle p_T \rangle$ vs N_{ch}

Bin	N_{ch}	N_{ch}	$\langle p_T \rangle$	σ
0	1.42035	1.25598	0.53296	0.0145784
1	3.48482	2.23398	0.546942	0.00882868
2	5.45651	3.19684	0.554363	0.00802536
3	7.85482	4.39639	0.585034	0.00758939
4	11.1991	6.09326	0.630905	0.009208
5	16.7723	9.00727	0.675298	0.0118785

Table A.4: $K_s^0 \langle p_T \rangle$ from composite fit values as plotted in figure 5.7

Bin	N_{ch}	N_{ch}	$\langle p_T \rangle$	σ
0	1.42035	1.25598	0.499201	0.00598974
1	3.48482	2.23398	0.50989	0.00370631
2	5.45651	3.19684	0.527044	0.00354131
3	7.85482	4.39639	0.559267	0.00332646
4	11.1991	6.09326	0.597709	0.00385848
5	16.7723	9.00727	0.638776	0.0048305

Table A.5: $K_s^0 \langle p_T \rangle$ from powerlaw fit vs N_{ch} as plotted in figure 5.7

Bin	N_{ch}	$\langle p_T \rangle$	σ
0	1.25598	0.0268342	0.000519026
1	2.23398	0.080092	0.000914174
2	3.19684	0.140259	0.00143577
3	4.39639	0.209432	0.00192112
4	6.09326	0.305604	0.00315388
5	9.00727	0.481779	0.0059924

Table A.6: K_s^0 dN/dy values from composite fit as plotted in figure 5.9

Bin	N_{ch}	$\langle p_T \rangle$	σ
0	1.25598	0.0291896	0.000564585
1	2.23398	0.0873815	0.000997377
2	3.19684	0.14946	0.00152996
3	4.39639	0.221713	0.00203377
4	6.09326	0.327135	0.00337608
5	9.00727	0.516773	0.00642765

Table A.7: K_s^0 dN/dy values from powerlaw fit as plotted in figure 5.9

Bin	N_{ch}	N_{ch}	$\langle p_T \rangle$	σ
0	1.42035	1.25598	0.649925	0.0507249
1	3.48482	2.23398	0.656494	0.0234102
2	5.45651	3.19684	0.695579	0.0191059
3	7.85482	4.39639	0.768923	0.017503
4	11.1991	6.09326	0.812269	0.0197042
5	16.7723	9.00727	0.845597	0.0226975

Table A.8: Λ $\langle p_T \rangle$ values from composite fit as plotted in figure 5.8

Bin	N_{ch}	N_{ch}	$\langle p_T \rangle$	σ
0	1.42035	1.25598	0.683139	0.0261156
1	3.48482	2.23398	0.711955	0.0151057
2	5.45651	3.19684	0.736448	0.0119998
3	7.85482	4.39639	0.808279	0.0107625
4	11.1991	6.09326	0.850868	0.0112067
5	16.7723	9.00727	0.907416	0.0132835

Table A.9: Λ $\langle p_T \rangle$ values from m_T -exp fit as plotted in figure 5.8

Bin	N_{ch}	dN/dy	σ
0	1.25598	0.0075541	0.000416894
1	2.23398	0.023367	0.000589198
2	3.19684	0.0425934	0.000827274
3	4.39639	0.0660275	0.00106277
4	6.09326	0.103725	0.0017792
5	9.00727	0.180169	0.00341964

Table A.10: Λ dN/dy values from composite fit as plotted in figure 5.10

Bin	N_{ch}	dN/dy	σ
0	1.25598	0.00686662	0.000378954
1	2.23398	0.0203899	0.000514133
2	3.19684	0.0385404	0.000748553
3	4.39639	0.0608498	0.00097943
4	6.09326	0.0967386	0.00165937
5	9.00727	0.162715	0.00308835

Table A.11: Λ dN/dy values from m_T -exp fit as plotted in figure 5.10

Bibliography

- [1] E.O. Lawrence and D.H.Sloan, Phys. Rev. **38**, 20212032 (1931)
- [2] J. Schaffner-Bielich, astro-ph/0412215.
- [3] P. Haensel, J. L. Zdunik and R. Schaeffer, Astron. Astrophys. **160**, 121 (1986).
- [4] S. Bethke, alpha(s) 2002, Proceedings of the QCD 02 conference in Montpellier, France, hep-ex/0211012
- [5] D. Gross and F. Wilczek, Phys. Rev. Lett. **30**, 1343 (1973).
- [6] M. Banner *et al.* [UA2 Collaboration], Phys. Lett. B **118**, 203 (1982)
- [7] W. Thome *et al.* [Aachen-CERN-Heidelberg-Munich Collaboration], Nucl. Phys. B **129**, 365 (1977)
- [8] G. Arnison *et al.* (UA1 Collaboration), Phys. Lett. B **107**, 320 (1981)
- [9] Z. Koba, H.N. Nielson and P. Oleses, Nucl. Phys. B **40**, 317 (1972)
- [10] J. Adams *et al.* [STAR Collaboration], nucl-ex/0501009.
- [11] J. D. Bjorken, Phys. Rev. D **27**, 140 (1983).
- [12] J. Rafelski and B. Muller, Phys. Rev. Lett. **48**, 1066 (1982)

- [13] P. Koch, B. Muller and J. Rafelski, Phys. Rept. **142**, 167 (1986).
- [14] J. Rafelski and J. Letessier, J. Phys. G **30**, S1 (2004)
- [15] G. Bocquet *et al.* [UA1 Collaboration], Phys. Lett. B **366**,447 (1996)
- [16] A. Wroblewski, Acta Phys. Polon. B **16**, 379 (1985).
- [17] S. Kabana, Eur. Phys. J. C **21**, 545 (2001)
- [18] J. Rafelski, Phys. Lett. B **262**, 333 (1991).
- [19] F. Becattini and U. W. Heinz, Z. Phys. C **76**, 269 (1997)
- [20] F. Becattini, J. Cleymans, A. Keranen, E. Suhonen and K. Redlich, Phys. Rev. C **64**, 024901 (2001)
- [21] P. Braun-Munzinger, I. Heppe and J. Stachel, Phys. Lett. B **465**, 15 (1999)
- [22] P. Braun-Munzinger, D. Magestro, K. Redlich and J. Stachel, Phys. Lett. B **518**, 41 (2001)
- [23] R. K. Ellis, D. A. Ross and A. E. Terrano, Nucl. Phys. B **178**, 421 (1981).
- [24] T. Sjostrand and P. Z. Skands, Eur. Phys. J. C **39**, 129 (2005)
- [25] H. U. Bengtsson and T. Sjostrand, Comput. Phys. Commun. **46**, 43 (1987).
- [26] T. Sjostrand, Comput. Phys. Commun. **27**, 243 (1982).
- [27] B. Andersson, G. Gustafson and T. Sjostrand, Nucl. Phys. B **197**, 45 (1982).

- [28] B. Andersson, G. Gustafson, G. Ingelman and T. Sjostrand, Phys. Rept. **97**, 31 (1983).
- [29] J. Binnewies, B. A. Kniehl and G. Kramer, Phys. Rev. D **52**, 4947 (1995)
- [30] G. Altarelli and G. Parisi, Nucl. Phys. B **126**, 298 (1977).
- [31] B. A. Kniehl, G. Kramer and B. Potter, Nucl. Phys. B **597**, 337 (2001)
- [32] K. Werner, Phys. Lett. B **208**, 520 (1988).
- [33] K. Werner, Phys. Rept. **232**, 87 (1993).
- [34] V. N. Gribov, Sov. Phys. JETP **26**, 414 (1968)
- [35] A. Capella, U. Sukhatme, C. I. Tan and J. Tran Thanh Van, Phys. Rept. **236**, 225 (1994).
- [36] N. N. Kalmykov and S. S. Ostapchenko, Sov. J. Nucl. Phys. **50**, 315 (1989)
- [37] H. J. Drescher, M. Hladik, S. Ostapchenko, T. Pierog and K. Werner, Phys. Rept. **350**, 93 (2001)
- [38] X. Artru and G. Mennessier, Nucl. Phys. B **70**, 93 (1974).
- [39] X. N. Wang and M. Gyulassy, Comput.Phys.Commun. 83,307 (1994)
- [40] X. N. Wang, Phys. Rept. **280**, 287 (1997)
- [41] X. N. Wang and R. C. Hwa, Phys. Rev. D **39**, 187 (1989)
- [42] T. K. Gaisser and F. Halzen, Phys. Rev. Lett. **54**, 1754 (1985)
- [43] K.H. Ackermann *et al.* [STAR Collaboration], Nucl. Phys. A**661** (1999)
681

- [44] K.H. Ackermann *et al.*[STAR Collaboration], Nucl. Instrum. Meth. **A499** (2003) 624
- [45] K.H. Ackermann *et al.* [STAR Collaboration], Nucl. Instrum. Meth. **A499** (2003) 659
- [46] K.H. Ackermann *et al.* [STAR Collaboration], Nucl. Instrum. Meth. **A499** (2003) 679
- [47] H. Bichsel , STAR Technical Note 441, 2002
- [48] R. Bellwied *et al.* [STAR Collaboration], Nucl. Instrum. Meth. **A499** (2003) 640
- [49] R. Bossingham *et al.* Technical report, STAR Note 281, “STAR Offline Simulations and Analysis Software Design”, 1997
- [50] W. Blum, L. Rolandi, “Particle detection with Drift chambers”, Springer Berlin, 1993
- [51] M. Calderon de la Barca Sanchez, PhD Thesis, Yale University, 2001
- [52] J. Gans, PhD Thesis, Yale University, 2004
- [53] S. Salur (for the STAR collaboration), HotQuarks 2004 conference, *J. Phys. G* **31** (2005) S179
- [54] R. Hagedorn, Nuovo Cim. Suppl. **3**, 147 (1965).
- [55] R. Hagedorn and J. Ranft, Nuovo Cim. Suppl. **6**, 169 (1968).
- [56] G. Arnison *et al.* [UA1 Collaboration], Phys. Lett. **B132**,223 (1983)
- [57] R. E. Ansorge *et al.* [UA5 Collaboration], Nucl. Phys. **B328**,36 (1989)

- [58] R. E. Ansorge *et al.* [UA5 Collaboration], Phys. Lett. B **199**, 311 (1987)
- [59] P. Braun-Munzinger, K. Redlich and J. Stachel, nucl-th/0304013.
- [60] C. Adler *et al.* [the STAR Collaboration], Phys. Rev. Lett. **86**, 4778 (2001)
- [61] T. Alexopoulos *et al.* [E735 Collaboration], Phys. Rev. Lett. **64**, 991 (1990).
- [62] T. Sjöstrand and M. Van Zijl, Phys. Rev. D **36**, 2019 (1987)
- [63] D. Acosta *et al.* [CDF Collaboration], Phys. Rev. D **65**, 072005 (2002).
- [64] L. D. McLerran and J. Schaffner-Bielich, Phys. Lett. B **514**, 29 (2001)
- [65] A. Dumitru *et al.*, Phys. Lett. B **446**, 326 (1999)
- [66] I. Bearden *et al.* [NA44 Collaboration], Phys. Rev. Lett. **78**, 2080 (1997)
- [67] P. F. Kolb, J. Sollfrank and U. W. Heinz, Phys. Rev. C **62**, 054909 (2000)
- [68] B. Alper *et al.* [British-Scandinavian Collaboration], Nucl. Phys. B **100**, 237 (1975)
- [69] X. N. Wang, Phys. Rev. C **58**, 2321 (1998)
- [70] X.N. Wang and M. Gyulassy, Phys. Lett. B **282**, 466 (1992)
- [71] X.N. Wang and M. Gyulassy, Phys. Rev. D **45**, 844 (1992)
- [72] F. M. Borzumati and G. A. Schuler, Z. Phys. C **58**, 139 (1993)
- [73] F. M. Borzumati and G. Kramer, Z. Phys. C **67**, 137 (1995)

- [74] B. A. Kniel *et al.*, Nucl. Phys. B **582**, 514 (2000)
- [75] W. Vogelsang, private communication (9/2004)
- [76] C. Bourrely and J. Soffer, Phys. Rev. D **68**, 014003 (2003)
- [77] S. Albino, B. A. Kniehl and G. Kramer, hep-ph/0502188.
- [78] G. Abbiendi *et al.* [OPAL Collaboration], Eur. Phys. J. C **16**, 407 (2000)
- [79] K. J. Eskola and H. Honkanen, Nucl. Phys. A **713**, 167 (2003)
- [80] M. van Leeuwen, SQM 2004 conference, nucl-ex/0412023.
- [81] D. d'Enterria, J. Phys. G **30**, 767 (2004)
- [82] D. Elia [NA57 Collaboration], J. Phys. G **31**, S135 (2005)
- [83] A. Tounsi, A. Mischke and K. Redlich, Nucl. Phys. A **715**, 565 (2003)
- [84] K. Redlich and A. Tounsi, Eur. Phys. J. C **24**, 589 (2002)
- [85] M. Estienne (for the STAR collaboration), SQM 2004 conference, nucl-ex/0412041
- [86] R. Witt (for the STAR collaboration), SQM 2003 conference, J. Phys. G **30** S205 (2004)
- [87] H. Caines (for the STAR collaboration), HotQuarks 2004 conference, J. Phys. G **31** (2005) S101
- [88] C. Mironov, private communications (2005)
- [89] J. Ma, private communications (2005)
- [90] C. Adler *et al.* [STAR Collaboration], Phys. Rev. Lett. **89**, 202301 (2002)

- [91] J. Adams *et al.* [STAR Collaboration], Phys. Rev. Lett. **92**, 052302 (2004)
- [92] K. Schweda (for the STAR Collaboration), J. Phys. G **30** S693 (2004)
- [93] R. J. Fries, B. Muller, C. Nonaka and S. A. Bass, Phys. Rev. Lett. **90**, 202303 (2003)
- [94] R. J. Fries, B. Muller, C. Nonaka and S. A. Bass, Phys. Rev. C **68**, 044902 (2003)
- [95] R. C. Hwa and C. B. Yang, Phys. Rev. C **70**, 024904 (2004)
- [96] S. Eidelman *et al.*, Phys. Lett. B **592**, 1 (2004)
- [97] T. Nakano *et al.* [LEPS Collaboration], Phys. Rev. Lett. **91**, 012002 (2003)
- [98] A. Dzierba *et al.* , APS Meeting 2004, hep-ex/0412077
- [99] S. Stepanyan *et al.* [CLAS Collaboration], Phys. Rev. Lett. **91**, 252001 (2003)
- [100] S. Stepanyan *et al.* [CLAS Collaboration], Phys. Rev. Lett. **92**, 032001(2004)
- [101] M. Karliner and H. Lipkin, Phys. Lett. B **597**,309 (2004)
- [102] Y. Azimov and I. Strakovsky, Phys. Rev. C **70**,035210 (2004)
- [103] R. L. Jaffe and K. Johnson, Phys. Lett. B **60**, 201 (1976).
- [104] R. Jaffe,Phys. Rev. Lett. **38**, 195 (1977).
- [105] R. Jaffe,Phys. Rev. D **15**, 281 (1977).

-
- [106] R. L. Jaffe and F. Wilczek, Phys. Rev. Lett. **91**, 232003 (2003)
- [107] J. K. Perring and T. H. R. Skyrme, Nucl. Phys. **31**, 550 (1962)
- [108] M. P. Mattis and M. Karliner, Phys. Rev. D **31**, 2833 (1985).
- [109] P. O. Mazur, M. A. Nowak and M. Praszalowicz, Phys. Lett. B **147**, 137 (1984)
- [110] D. Diakonov, V. Petrov and M. V. Polyakov, Z. Phys. A **359**, 305 (1997)
- [111] I. Abt *et al.* [HERA-B Collaboration] Phys. Rev. Lett. **93** (2004) 212003
- [112] S. Kabana, Proceedings to conference HADRON-RANP 2004, hep-ph/0501121
- [113] C. Markert (for the STAR collaboration), Winter Workshop on Nuclear Dynamics 2004, nucl-ex/0501033
- [114] C. Markert, private communications (2005)

List of Figures

2.1	Table of elementary particles and forces known in the standard model.	4
2.2	Running coupling constant, α_s , versus momentum transfer, Q . The world average measurement of α_s is given at the value of the Z boson mass (91.2 GeV). Taken from [4]	6
2.3	First observation of jets in $\bar{p} + p$ collisions by UA2 experiment at CERN. Taken from [6]	9
2.4	Space-time evolution of a heavy ion collision assuming the formation of Quark-Gluon Plasma.	12
2.5	Contributions to the Wroblewski factor λ_s in heavy ion collisions from strange baryons (red), strange mesons (blue) and mesons with hidden strangeness (green). Taken from [22] . . .	14
2.6	Yields calculated with the thermal statistical model for $\bar{p} + p$ collisions at $\sqrt{s} = 200$ GeV (top), 546 GeV (center), 900 GeV (bottom). Taken from [19]	16
2.7	Schematic of string fragmentation process	17

2.8	Fragmentation function parametrization by Kramer-Kniehl-Poetter (KKP) for charged kaons at LO (left) and NLO (right). Contributions from different quark flavor and gluons are shown separately. Taken from [29]	18
3.1	RHIC collider overview	23
3.2	STAR Experiment. Cut-away taken from [44]	26
3.3	Schematic of STAR Detector systems. Taken from [44]	27
3.4	Reconstructed tracks with the STAR Time Projection Chamber in a Au+Au collision at $\sqrt{s} = 130$ GeV. Taken from [44]	29
3.5	STAR Time Projection Chamber (TPC). Taken from [45]	30
3.6	The TPC MWPC including the configuration of the wire planes and the pad readout plane. Taken from [46].	31
3.7	TPC anode pad plane for 1 sector. The geometrical arrangement of the 5692 pads within the inner and outer sector are shown. Taken from [45].	32
3.8	TPC dedx resolution. Taken from [47]	33
3.9	Tracking efficiency for pions in Au+Au collisions in STAR vs. collision centrality at half-field magnetic setting (0.25T). Taken from [51].	34
3.10	Schematic view of Beam Beam Counter (BBC) components. The active components are the 18 small tiles (blue) arranged in a hexagonal shape. The location of the beam-pipe is designated by "B".	36
3.11	Schematic view of Central Trigger Barrel (CTB) components. The rectangular radiators have dimensions of 1cm x 21cm x 112/130cm	37

3.12	Layout of SVT ladders (left). Generic Silicon Drift Detector (right). Taken from [48]	39
3.13	Photo of STAR Silicon Vertex Tracker (SVT) detector	39
4.1	Left: Primary vertex position for Monte-Carlo simulation and reconstructed with vertex finder. Right: Distribution of quantity $\Delta(PV(z))$. Fake events are marked red.	44
4.2	Left: Global track distributions for different event types. Right: Primary vertex efficiency η_{vtx} vs number of global tracks.	45
4.3	Left: Correlation between nPrimary tracks vs nGlobal tracks from Hijing events. Right: Primary vertex finding efficiency vs. number of primary tracks	46
4.4	Left: Multiplicity distributions for events with strange particle candidates (left) and minimum bias events before and after vertex correction (right).	47
4.5	Percentage of lost vertex events as a function of the product of N_{ions} in the blue and yellow proton beams. This quantity is proportional to beam luminosity as shown in equation 4.3. The line shows the mean value of all measurements.	48
4.6	Mean number of primary (left) and global (right) tracks as a function of beam luminosity	51
4.7	Track dE/dx vs total momentum for primary (left) and global (right) tracks. Lines represent Bethe-Bloch parametrizations. Tracks are required to have minimum 10 hits.	53

4.8	Schematic of V^0 -decay topology including all used cut variables: a) Distance of Closest Approach (DCA) to primary vertex(PV), b) DCA of V^0 daughter tracks to PV, c) V^0 decay length, d) DCA of V^0 daughters at secondary vertex. Shown is K_s^0 decay, for Λ replace π^+ with p.	54
4.9	Invariant mass of K_s^0 plotted against a certain topological cut-variable	56
4.10	Invariant mass of K_s^0 (left) and Λ (right) after application of consecutive cuts in the following order: 1. no cuts (black), 2. N_{hits} (red), 3. dE/dx (green), 4. DCA to PV (blue), 5. 3D decay length (magenta) 6. radial decay length (light blue) . . .	57
4.11	Left: Mean number of V^0 -candidates after certain cuts vs run-day (beam luminosity). Right: Invariant mass of K_s^0 . Colors described in text.	58
4.12	DCA to PV distribution for V^0 's with 0,1 or 2 daughter tracks matching CTB-hits	59
4.13	p_T -integrated invariant mass distribution of a) K_s^0 and b) Λ after final cuts. Signal region is red, background is blue	61
4.14	Invariant mass of K_s^0 in the 22 p_T -bins. Numerical Values are given in GeV/c. Red line is gaussian plus polynomial fit.	62
4.15	Invariant mass of Λ in the 21 p_T -bins. Numerical Values are given in GeV/c. Red line is gaussian plus polynomial fit.	63
4.16	Mean and width of the gaussian fit to the K_s^0 mass peaks in the first 13 p_T -bins	64
4.17	Mean and width of the gaussian fit to the Λ and $\bar{\Lambda}$ mass peaks in the first 12 p_T -bins	65

4.18	Comparison of the topological distribution variables for K_s^0 between real data and simulation.	67
4.19	Total correction factor (efficiency *acceptance) for K_s^0 (left) and Λ (right) at mid-rapidity $ y <0.5$. This factor does not include the branching ratios.	69
4.20	Transverse momentum distributions of simulated Ξ^- particles and their decay daughter Λ . The Ξ^- datapoints from the STAR measurement are shown as comparison and were measured here [86].	70
4.21	Total correction factors for primary Λ particles (black) and secondary Λ particles from Ξ^- decay (green).	71
4.22	Final Feed-down correction factor vs. p_T	72
4.23	Matching efficiency for TPC tracks to SVT hits with the EST code package. X-axis is position of primary vertex along z in cm. Y-axis is ratio of primary tracks with at least 1 SVT hit divided by total number of primary tracks. Red and black curves show two different track definitions to estimate systematic error.	73
4.24	Λ invariant mass for V^0 's with and without SVT-hits. Right plot shows the uncorrected yield vs. p_T	75
4.25	K_s^0 invariant mass for V^0 's with and without SVT-hits. Right plot shows the uncorrected yield vs. p_T	75
5.1	Corrected p_T -spectra for K_s^0 (left), Λ and $\bar{\Lambda}$ (right). Before feed-down correction from Ξ^- . Statistical errors only.	77
5.2	Fit-functions and their χ^2 values for corrected p_T -spectra for K_s^0 : a) m_T -exponential b) power-law c) composite(inclusive) d) composite(exclusive)	81

5.3	Fit-functions and their χ^2 values for corrected p_T -spectra for Λ : a) m_T -exponential b) power-law c) composite(inclusive) d) composite(exclusive)	81
5.4	Ratio of $\bar{\Lambda}/\Lambda$ vs p_T in $ y <0.5$. Dashed line is weighted fit to datapoints.	83
5.5	Definition of multiplicity classes used in this analysis with mean value per class	87
5.6	p_T -spectra for K_s^0 (left) and Λ (right) in the N_{ch} classes as described above. Dashed lines are composite function 5.4 and 5.6	89
5.7	$\langle p_T \rangle$ vs $\langle dN_{ch}/d\eta \rangle$ for K_s^0 . Error bars are statistical and highly correlated.	90
5.8	$\langle p_T \rangle$ vs $\langle dN_{ch}/d\eta \rangle$ for Λ . Error bars are statistical and highly correlated.	91
5.9	Left side is dN/dy of K_s^0 vs. event multiplicity, $\langle N_{ch} \rangle$. Results for the two best fit-functions are shown. Right side is dN/dy per charged track vs. $\langle N_{ch} \rangle$	92
5.10	Left side dN/dy of Λ vs. event multiplicity, $\langle N_{ch} \rangle$. Results for the two best fit-functions are shown. Right side is dN/dy per charged track vs. $\langle N_{ch} \rangle$	92
5.11	Ratio of $\bar{\Lambda}/\Lambda$ vs event multiplicity. Dashed line indicates minimum bias value of ratio.	93
5.12	R_{pp} ratio for K_s^0 (left) and Λ as defined in equation 5.8 above.	94
5.13	Ratio of Λ/K_s^0 vs p_T for three different event multiplicity classes. Lines connect the datapoints and are to guide the eye only.	95

6.1	First observations of $\theta^+ \rightarrow K^+ + n$ by LEPS collaboration [97] and CLAS collaboration [99].	98
6.2	Flavor Anti-decuplet in the Jaffe-Wilczek diquark model. Taken from [106]	99
6.3	Possible θ^+ production channels via N^* (2400) resonance. Taken from [100]	101
6.4	K_s^0 cut-distribution before (black) and after (red) cuts $d + Au$ collisions. a)invariant mass, b)decay length, c) $n\sigma$ dE/dx, d)daughter n_{hits} , e)Parent DCA to PV, f) pion daughter momenta	104
6.5	Proton cut-distribution before (black) and after (red) cuts $d + Au$ collisions.a)Track n_{hits} , b)Track DCA to PV, c)total momentum, d) $n\sigma$ dE/dx	105
6.6	Armenteros-Podolanski plot for K_s^0 candidates before (left) and after cuts(right)	105
6.7	Sketch of rotating daughter background method. The momentum of the proton is rotated around the z-axis by an angle β and the θ^+ invariant mass is computed with the original K_s^0 momentum and the rotated proton momentum.	106
6.8	Comparison of proton-daughter momentum from real data and simulated θ^+ decay	108
6.9	θ^+ reconstruction efficiency from MC study in $p + p$ collisions. Left: efficiency vs transverse momentum, right:efficiency vs rapidity.	109
6.10	θ^+ reconstruction efficiency from MC study in $d + Au$ collisions. Left: efficiency vs transverse momentum, right:efficiency vs rapidity.	110

6.11	θ^+ invariant mass in $p + p$ simulation. Left: Simulation input, right: reconstructed peak showing experimental resolution of ≈ 6 MeV	111
6.12	θ^+ invariant mass in $d + Au$ simulation. Left: Simulation input, right: reconstructed peak showing experimental resolution of ≈ 5 MeV	112
6.13	θ^+ invariant mass in $p + p$ collisions. Fit is gaussian plus linear background. Top row: Without strict k^- cut. Center row: k^- is required to pass the cuts. Bottom row: requirement on N^* invariant mass	114
6.14	θ^+ invariant mass in $d + Au$ collisions. Fit is gaussian plus linear background. Top row: Without strict k^- cut. Center row: k^- is required to pass the cuts. Bottom row: requirement on N^* invariant mass	115
7.1	Comparison of inclusive p_T -spectra for K_s^0 (left) and Λ (right) for STAR vs CERN UA5 experiment [58, 57]	120
7.2	Rapidity distribution for K_s^0 (left) and Λ (right) from PYTHIA simulation of $p + p$ events.	121
7.3	Anti-particle to particle ratios.	122
7.4	Comparison of inclusive $\langle p_T \rangle$ vs. N_{ch} for K_s^0 (left) and Λ (right) for STAR vs other experiments. p_T range of E735 was 0.3-1.5 GeV/c [61]. UA1 measurement extended to 6 GeV/c (K_s^0) and 7 GeV/c (Λ) [15]	124
7.5	$\langle p_T \rangle$ vs $\langle dN_{ch}/d\eta \rangle$ for different particles measured by STAR in $p + p$ collisions at $\sqrt{s} = 200$ GeV.	126
7.6	$\langle p_T \rangle$ vs particle mass in central Au+Au and $p + p$ collisions measured by STAR	128

- 7.7 Compilation by Eskola et al. of K-Factors for charged hadrons spectra computed at different \sqrt{s} using KKP fragmentation functions. The inner error bars are the statistical errors calculated, the outer reflect the systematic errors reported by the experiment. Taken from [79] 131
- 7.8 N_{ch} distribution for $p + p$ minbias at $|y| < 0.5$ from PYTHIA vs STAR data for different tunes. 132
- 7.9 K_s^0 particle spectra (squares) for $p + p$ minbias at $|y| < 0.5$ compared to default (black line) and tuned (red line) PYTHIA (v6.221, MSEL1) 133
- 7.10 Λ particle spectra (circles) for $p + p$ minbias at $|y| < 0.5$ compared to default (black line) and tuned (red line) PYTHIA (v6.221, MSEL1) 134
- 7.11 $\langle p_T \rangle$ vs N_{ch} for K_s^0 (square) and Λ (triangles) from data compared to different tuned PYTHIA results (black lines). Lower line is K_s^0 , upper is Λ 135
- 7.12 Comparison of most recent version of PYTHIA (6.317) to K_s^0 (left) and Λ (right) 137
- 7.13 Comparisons of NLO calculation from W.Vogelsang with STAR data for K_s^0 (left) and Λ (right). μ is the factorization scale of the calculation and its variation gives an estimate of the uncertainty. 138

7.14	NLO calculations for K_s^0 by Albino, Kramer and Kniehl (AKK) (full lines) together with $p + p$ data from STAR at $\sqrt{s} = 200$ GeV (lower points, scaled down by 30) and $\bar{p} + p$ data from UA1 at $\sqrt{s} = 630$ GeV (upper points). Dashed lines are previous NLO calculations by Kramer, Kniehl and Potter (KKP) with older parametrizations. Taken from [77]	139
7.15	Comparison of charged multiplicity distributions N_{ch} for $p + p$ minbias between data and EPOS v1.02.	141
7.16	Comparison of most recent version of EPOS to $p + p$ minbias p_T -spectra for K_s^0 (left) and Λ (right)	141
7.17	Prediction of strange baryon enhancement in Pb+Pb collisions with respect to $p + p$ collisions at $\sqrt{s} = 8.73$ GeV and $\sqrt{s} = 130$ GeV. Taken from [84]	144
7.18	Strangeness enhancement for Λ and Ξ^- in central collisions at STAR (full symbols) and NA57 (open symbols, $\sqrt{s} = 17.3$ GeV). Left panel is for particles, right panel is for anti-particles. . . .	144
7.19	Nuclear modification factor R_{CP} for mesons and baryons at $\sqrt{s} = 200$ GeV. Taken from [92].	146
7.20	Nuclear modification factor for mesons (left) and baryons (right) in STAR at $\sqrt{s} = 200$ GeV [88]	147

List of Tables

4.1	Table of vertex "finding status" for events from the simulation study	45
4.2	Summary of events statistics after event selection cuts.	49
4.3	summary of V^0 cuts	55
5.1	A summary of χ^2/ndf values for all tested fit-functions to the different particle p_T -spectra.	80
5.2	A summary of yields and $\langle p_T \rangle$ at mid-rapidity ($ y < 0.5$) including statistical and systematical errors. The feed-down corrected yields for Λ and $\bar{\Lambda}$ include contributions from Ξ and $\Sigma^*(1385)$	82
5.3	A summary of $\bar{\Lambda}$ to Λ ratio at mid-rapidity ($ y < 0.5$). Errors quoted are statistical only.	84
5.4	A summary of systematic errors from various sources and their magnitude in percent	85
5.5	Summary of number of events and mean N_{ch} for each multiplicity bin. Last column shows the corresponding uncorrected $dN_{ch}/d\eta$	88
6.1	Summary of event selection-cuts	100

6.2	Prefilter cuts for K_s^0	102
6.3	Prefilter cuts for protons and charged kaons	102
6.4	Final cuts for K_s^0	103
6.5	Final cuts for protons and charged kaons	104
6.6	θ^+ Monte-Carlo simulation requests	107
6.7	θ^+ Cross-section estimation with respect to Λ and $\Lambda^*(1520)$ analysis [113, 114].	116
6.8	θ^+ Cross-section estimation by STAR compared to Upper Lim- its published by HERA-B [111].	117
7.1	A comparison of mid-rapidity yields and $\langle p_T \rangle$ for K_s^0 and Λ measured by STAR and UA5. STAR measurements include stat. and syst. errors. The UA5 measurements were made over a large rapidity interval and have been scaled down using the following factors obtained from PYTHIA simulation (see figure 7.2): $K_s^0= 4.67(y < 3.5)$, $\Lambda=3.27 (y < 2.0)$	121
7.2	A summary of tuned PYTHIA parameters.	130
7.3	Comparison of dN/dy and $\langle p_T \rangle$ obtained from PYTHIA and experiment	136
7.4	Comparison of dN/dy and $\langle p_T \rangle$ obtained from EPOS and ex- periment. Statistical and systematical errors shown for data.	142
A.1	K_s^0 spectra values as plotted in figure 5.1	152
A.2	Λ spectra values as plotted in figure 5.1	153
A.3	$\bar{\Lambda}$ spectra values as plotted in figure 5.1	154
A.4	$K_s^0 \langle p_T \rangle$ from composite fit values as plotted in figure 5.7 . . .	155
A.5	$K_s^0 \langle p_T \rangle$ from powerlaw fit vs N_{ch} as plotted in figure 5.7 . . .	155
A.6	$K_s^0 dN/dy$ values from composite fit as plotted in figure 5.9 . . .	156

A.7	K_s^0 $dN/d\mathbf{y}$ values from powerlaw fit as plotted in figure 5.9 . . .	156
A.8	Λ $\langle p_T \rangle$ values from composite fit as plotted in figure 5.8 . . .	157
A.9	Λ $\langle p_T \rangle$ values from m_T -exp fit as plotted in figure 5.8	157
A.10	Λ $dN/d\mathbf{y}$ values from composite fit as plotted in figure 5.10 .	158
A.11	Λ $dN/d\mathbf{y}$ values from m_T -exp fit as plotted in figure 5.10 . . .	158

CURRICULUM VITAE

Personal Data

Full Name: Mark Thomas Heinz

Nationality: Swiss / British

Date of Birth: 28 May 1971

Place of Birth: Geneva, Switzerland

Marital Status: married, 1 daughter

Education

1978 - 1983 Primarschule, Rorbas-Freienstein (ZH)

1983 - 1990 **Matura Typ B (Latein)**

Kantonsschule Zürcher Unterland, Bülach (ZH)

1991 - 1997 **Diplome d'Ingénieur Physicien**

Ecole Polytechnique Fédérale de Lausanne, Lausanne (VD)

2002 - 2005 **Doktorat**

Universität Bern, Bern (BE)

Professional Experience

1997 - 1999 Pilatus Aircraft AG, Stans (NW)

1999 - 2001 Transairco AG (Subsidiary of Pilatus Aircraft), Genève (GE)

2001 - 2002 Contraves Space AG, Zürich (ZH)